Total ionizing dose monitoring for mixed field environments

Matteo Brucoli

THÈSE POUR OBTENIR LE GRADE DE DOCTEUR DE L'UNIVERSITÉ DE MONTPELLIER

En Electronique

École doctorale Information, Structures et Systèmes (I2S)

Unité de recherche Institut d'Electronique et des Systèmes (IES)

TOTAL IONIZING DOSE MONITORING FOR MIXED FIELD ENVIRONMENTS

MESURE DE DOSE IONISANTE EN CHAMPS DE RAYONNEMENT MIXTE

Présentée par Matteo BRUCOLI

Le 30 novembre 2018

Sous la direction de Laurent DUSSEAU et Frédéric WROBEL

Devant le jury composé de

Laurent DUSSEAU, Professeur, Université de Montpellier, IES	Directeur de thèse
Frédéric WROBEL, Professeur, Université de Montpellier, IES	Co-directeur de thèse
Lionel TORRES, Professeur, Université de Montpellier, LIRMM	Examinateur
Salvatore DANZECA, Docteur, CERN	Examinateur
Sylvain GIRARD, Professeur, Université Jean-Monnet-Saint-Étienne	Rapporteur
Lodovico RATTI, Professeur, Università degli Studi di Pavia, Electronic Instrumentation Laboratory	Rapporteur

UNIVERSITÉ DE MONTPELLIER

Abstract

The Total Ionizing Dose (TID) monitoring is nowadays a crucial task for a wide range of applications running in harsh radiation environments. In view of the High-Luminosity upgrade for the Large Hadron Collider, the monitoring of radiation levels along the CERN's accelerator complex will become even more challenging. To this extent, a more detailed knowledge of the radiation field in the accelerator tunnel and its adjacent areas becomes necessary to design installation, relocation or shielding requirements of electronics sensitive to radiation. Aiming to improve the monitoring of the TID delivered by the mixed radiation field generated within the accelerator system, investigations on new suitable dosimeters have been carried out.

With this research, two devices have been studied and characterized to be employed as dosimeter and possibly to integrate the use of the silicon sensor currently employed at CERN for TID monitoring, i.e. the RADiation-sensitive Field Effect Transistor (RADFET): a commercial NMOS, and an ASIC (Application-Specific Integrated Circuit) named FGDOS. The devices have been selected following two opposite approaches: on the one hand, reducing the costs would allow the density of the deployed sensors to increase. As a direct consequence, a more detailed dose map would be obtained for large distributed systems like the LHC. On the other hand, the radiation monitoring can be further improved by deploying more sensitive detectors, which would allow to measure the dose where the levels are too low for the RADFET. Moreover, sensors with higher resolution would permit the characterization of the radiation field in a shorter time, which means within a lower integrated luminosity.

The first approach has been accomplished by searching for alternative solutions based on COTS (Commercial Off-The-Shelf) devices, which would significantly reduce the costs and guarantee unlimited availability on the market. For this aim, investigations on a commercial discrete NMOS transistor, which was found to be very sensitive to the radiation, has been carried out.

The need for improving the resolution of TID monitoring led to investigate the FGDOS, which is an innovative silicon dosimeter with a very high sensitivity that enabling the detection of to detect extremely low doses.

The calibration of the NMOS and the FGDOS have been performed by exposing the dosimeters to γ-ray. Their radiation response has been characterized in terms of linearity, batch-to-batch variability, and dose rate effect. The influence of the temperature has been studied and a method to compensate for the temperature effect has been developed and implemented.

Being the FGDOS a System-On-Chip with several features that make the dosimeter an extremely flexible system, the characterization of its operational modes (Active, Passive and Autonomous) have been performed. Following the first characterization, some questions arose concerning the sensitivity degradation mechanisms affecting the dosimeter. To investigate this phenomenon, radiation experiments were performed with a test chip embedding only the radiation sensitive circuit of the FGDOS. The analysis of the experiments allowed the understanding of the processes responsible for the sensitivity degradation, by separating the contribution of the reading transistor and the floating gate capacitor. The results of this investigation led us to considerer new design solutions and compensation methods.

The suitability of the NMOS and the FGDOS for TID measurement in the mixed radiation field produced by the CERN's accelerator complex has been verified by performing accelerated radiation tests at the Cern High energy AcceleRator Mixed field facility (CHARM). The consistency of both sensors with the RADFET measurement has been demonstrated. The high sensitivity of the FGDOS leads to a significant improvement in terms of TID measurement in mixed radiation fields with respect to the RadFET, especially for low radiation intensities.

Keywords

Radiation Monitoring, Total Ionizing Dose, Dosimetry, Radiation Environment.

Résumé

La mesure de la dose ionisante est aujourd'hui une tâche cruciale pour une large gamme d'applications fonctionnant dans des environnements de rayonnement sévères. Dans le contexte de l'amélioration de la luminosité du grand collisionneur de hadrons (LHC), la mesure des niveaux de rayonnement le long du complexe d'accélérateurs du CERN va devenir encore plus difficile. A cet effet, une connaissance plus détaillée du champ de rayonnement dans le tunnel de l'accélérateur et ses zones adjacentes devient nécessaire pour définir les exigences d'installation, de déplacement ou de blindage de l'électronique sensible au rayonnement. Dans l'objectif d'améliorer la mesure de la dose absorbée par les systèmes exposés au champ de rayonnement mixte généré par l'accélérateur, des investigations sur des nouveaux dosimètres ont été menées.

Dans le cadre de cette recherche, deux dispositifs ont été étudiés et caractérisés pour être utilisés comme dosimètres et éventuellement pour compléter l'utilisation du dosimètre au silicium actuellement utilisé au CERN, à savoir le RADFET (RADiation-sensitive Field Effect Transistor) : un NMOS commercial et un ASIC (Application-specific Integrated Circuit) nommé FGDOS. Les dispositifs ont été sélectionnés selon deux approches opposées : d'une part, la réduction des coûts permettrait d'augmenter la densité des capteurs déployés. En conséquence directe, une carte des doses plus détaillée serait obtenue pour les grands systèmes distribués comme le LHC. D'autre part, la dosimétrie peut être améliorée en déployant des détecteurs plus sensibles, ce qui permettrait de mesurer la dose lorsque les niveaux sont trop faibles pour le RADFET. De plus, des capteurs à plus haute résolution permettraient de caractériser le champ de rayonnement dans un temps plus court, c'est-à-dire avec une luminosité intégrée plus faible.

La première approche a été réalisée en recherchant des solutions alternatives basées sur des dispositifs COTS (Commercial Off-The-Shelf), qui réduiraient considérablement les coûts et garantiraient une disponibilité illimitée sur le marché. À cette fin, des recherches ont été menées sur un transistor NMOS discret commercial, qui s'est révélé très sensible au rayonnement.

La nécessité d'améliorer la résolution de la mesure de dose a conduit à étudier le FGDOS, un dosimètre en silicium innovant à très haute sensibilité qui permet de détecter des doses extrêmement faibles.

La calibration du transistor NMOS et du FGDOS a été effectuées en exposant les dosimètres à des rayons gamma. Leur réponse au rayonnement a été caractérisée en termes de linéarité, de variabilité d'un lot à l'autre et d'effet du débit de dose. L'influence de la température a été étudiée et une méthode pour compenser l'effet de la température a été développée et mise en œuvre.

Le FGDOS étant un système sur puce (SoC) avec plusieurs caractéristiques qui font du dosimètre un système extrêmement flexible, la caractérisation de ses différents modes de fonctionnement (actif, passif et autonome) a été effectuée. Suite à la première caractérisation, des questions se sont posées concernant les mécanismes de dégradation de la sensibilité affectant le dosimètre. Pour étudier ce phénomène, des campagnes d'irradiations ont été effectuées avec une puce d'essai incorporant seulement le circuit sensible au rayonnement du FGDOS. L'analyse des expériences a permis de comprendre les processus responsables de la dégradation de la sensibilité, en séparant la contribution du transistor de lecture de celle du condensateur à grille flottante. Les résultats de cette étude nous ont amenés à envisager de nouvelles solutions de conception et des méthodes de compensation.

L'aptitude du transistor NMOS et du FGDOS à mesurer la dose ionisante dans les champs de rayonnement mixtes produits par le complexe d'accélérateurs du CERN a été vérifiée à l'aide de test radiatifs accélérés effectués dans le centre de tests en champs mixte à haute énergie du CERN (CHARM).

Mots-clés

Surveillance des radiation, Dose Ionisante, Dosimetrie, Environnement Radiatif.

Contents

List of Figures

List of Tables

Chapter 1 Introduction

1.1 Context and Overview

The aim of understanding the laws that govern the Universe requires the performance of extremely complex experiments in order to verify the theoretical models describing the elementary particles the matter is composed of and the forces keeping them together. At CERN, the European Organization for Nuclear Research, physicists and engineers from all over the world work side by side to reproduce the conditions that arose a few instants after the Big Bang, availing themselves of the largest particle accelerator in the world, i.e. the Large Hadron Collider (LHC), and of extremely advanced scientific instruments. To make this possible, beams of charged particles are accelerated close to the speed of light and made to collide with each other or with fixed targets. These collisions produce a large diversity of secondary particles observed by means of extremely complex machines, called particle detectors, which have been designed to identify the products of those interactions. The results of these experiments provide clues about the processes leading to the multitude of the existing physical phenomena in the Universe. Invaluable discoveries in the history of science and technology have been made possible for the first time, and earned several scientists the Nobel Prize, thanks to the uniqueness of the research that can be performed within this environment.

The technological challenges that must be faced to accelerate tiny elements, such as protons or ions, up to very high energies and made them collide with each other, detecting the products of these interactions, involve several disciplines. In many cases, high energy physics experiments performed at CERN required to overcome the state of the art established at that moment, pushing the technological limits even further. As it will be discussed, it appears to be clear that reliability becomes a major challenging task for electronic systems working in radiation environments, such as the ones generated by particle colliders. In this concern, a detailed knowledge of the radiation environment is required to prevent or mitigate failures in electronic systems. In fact, a side effect of these high energy experiments is the production of unwished radiation fields, which affect the electronic equipment installed along the tunnel and in the adjacent areas and may be responsible of damages and failure of whole electronic systems running in this environment. In the experimental areas, the beam-to-beam or beam-to-target collisions produce high energy radiation fields. In addition, distributed beam losses, due to the interaction of the beam with collimators and collimator-like objects, , as well as the interactions between the residual gas in the beam line and the particles traveling close to the speed of light, generate a significant amount of radiation.

The radiation field depends on several variables that make its characteristics difficult to be predicted, such as beam interactions with residual gases in the pipeline or some optical parameters that must be tuned to control the beam according to the running operation (e.g. injection, ramping, squeezing, etc. (REF LHC NOMINAL CYCLE)). Furthermore, the distance, the angle and the shielding that may be present between the interaction point (i.e. where the beam interacts with the residual gas, the collimators, beam itself, etc.) and the considered location affect the field composition, its intensity (i.e. the number of particles crossing a unit area per second) and the spectrum of the field (i.e. the intensity distribution over the energy range). Thus, the ability to measure and monitor the radiation levels is of fundamental importance, as simulation is not sufficient describe this specific type of radioactive environments.

One of the main concerns about the performance of the LHC is related to its ability to produce a vast quantity of interactions over time. Indeed, the products of the collision that are of interest to particle physicists at CERN, generated through the interaction of the two proton beams and measured in the experiments, are extremely rare. Therefore, a huge quantity of events is required to provide a sufficient level of statistics. Thus, the efficiency of the collider can be quantified by its integral luminosity, i.e. the number of collisions cumulated in a certain period of time. The high level of performance needed can be reached either by increasing the luminosity (the number of collisions per unit time and area), or by increasing the operational time of the machine. That means that, in order to accomplish the mission for a more efficient functioning of the collider, a reduction either in the number of premature dumps, or in the average fault time is necessary. Radiation plays an important role, as far as the number of dumps is concerned, since a significant proportion of premature dumps are due to radiation-induced failures in the electronic system.

The Radiation to Electronics (R2E) project at CERN is responsible for the optimization of the performance of the LHC system in terms of the number of radiation-induced dumps per unit integrated luminosity. In order to deal with radiation effects on electronics affecting the correct functioning of the collider, several remedial and preventive measures could be evaluated. Either when a radiation-induced failure occurs, or as a intervention required after the analysis of the radiation environment, some direct measures can be applied on the interested system: relocation, improvement of the shielding, or replacement with a radiation resistant system. However, these remedial solutions might be only partially feasible and their effectiveness strongly depends on the system requirements (some equipment must be located in the proximity of the accelerator for technical reasons) and on the room availability that is necessary to improve the shielding. Moreover, the LHC complex is an extremely big machine and the number of electronic components in use that are susceptible to radiation-derived

damages is very high. In this context, from a sustainability and economic viability point of view, it would be certainly impracticable to employ radiation-hardened components only, as is regularly done in space applications instead.

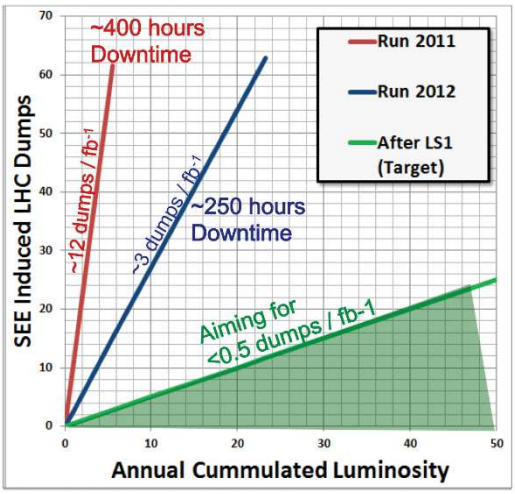

Figure 1. LHC beam dumps due to radiation-induced failures (SEEs) versus beam luminosity (source [1]).

Figure 1 shows the number of dumps per unit integrated luminosity in 2011, 2012 and 2015 LHC runs. As it can be seen, the number of dumps clearly decreases over time and, even if it is not shown in the picture, run 2017 was characterized by a further reduction of this figure-of-merit. These achievements were made possible thanks to R2E mitigation actions.

Based on these considerations, the research on new dosimeters suitable for accelerator-like environments appears to be essential. In fact, as it has been already pointed out, the radiation monitoring plays a crucial role and a detailed knowledge of the radiation environment is necessary to efficiently perform any mitigation or preventive action. Moreover, this issue is expected to become even more critical in view of the implementation of the Hi-Lumi project that is supposed to be characterized by a 10 times higher integrated luminosity and, therefore, by a proportional increase in the levels of radiation.

Cost containment and improvement of the measurement resolution have both driven the selection of the two sensors object of study in this research, a commercial NMOS transistor and an ASIC device called FGDOS (Floating Gate Dosimeter), that have been studied and characterized.

1.2 Radiation Effects on Electronics

Radiation effects on electronics can be divided in two main categories, named *cumulative effects* and *Single Event Effects* (SEEs). The first category includes all the effects resulting from the sum of micro-effects due to each single penetrating particle. Cumulative effects can be defined as macroscopically observable variations in the characteristics of an electronic circuit or component due to the gradual degradation of some electronic parameters.

The second category includes all the macroscopically observable effects induced by a single highly-energetic particle that deposits enough energy in a sensitive volume of the device to trigger the event. Being this mechanism stochastic, SEEs are not easily predictable and mitigation techniques must be employed in harsh environments to avoid failures. Single Event Effects include a large variety of radiation damages, which can be further divided into destructive (hard) or non-destructive (soft) events.

1.3 Radiation Interactions

The most accurate way to describe a radiation environment would require the evaluation of the flux as a function of the energy for each type of particle. However, this level of attention to detail is not necessarily useful for the purpose, especially when the aim is to predict radiation-induced damages and failures of electronic components and systems. Intending to describe a radiation environment, the measurement of other physical quantities, such as the total dose and the fluence of some specific type of particles, is more convenient, as they are directly related to the different effects induced by radiation on electronics. To understand the meaning of these quantities and why they constitute a good choice, the interactions of radiation with matter should be introduced.

Radiation deposits energy on matter in several ways depending on the type of impinging particle and its energy, the target material (i.e. the material the device crossed by radiation is composed of) and the type of interactions involved. A major first distinction between the different interaction processes that could occur must be done. The two main types of interaction are the following:

- The incident radiation interacts with the electrons of the target material;
- The incident radiation interacts with the nuclei of the target material.

In the former case, radiation is defined as ionizing radiation, whereas we talk about non-ionising radiation in the latter.

1.3.1 Ionizing Radiation

The ionization of matter is triggered by Coulumb interaction between the incident particle and the electrons of the target material. Charged particles deposit their energy by exciting the electrons of the outermost shell of the atoms, which gain enough energy to leave their atomic site: this mechanism is known as “direct ionization”. In case these excited electrons absorb sufficient kinetic energy to travel matter and ionize other atoms, the energy deposition mechanism occurs in two steps, primary electron excitation and secondary ionization, and is called “indirect ionization”. The excited electrons are called delta rays, or primary knock-on electrons.

However, the ionization of the atoms is not only induced by the effect of charged particles. Photons can trigger the indirect ionization process in different ways, depending on their energy and the atomic species the photons interact with. For example, an incident photon can partially deliver its energy to an electron through the Compton scattering: in this process, the photon is diffused with a different wavelength and direction, whereas the electron may get enough energy to ionize one or more atoms. Another important mechanism through which photons deposit their energy into matter is known as photoelectric effect. In this case, the photon is totally absorbed by the electron, which is liberated even from inner shells with enough energy to ionize more atoms. The probability to trigger the photoelectric effect is proportional to the atomic number Z and decreases with the photon energy. Finally, a further process that must be considered in this context is the so-called pair production: high-energy photons ($E > 1.02$ MeV) can generate electron-positron pairs by interacting with the nuclei. Again, the secondary particles can deposit their energy on matter by ionizing other atoms.

Considering the several phenomena involved, energy deposition through ionization can be an extremely complex process. Thus, to quantify the effect induced by photons or charged particles through the above-described mechanisms, it is convenient to describe the outcome of these phenomena considering the generation of electron-hole pairs within the semiconductor and insulator materials composing the electronic device, irrespective of their creation process. As it will be pointed out in the next section, the free carriers generated by the ionizing radiation are responsible for cumulative and stochastic effects, each of which can be measured by dedicated physical quantities. In this concern, to fully understand the physical manifestation of ionizing radiation, some considerations should be done concerning the spatial distribution of the energy deposition along the particle track. Firstly, the probability of interactions between the penetrating particle and the electrons of the medium depends on the speed of the particle: the slower the particle, the higher the probability of interaction. Furthermore, as the particle deposits energy in the material, its speed decreases along the

path. These two mechanisms feed each other until the particle does not have enough energy to ionize more atoms. As a result, the energy loss rate gradually increases along the particle path, until it reaches the so-called Bragg peak, and then abruptly drops to zero. The rate of energy loss through ionization along the particle path normalized by the density of the material[1] is called *electronic mass stopping power*, and can be calculated as [2]

$$S = \frac{1}{\rho}\frac{\partial E}{\partial x}\Big|_e$$

Equation 1.1

where ρ is the density of the material, ∂E represents the energy loss and ∂x is the increment of path length, whereas the subscript e highlights that the energy is loss "electronically", or in other words, through direct and indirect ionization. In this expression, all the energy transferred to the medium through ionization is considered, even though a portion of it propagates in the medium by means of the knock-on electrons, far from the point where it was deposited by the incident particle. This physical quantity is also called *unrestricted Linear Energy Transfer* and it is typically expressed in [MeV·cm^2/mg], although the appropriate SI unit would be [N·m^3/kg]. However, when highly accurate information on the energy distribution is necessary, it might be necessary to consider only the energy that remains along the particle path, excluding the component that scatters by means of delta rays. In this case, the energy loss rate per unit length is called *restricted Linear Energy Transfer*, and it is expresses as:

$$LET_\Delta = \frac{1}{\rho}\frac{\partial E_\Delta}{\partial x}\Big|_e$$

Equation 1.2

Where ∂E_Δ represents the energy loss of the impinging charged particle due to electronic collisions while traversing a distance ∂x, excluding all secondary knock-on electrons with kinetic energies larger than Δ. If the energy interval considered is large enough to include all the delta rays generated, then the restricted LET corresponds to the unrestricted LET, or electronic mass stopping power.

In Figure 2, the LET for some heavy ions penetrating silicon with different energies is shown. This curve describes the force acting on the impinging particle as a function of the material depth and is

[1] The energy loss rate is commonly normalized by the density of the material in order to greatly reduce, but not remove, the dependency on the density. In this way, energy loss rate for different materials can be compared. However, in some documents this normalization in not done: in this case, the energy loss rate is called *linear stopping power*.

called the Bragg curve. As can be seen, the energy loss distribution is different for each particle, as it depends on the particle species and its energy.

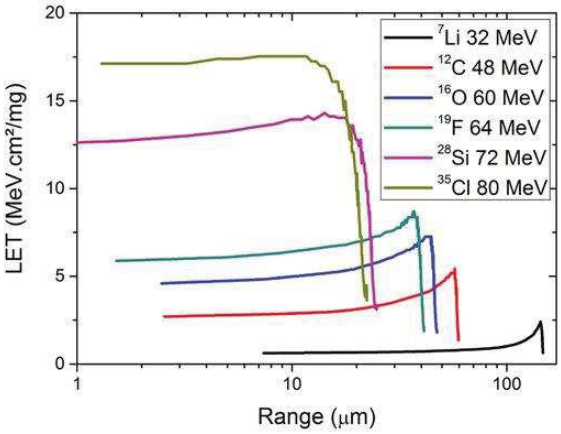

Figure 2. LET as a function of the range in silicon for some heavy ions. (Source [3])

Differently from charged particles, photons absorption cannot be described by LET. As mentioned above, photons may be absorbed in a single process (photoelectric effect or pair production), or it continues unchanged on its path. (Only in the case of the Compton interaction, the photon proceeds with a lower energy). Photon absorption therefore obeys an exponential law, which can be described by the absorption coefficient.

To quantify the cumulative damage induced by ionizing radiation, the most convenient physical quantity commonly considered is the ionizing energy deposited per unit mass, namely Total Ionizing Dose (TID) or *absorbed dose*. In formula:

$$TID = \frac{E}{m}$$

Equation 1.3

Where *E* is the energy deposited in the fraction of mass *m*. The corresponding unit of measurement adopted by the International System of Units (SI) is called *Gray* (symbol *Gy*) and corresponds to one joule of energy absorbed by one kilogram of mass. However, in the space community, the dose is commonly measured in *rad*, according to the *Centimetre–Gram–Second* system of units (CGS). The equivalence between *rad* and *Gray* is the following:

$$1\,Gy = 100\,rad$$

Equation 1.4

Moreover, since the dose depends on the target material, it must be specified when dose measurements are reported. In this work, all the dose values are referred to silicon.

In the context of a radiation environment composed by a large variety of particles whose energies range from meV to tens of GeV, such as the one produced by the LHC, the sum of the energy contributions deposited by all the incident particles composing the mixed field, weighted by their LET, should be considered. The energy deposited per unit mass, or Total Ionizing Dose (TID), can be expressed as:

$$TID = \int LET(E) \times \frac{\partial \Phi(E)}{\partial E} \partial \Phi(E)$$

Equation 1.5

where *Φ(E)* represents the fluence for each particle composing the mixed field as a function of the energy *E*. Therefore, the TID is the sum of the energy deposited by all the penetrating particles in the medium. However, if the ionization generated by a single particle occurs in a sensitive volume of the electronic component, a macroscopically observable effect can be induced. The manifestation of this phenomenon occurs in many different ways, depending mainly on the device. For example, SRAM memories are subject to the switching of logic states, which can be restored to its initial value by rewriting the bit: this type of non-destructive events are called Single Event Upset (SEUs). Nevertheless, a highly-ionizing particle might activate parasitic structures that trigger latch-up in CMOS devices. This event can be destructive and is named Single Event Latch-up (SEL). To measure the component of the radiation field responsible for the SEEs, only the particles having a sufficiently high LET must be considered. For this purpose, the physical quantity commonly used is the fluence of High Energy Hadrons, i.e. neutral and charged hadrons whose energy is above 20 MeV.

1.3.2 Non-Ionizing Radiation

Neutrons, charged hadrons and heavy ions can transfer their energy by interacting with the nuclei of the target material. The impinging particle transfers its energy by hitting the nucleus of the lattice. Depending on the amount of energy involved in the collision, these interactions can be divided into inelastic or elastic scattering. In inelastic scattering, or hard collision, the kinetic energy of the incident particle is enough to break the nucleon, producing nuclear fragments, which, in turn, can deposit more energy through ionization or nuclear scattering. However, this phenomenon is extremely rare and can be neglected in this context. In elastic scattering, or soft collision, the incident particle knocks

the nucleon, displacing the atom from its initial lattice position, which leaves an empty atomic site called vacancy. Both the vacancy and the primary knock-on atom (shortly PKA) can recombine, as it is the case for 95% of the pair produced, or migrate to a more energetically stable site and become a stable defect (see Figure 3).

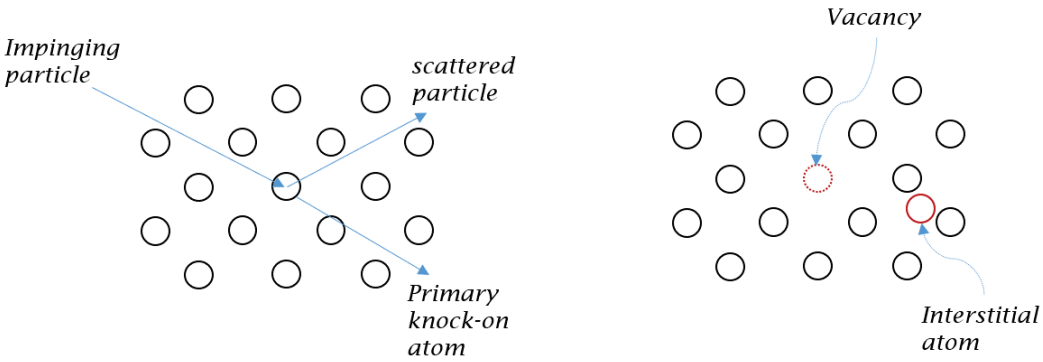

Figure 3. Displacement Damage: the atom is dislodged and a Frenkel pair is produced.

The minimum energy necessary to create a vacancy-PKA pair (also called Frenkel pair) is 21 eV [4]. In addition, if the PKA has enough kinetic energy (more than 1-2 keV) it can induce itself displacement damage. For energies above 10-20 KeV, regions with high density of defects, called clusters, are generated [5], as depicted in Figure 4.

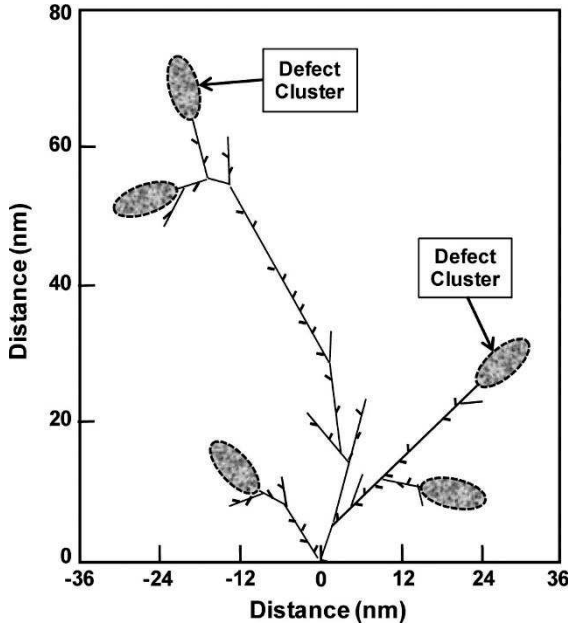

Figure 4. Clusters and isolated defects induced by a 50 keV primary recoil atom in Si. (Source [6])

Although interstitial atoms do not affect the functioning of electronic devices, vacancies do play an important role for components based on bulk conduction, such as bipolar transistor, diodes and JFET transistor. These defects act like recombination or trapping centres for minority carriers, reducing their lifetime and, therefore, the mobility in the lattice. As a consequence, the electrical parameters generally affected concern the output current or the current gain of these devices, such as the current gain (β) of bipolar transistors, the efficiency of solar cells, the output light of LEDs and optocouplers, the dark current in CCD cameras, etc. As an example, the degradation of the Current Transfer Ratio (CTR) of commercial optocouplers exposed to Displacement Damage (shortly DD) and TID is shown in Figure 5.

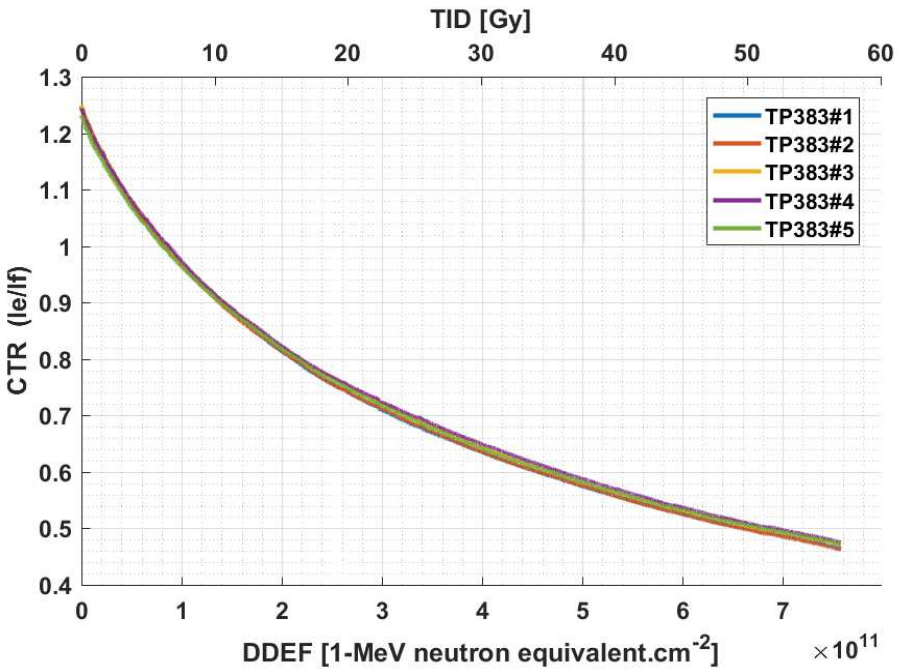

Figure 5. Current Transfer Ratio (CTR) of Optocouplers exposed to DD and TID. (Source [7])

According to the Shockley-Read-Hall theory, the concentration of defects is proportional to the non-ionizing dose deposited in the lattice. In a formula, the defect concentration (or damage, D) can be expressed as

$$D = k_d \times DDD$$

Equation 1.6

where k_d is a proportionality factor which depends on the lattice characteristics, and *DDD* is the Displacement Damage Dose, i.e. energy deposited by non-ionizing radiation per unit mass, which can be expressed as

$$DDD = \int NIEL(E) \times \frac{\partial \Phi(E)}{\partial E} \partial \Phi(E)$$

Equation 1.7

where *Φ(E)* is the fluence of the particles composing the radiation environment, and the *NIEL* is the Non-Ionizing Energy Loss, i.e. the portion of energy lost by a traversing particle that does not induce atom ionization. The NIEL is the result of the energy transferred to the target material by non-ionizing interactions per unit distance, normalized by the density of the material. It can be expressed as:

$$NIEL = \frac{1}{\rho} \frac{\partial E}{\partial x}\Big|_n$$

Equation 1.8

where *ρ* is the density of the material, and the subscript *n* emphasizes the fact that the interactions involve the nuclei and not the electrons of the target material. As well as for the LET, the NIEL depends on the energy and the species of the impinging particle. In Figure 6, the NIEL for protons, electrons and neutrons is reported for silicon material.

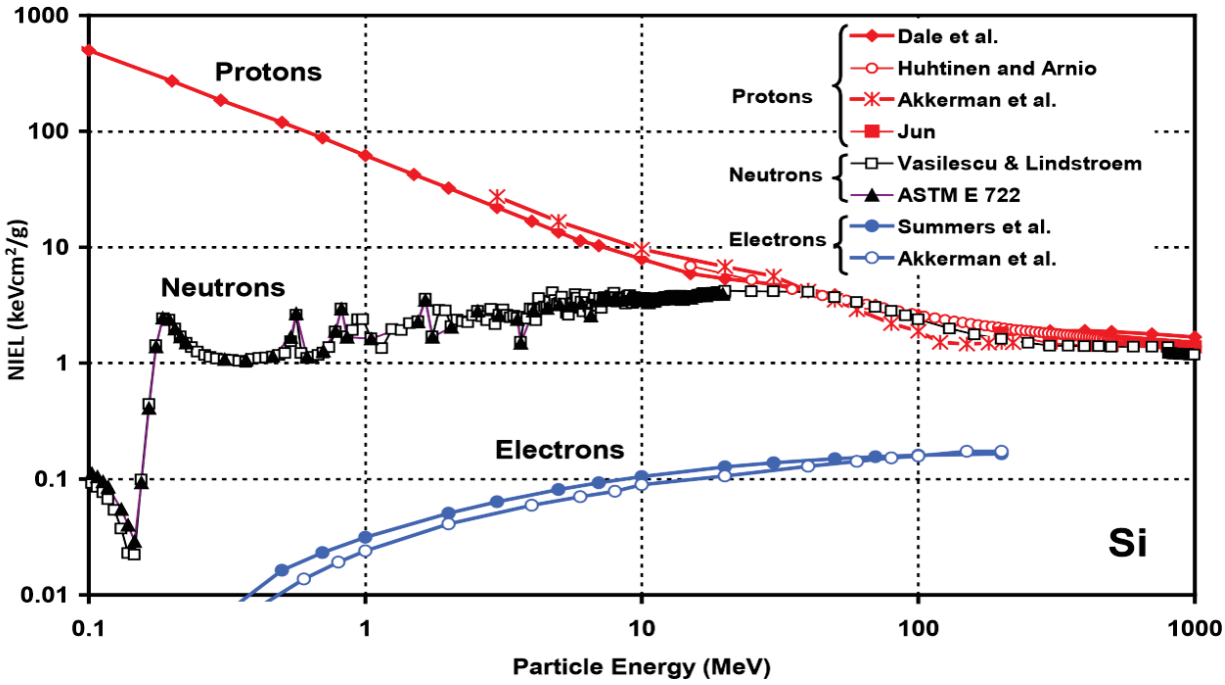

Figure 6. Non-Ionizing Energy Loss (NIEL) for different particle species, as a function of the particle energy. (Source [8])

Generally, the DDD is expressed as the displacement damage equivalent to the one induced by a mono-energetic beam (e.g. 1MeV neutron), and it is called Displacement Damage Equivalent Fluence (DDEF), or 1-MeV equivalent neutron fluence (Φ_{eq}):

$$DDEF = \int \frac{NIEL(E)}{NIEL_{neutron}(1MeV)} \times \frac{\partial \Phi(E)}{\partial E} \partial \Phi(E)$$

Equation 1.9

1.3.3 Neutron Absorption

An important type of nuclear interaction that should be considered is the so-called *neutron absorption*: it occurs when a neutron is captured by a nucleus, which becomes instable, emitting radiation in different forms. This nuclear reaction plays a significant role for technologies using boron (^{10}B), whose thermal neutron capture cross section results extremely high (3840 barns [9]), hundreds of times higher than for other elements employed to fabricate electronic devices. Such a large cross section makes the interaction between a thermal neutron and the ^{10}B nucleus highly probable, consequently affecting the functioning of the electronics using ^{10}B operating in environments characterized by high thermal neutron fluencies, as in the case of the electronic systems installed in the shielded areas along the LHC. The high-energy particle shower produced by beam collisions in the interaction points interacts with several meters of shielding surrounding the experiments' area, generating a significant number of thermal neutrons that reach the shielded areas.

Boron is largely used as a dopant to increase the amount of positive carriers in silicon semiconductors. Moreover, in some fabrication processes, a material containing boron called Boron-Phospho-Silicate Glass (BPSG) is used to coat microchips and as interlevel and intermetal dielectric films for multilevel interconnections [10], as it is characterized by good mechanical and thermal properties. However, it has been observed that BPSG increases the device's susceptibility to soft errors [11].

As the isotope ^{10}B absorbs a neutron, it becomes ^{11}B, which is meta-stable and decays almost instantaneously through one of the following processes:

$$^{10}B + n_{th} \rightarrow \left[^{11}B\right]^{*} \rightarrow {}^{4}He^{2+} + {}^{7}Li^{3+} \qquad (6\%)$$
$$^{10}B + n_{th} \rightarrow \left[^{11}B\right]^{*} \rightarrow {}^{4}He^{2+} + {}^{7}Li^{3+} + \gamma\,(0.48\,MeV) \qquad (94\%)$$

Equation 1.10

The products of these nuclear reactions are alpha particles (i.e. helium nuclei), lithium ions and highly energetic photons, whose total energy is about 2.8 MeV for both reactions. As discussed in the previous section, these particles easily ionize the material along their track, leading to an accumulation of positive charge in the oxides (TID), and concentrated amount of charge in silicon that can induce SEEs.

In the context of radiation monitoring for the accelerator complex, the measurement of thermal neutron fluence becomes extremely important, as the presence of these particles in the mixed radiation fields might affect a large variety of commercial components installed in the shielded areas.

This nuclear reaction is also used in an innovative medical application called Boron Neutron Capture Therapy (BNCT): a non-invasive therapeutic modality for treating locally invasive malignant tumours, which consists in irradiation with ephitermal neutrons the tumor mass previously enriched with ^{10}B.

1.4 Radiation Monitoring System at CERN

At CERN, the monitoring of the radiation levels along the accelerator complex and its adjacent areas is performed by means of the Radiation Monitoring system (shortly RadMon), which allows the measurement of four different physical quantities: Total Ionizing Dose (TID), 1-MeV equivalent neutron fluence (Φ_{eq}), High Energy Hadron fluence (Φ_{HEH}) and Thermal Neutron fluence (Φ_{ThN}). In order to perform these measurements, the variations of different electrical quantities induced by the radiation on three different types of sensor are measured and converted into the above-mentioned physical quantities.

The sensor employed to measure the TID is a special p-channel transistor called RadFET. The ionizing radiation induces a shift in the threshold voltage of the RadFET (shortly ΔV_{th}), which can be converted into TID by knowing the relationship between the absorbed dose and the threshold voltage shift. The use of this sensor, as well as the other two TID detectors (NMOS and FGDOS), will be the subject of the next chapters.

The 1-MeV equivalent neutron fluence (Φ_{neq}) is calculated by measuring the variation of the forward threshold voltage (shortly ΔV_f) of PIN diodes, which is due to the defects generated in the silicon lattice by the impinging particles. The Φ_{neq} is obtained by converting the voltage shift through the relationship between the voltage and the fluence.

The measurement of Φ_{HEH} and Φ_{ThN} is performed by counting the Single Event Upsets (SEUs) induced by radiation in two kinds of SRAM memory. Taking advantage of the different sensitivities that these sensors show to the fluence of high energy hadrons and thermal neutrons, it is possible to calculate the Φ_{HEH} and the Φ_{ThN} by solving the following system for the two fluences:

$$\begin{cases} SEU_1 = \sigma_1^{ThN} \times \Phi_{ThN} + \sigma_1^{HEH} \times \Phi_{HEH} \\ SEU_2 = \sigma_2^{ThN} \times \Phi_{ThN} + \sigma_2^{HEH} \times \Phi_{HEH} \end{cases}$$

Equation 1.11

where the subscript 1 and 2 indicate the type of the memory, SEU is the count of single event upsets for each memory, σ^{ThN} is the cross section of the memory for thermal neutrons, whereas σ^{HEH} is the cross section of the memory to high energy hadrons. The cross section can be thought as the capability for a particle to induce a SEU in the memory and it is calculated as the ratio of the SEU over the particle fluence, normalized by the memory size (i.e. measured cm^2/bit). It is an intrinsic parameter of the device that depends on the biasing of the chip and can significantly change from batch to batch. To characterize each batch, dedicated radiation campaigns are performed, where the device are exposed to pure mono-energetic beams. To determine the cross section for thermal neutrons, the memories were exposed to the thermal neutron beam generated by a nuclear reactor at the Institut Laue-Langevin in Grenoble, France. The cross section for high energy hadrons is obtained by exposing the memories to a 200 MeV proton beam at the PIF facility at Paul Scherrer Institute in Villigen, Switzerland. In order to increase the sensitivity of the measurement system, four memories of each type are employed. In such a system, the SEUs are evaluated as the sum of the counts of the four memories, and the cross section is calculated by normalizing by the size of the four memories.

The measurements of the Φ_{HEH} and Φ_{ThN} allows the calculation of an important parameter, which is helpful to understand the "harshness" of the radiation environment. This parameter is called R-factor and is defined as follows:

$$\mathrm{R} = \frac{\Phi_{ThN}}{\Phi_{HEH}}$$

Equation 1.12

The RadMon system has been conceived in a modular design, which allows easy maintenance and flexibility. The device is built on three printed boards, each of which is dedicated to a different task: the Power Board, the Main Board and the Sensor Board. The Power Board provides the voltage supply levels converting the 220 V of the electrical power distribution network. The Main Board hosts the brain of the system, an Actel ProAsic3 FPGA, which controls and monitor the peripherals and communicates with the outside. The Sensor Board hosts two banks made of four SRAMmemory chips to measure the Φ_{HEH} and Φ_{ThN}, three PIN diodes to measure the 1-MeV equivalent neutron fluence and two RadFETs for TID measurements. In addition, a fourth board called Deported Module can be connected to the RadMon via an up to 50 m long cable. The Deported Module can host two RadFETs and three PIN diodes, allowing the measurement of TID and DD in zones with very high radiation levels, where the RadMon would not survive.

Chapter 2 Total Ionizing Dose Sensors Based on Metal-Oxide-Semiconductor Structure

In this chapter, several aspects of MOS dosimetry will be analysed. Radiation-induced mechanisms that affect the functioning of MOSFET transistors will be reviewed and the main effects on the radiation response will be addressed to better understand the behaviour of semiconductor dosimeters based on MOS structures.

The characterization of two different kinds of MOS transistors used as dosimeters will be discussed to highlight their performance in terms of dose range, resolution and accuracy. The first device investigated is called RADFET (stands for RADiation-sensing Field Effect Transistor), which is a p-channel MOS transistor with an unusually thick layer of silicon dioxide. This device is well-known, since it has been extensively studied over time [12] and is largely employed for radiation monitoring in different environments, including the CERN's accelerator complex ([13], [14]) , irradiation facilities and space applications (e.g. [15], [16]). In this chapter, the characterization of measurements performed by means of the RADFET will be presented. The second device investigated is a commercial NMOS transistor, whose high radiation-sensitivity makes it a good candidate as TID dosimeter. The affordable cost of COTS components allows the purchase of large volumes, which can possibly integrate the use of the RADFET. Following the radiation test campaign reported in [17], which was performed to select radiation tolerant transistors available on the market, the high sensitivity to TID shown by the DMN601 NMOS transistor led to consider its use for ionizing radiation dosimetry. Irradiation experiments were consequently performed to characterize its radiation response and to investigate its suitability as radiation sensor. The tests were performed by exposing the devices to a pure gamma field, generated by means of a ^{60}Co source at the CC60 (CERN) facility. As results of the analysis, the calibration curve and the uncertainty on the measure performed by means of this device are obtained. The characterization of these sensors has been performed aiming at providing an effective method to measure the absorbed dose.

2.1 Basic Mechanisms

The understanding of the mechanisms behind the interaction between ionizing radiation and semiconductor devices based on metal-oxide-semiconductor structures is crucial for exploiting the change in the electrical parameters of the device with the aim of measuring the absorbed dose. In general,

in these devices several parameters are affected by ionizing radiation (e.g. transconductance, noise, channel leakage). Among them, the shift of the threshold voltage (shortly ΔV_{th}) is the observed parameter which allows the conversion of absorbed dose into an easily measurable quantity. Indeed, the V_{th} shift is extremely simple to measure with respect to the other affected parameters, as it is mirrored on the V_{gs} when the transistor works in saturation and the drain current is constant. The change in the V_{th} is the result of the cumulation of charge within the insulator layer of the metal-oxide-semiconductor sandwich, i.e. the silicon dioxide SiO_2 and at the border between the insulator and the semiconductor edge, i.e. $Si/\ SiO_2$ interface. The nature of these two contributions is partially different and their separation becomes important as they lead to various secondary effects (e.g. interface traps induce the degradation of the transconductance, whereas border traps are responsible for an increase in flicker noise [18]).In general, ionizing radiation induces long-term effects only in the oxides of integrated circuits (such as gate, field and buried oxides, Shallow Trench Isolations, LOCal Oxidation of Silicon, etc.), whereas the bulk suffers from transient effects, since the high mobility of holes and electrons in the silicon allows a fast recombination. To have a complete picture on the ionizing radiation effects on the MOS oxide, four major physical processes can be distinguished as follows:

- Generation and initial recombination;
- Holes transport;
- Charge trapping;
- Radiation-induced interface traps build up.

The band diagram of a MOS capacitor, whose gate and bulk terminal are respectively biased to positive voltage and ground, is depicted in Figure 7 [19], as well as the four processes acting in chronological order from left to right, starting from the arrival of the impinging particle represented by the wavy arrow. Initially, the impinging particle ionizes the atoms along its track, generating a certain amount of electron hole pairs, a fraction of which immediately recombines (process 1). The energy required to generate an electron hole pair in the SiO_2 has been investigated in several works (e.g. [20], [21]), although the most accurate measurement has been proposed in [22], where a value of 17 ± 1 eV is reported. Following the initial recombination, survived electron-hole pairs (shortly *ehps)* are separated by the electric field that pushes the two charges in opposite directions, according to their sign: electrons are swept towards the gate terminal that is quickly reached thanks to their high mobility (about 20 $cm^2/V{\cdot}sec$ [23]), whereas holes move slowly towards the substrate by means of a

particular transport mechanism, called *hopping transport* (process 2). During their travel, holes might fall in energy wells where they might be trapped (process 3). However, a portion of holes escapes to the trapping and reaches the substrate, where holes mobility is higher and they can be easily be neutralized. Depending on the position and the depth of the energy wells in the MOS structure, they are called respectively *oxide traps*, *border traps* or *interface traps*. This distinction is important because of their different effects on the radiation response of the device. In this regard, a major mechanism to be considered is the increase of the *interface trap* density with the radiation (process 4), which leads to an increase of probability for a carrier to be trapped. Moreover, the distance of the trap from the channel of the device and its energy depth are important parameters as they determine the probability of interaction with the carriers existing in the substrate.

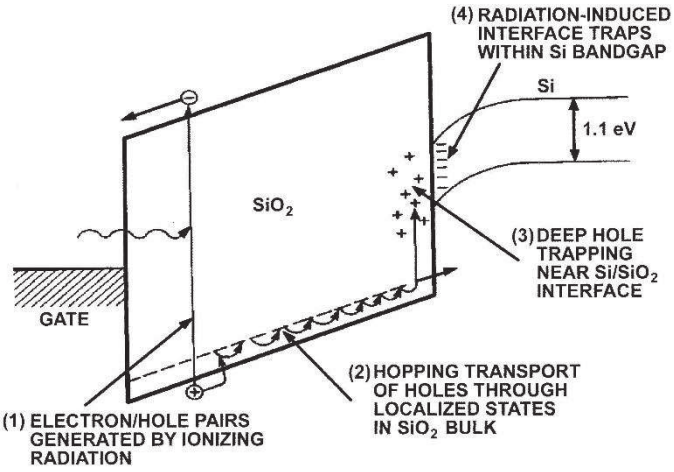

Figure 7. Main processes due to ionizing dose in the MOS insulator layer. (Source: [19])

2.1.1 Generation and Recombination

The number of *ehps* generated by ionizing radiation depends on the interaction of the impinging particle[2] and matter. All the particle properties having a direct impact on the number of pairs generated per unit dose, such as the kinetic energy and the species, can be condensated in the LET of the particle. Keeping into account the energy necessary to generate a single pair, the density of the target material (which results in 2.3 g/cm^3 for SiO_2) and the fact that one Gray corresponds to 6.24×10^{15} eV deposited in one gram of matter, one can calculate the density of *ehps* generated per unit of absorbed

[2] In this context, the term *particle* refers to any kind of radiation that ionizes the target material, including photons and ions.

dose, which results in 8.2×10^{14} Gy^{-1} cm^{-3}. However, only a portion of these pairs survives the recombination becoming available for trapping.

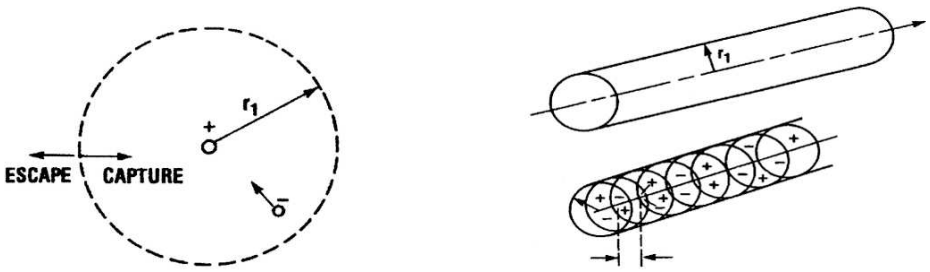

(a) Geminate Recombination (b) Columnar Recombination

Figure 8. Recombination models. (Source: [19])

Recombination of *ehps* is the first significant process that follows charge generation, determining a quick reduction of the initial density. Electrons surviving the recombination process will not contribute to the net charge which is responsible for the voltage threshold shift, since their high mobility allows them to escape in a time on the order of a few picoseconds (also depending on the applied field and on the oxide thickness). This happens even though no external voltage is applied: the electric field induced by the built-in potential due to the different work functions of the semiconductor and the metal is enough to move electrons inside the oxide. As a consequence, only the holes surviving the recombination can potentially contribute to the shift of the threshold voltage.

The fraction of electrons and holes that recombine depends on two factors: the intensity of the electric field in the oxide and the density of the cloud of *ehps* generated along the track of the ionizing particle. The former acts immediately after the generation, reducing the electron/hole recombination probability: the stronger the field, the lower the fraction of recombining *ehps*. The latter is determined by the LET of the particle and, as mentioned above, depends on the energy and on the type of radiation. According to the distribution of the generated *ehps* along the ionized track, recombination phenomena can be classified with two different models called *columnar recombination* and *geminate recombination*. To explain the differences between these processes, one can introduce a new parameter: the *thermalization distance*. For each pair, the thermalization distance is the separation between the hole and the corresponding electron when they reach the thermal equilibrium. The average value of this distance is known as *thermalization radius*. If the distance between two pairs is larger than a thermalization radius, then each electron can recombine only with the hole coming from the same pair: this process is known as geminate recombination (see Figure 8(a)). On the contrary, when

radiation induces a high density of *ehps* along the particle track and the distance between *ehps* is less than the thermalization radius, the individual *ehp* lose their identity and each electron can recombine with a hole belonging to a different pair, and vice versa. As a result, generated particles have a significantly higher probability to recombine than in the case of geminate recombination. The mathematical treatment of this process involves the modelling of high-density columnar distribution of *ehps* along the particle track, and, for this reason, this process is called columnar recombination (see Figure 8(b)). As it has been confirmed by several experiments, geminate and columnar recombination are triggered respectively by low-LET and high-LET particles. For instance, geminate model well describes ehps density generated by high-energy electrons, while columnar model is obtained by using high-LET particles, such as protons and alpha particles. In many cases of practical interest, both the models are necessary for describing the state of the irradiated lattice. To understand how the type of radiation influences recombination in the oxide, one can considers Figure 9, where the fraction of holes that survives the recombination process as a function of the electric field magnitude is shown for different types of radiation. As can be observed, the LET of the particle plays a crucial role on the fractional yield. Moreover, depending on the bias condition of the device, the amount of charge available to be trapped can change significantly.

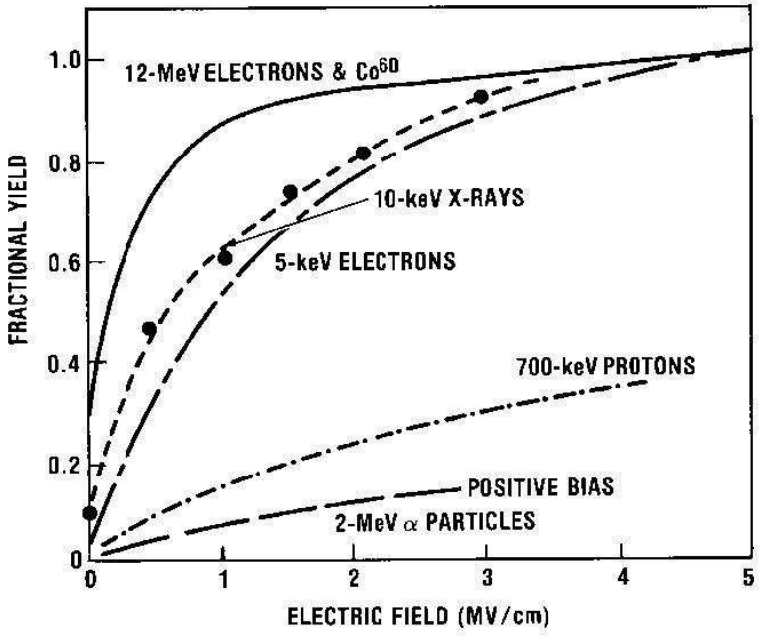

Figure 9. Fraction of charge escaping the recombination as a function of the Electric Field for different ionizing particles. (Source: [19])

2.1.2 Hopping Transport

The holes surviving the initial recombination move towards the silicon/silicon dioxide. The transport process is rather complicated, but some observations can be done to clarify the picture. Since holes are positive quasi-particles, they move towards the substrate under the effect the effective electric field. As the energy gap of the dioxide layer is extremely large, holes do not have enough energy to overcome this gap and to travel through the valence band: to make hole conduction possible, intermediate energy states are needed. These states are provided by interstitial defects due to oxide impurities, such as hydrogen. Due to thermal fluctuations, holes can hop from a trap energy state to the valence band and then travel through the oxide pushed by the electric field. When a hole bumps into a new oxide trap, it can be trapped one more time. Alternatively, if traps are sufficiently close to each other, it is possible for a hole to travel by moving from an energy well to a neighbouring one by means of tunnel effect. This second mechanism is activated by the electric field, which bends the energy band making the tunnelling possible [24]. In Figure 10, the two mechanisms are depicted.

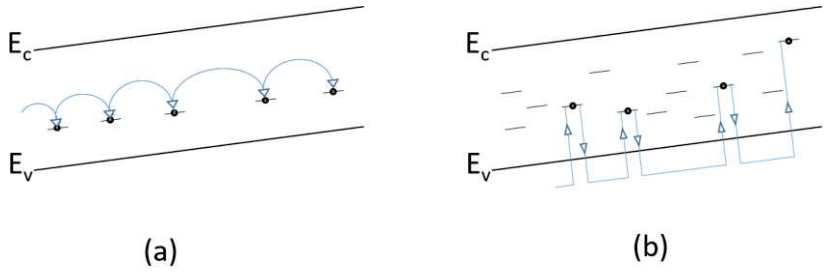

Figure 10. Hole travelling through the oxide by (a) tunnelling between traps and (b) by jumping from valance band E_v to shallow energy states.

Traps involved in the transport process are deeply localized in the oxide and their contribution to the net charge accumulation is not relevant. These traps are typically shallow and have energies located within 1.0 eV from the oxide valence band. As the trapping time can vary significantly, the transport process can change significantly in time, taking place over many decades. This large spread in the transit time is due to different elements, like the distance among traps and the difference in energy between the valence band and the generation/recombination center. However, the shape of the response on a log-time scale does not change by varying the temperature, the electric field and the oxide thickness [19].

The mathematical model that well describes the hole transport is called Continuous-Time Random Walk (CTRW): a complete review of the works analysing holes transport by this model is reported in [25]. The model is based on the idea that carriers jump from a trap to the next one at random time.

2.1.3 Charge Trapping

As already mentioned, in MOS dosimetry the electrical parameter monitored for measuring the absorbed dose is the radiation-induced V_{th} shift. This variation is the result of the sum of two different contributions: the oxide trapped charge and the charge captured by the interface traps. As it will be shown, it is important to separate these two components as they are responsible for different non-negligible effects. On this basis, it is convenient to express the voltage threshold shift as follows:

$$\Delta V_{th} = \Delta V_{ot} + \Delta V_{it}$$

Equation 2.1

Where ΔV_{th} is the voltage threshold shift, ΔV_{ot} is the contribution due to the oxide trapped charge and ΔV_{it} is the shift due to the charge trapped by the interface traps. Hereafter, the origin and the effects relevant to the two contributions are discussed.

2.1.3.1 Charge trapped in the oxide

Oxide traps that contribute to long-term charge accumulation are typically placed a few nanometers from the silicon/silicon dioxide interface. Their energies are located in the forbidden energy gap, more than 3 eV from the valence band of the oxide. These traps act like generation/recombination centers and are considered fixed, since external an voltage applied to the gate of the transistor does not change the state of the trap.

The origin of oxide traps lies in the imperfection of the SiO_2 lattice, which is affected by the change in the structure at the interface. Here, the transition region between the silicon and the silicon dioxide is limited to a few atom layers, where the lattice is a hybrid state between the two materials and it is often indicated as SiO_x. Although the dioxide becomes abruptly stoichiometric after the transition region, a large number of SiO_2 molecules within the first 4 nm from the interface show an anomalous angle between the *Si-O* bonds, which appears smaller than the one taken by the structure in the central part of the dioxide [26]. These strained bonds are particularly weak and can be easily broken by ionizing radiation [27], releasing oxygen atoms that migrate towards the bulk. The formation of these dangling bonds results in the so-called E' centers: their energy wells become the traps in which holes can fall. The distribution of this kind of defects increases in the transition region from SiO_2 to *Si*, and it is the main responsible of the charge accumulation in the silicon dioxide.

To quantify the effect of the oxide trapped charge on the ΔV_{th}, one can consider the MOS structure as a capacitor, with a thin layer of positive charge Q_{ox} [C/cm^2] trapped in the oxide at distance x_d from the gate: Q_{ox} will induce the same quantity of charge with the opposite sign in order to reach the neutrality of the system. This charge, which is properly called image charge, will be shared between substrate (Q_S) and metal of the gate (Q_G) if no bias is applied. It is easy to understand that the closer Q_{ox} to the interface, the larger the portion of image charge induced in the substrate with respect to the gate. However, the charge distribution does not violate the charge conservation law, which can be expressed as follows:

$$Q_{ox} = -(Q_S + Q_G)$$

Equation 2.2

The system configuration described above is depicted in Figure 11 (a). To calculate the shift of the I_d-V_g characteristic, one can apply a voltage on the gate of the capacitor to compensate both the effect of the extra-charge and the work function difference and obtain the flat band condition in the system. In this condition, the whole image charge is transferred to the metal plate of the capacitor (see Figure 11 (b)). Thus, it can be stated that the variation of the flat-band voltage with respect to its pre-irradiation value (i.e. when no extra-charge layer is present in the insulator), depends only on the charge that is trapped in the oxide. By applying the Gauss's law it is possible to calculate the electric field in the oxide, which is null for $x > x_d$, while for $0 < x < x_d$ is constant and given by

$$\mathcal{E}_{ox} = -\frac{Q_{ox}}{\varepsilon_{ox}}$$

Equation 2.3

where $\mathcal{E}_{ox}$ is the electric field in the oxide, ε_{ox} is the permittivity of the dielectric, given by the product between the relative permittivity of the material ε_r and the permittivity of the free space ε_0, and Q_{ox} is the charge layer trapped in the oxide. Hence, the flat-band shift induced by the charge layer Q_{ox} is given by

$$\Delta V_{FB} = x_d \mathcal{E}_{ox} = -\frac{x_d \cdot Q_{ox}}{\varepsilon_{ox}}$$

Equation 2.4

Where x_d is the distance of the trapped charge layer from the gate, ΔV_{FB} is the shift induced by the charge trapped in the flat-band voltage.

This equation allows to highlight that the effect on the voltage shift changes depending on the position of the charge layer in the oxide: charge placed close to the gate does not have significant influence on the flat-band voltage shift, whereas charges trapped near the interface (or at the interface) has the strongest effect.

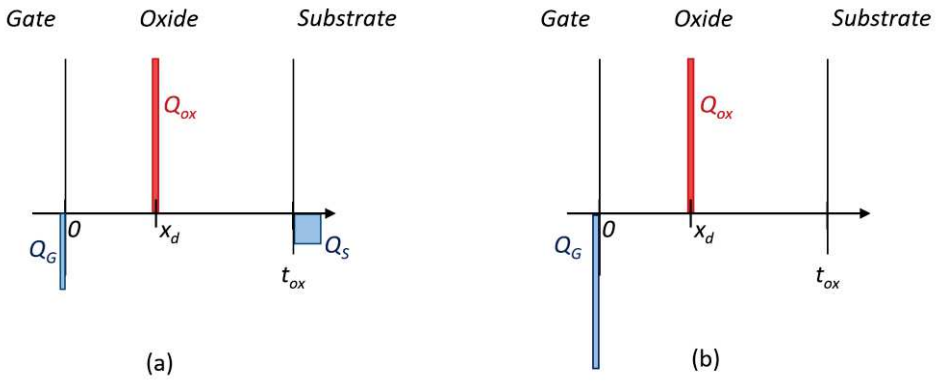

Figure 11. Charge distribution in the MOS system when (a) no bias is applied and (b) a V_g is applied to obtain the flat band condition

The effect of a charge distribution *ρ(x)* that involves the whole oxide, such as the one generated by ionizing radiation, can be evaluated by dividing the insulator in several slices, each of which characterized by its charge layer Q_{ox} whose thickness *dx* is infinitesimal, and summing each contribution. Considering the capacitor relationship, it is possible to express the shift of the characteristic induced by the oxide trapped charge as follows:

$$\Delta V_{ot} = \frac{-1}{C_{ox}\, t_{ox}} \int_0^{t_{ox}} x \cdot \rho(x)\, dx$$

Equation 2.5

ΔV_{ot} can be thought as the equivalent charge at the interface divided by the capacitance, where the integral in the formula represents the equivalent charge at the interface corresponding to the distributed trapped charge in the oxide, weighted for the distance. Considering that the charge trapped in the oxide is positive, the corresponding shift of the characteristic is different depending on the sign of the carriers: for n-channel transistors, the curve will be moved towards lower voltages, whereas for p-channel transistors, it will be pushed towards higher V_g, as shown in Figure 12. In other words, ionizing radiation reduces the magnitude of the threshold voltage for nMOS transistors and increases the one of pMOS transistors. Moreover, since oxide traps affect exclusively the V_{th} of the device, the curve will rigidly shift without being stretched-out.

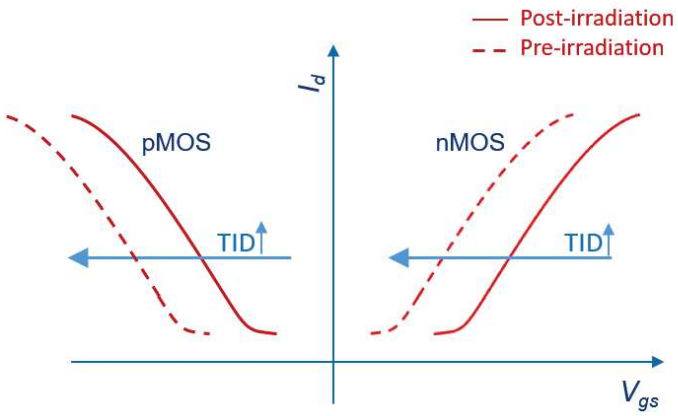

Figure 12. Effect of the positive trapped oxide charge on the pMOS (left) and nMOS (right) I_d-V_{gs} characteristic

In addition, among oxide traps, traps very close to the silicon/silicon dioxide interface may affect the transistor operation by electrically communicating with the channel. Indeed, the closer such traps are to the interface, the larger is the probability to interact with the carriers. Holes and electrons can be caught or released from/into the channel through tunnelling. Charge trapped in these sites (so-called *border traps*), besides being responsible for a threshold shift, may degrade the mobility of the carriers in the channel. Moreover, it has been shown that they are responsible for the increase in flicker noise of MOS transistors [18].

2.1.3.2 Charge trapped at the interface

Interface traps are located within two atomic bonds from the substrate, in the transition region between the silicon and the oxide: along this surface, the periodic nature of the semiconductor is interrupted, allowing further energy states within the forbidden energy gap. Silicon atoms belonging to the silicon layer adjacent to the oxide layer do not complete all their covalent bonds as they do inside the oxide bulk. The same happens to the SiO_2 molecules close to the interface. All these incomplete atom bonds are potential wells in which carriers can fall.

This kind of traps are process-induced as they depend on the structure of the MOS capacitor and, for these reason, they cannot be avoided. However, the density of interface traps increases with radiation, which adds to the existing states, the so-called radiation-induced interface traps, as it will be explained in Section 2.1.4.

The typical *U-shaped* energy distribution of the interface states within the oxide gap [28] and their closeness to the bulk facilitate the exchanging of charge with the channel. Indeed, since no barrier shields the channel from their effect, trapping and de-trapping phenomena are much more frequent for interface traps rather than for oxide border traps.

Due to these features, interface traps behave differently from oxide traps. In fact, interface traps are amphoteric, meaning that they can be negatively or positively charged depending on their energy within the energy gap and the biasing of the structure. The following classification will be helpful to explain the change induced in the I_d-V_g characteristic: they are called *donor-like* traps if positively charged when empty and neutral when filled with an electron, whereas they are called *acceptor-like* traps if neutral when empty and negatively charged when filled with an electron. In other words, a *donor-like* trap is positive (neutral) when its energy is above (below) the Fermi level. On the contrary, an *acceptor-like* trap is neutral (negative) when its energy is above (below) the Fermi level. It has been demonstrated that interfaces states whose energy is below the mid-gap are *donor-like* traps, while interface traps whose energy is below the mid-gap are *acceptor-like* traps [29]. This means that when the system is biased to have the Fermi level at mid-gap level at the interface, all the interface states are neutralized, regardless of their nature: biasing the transistor in this way allows to evaluate the amount of oxide trapped charge and to separate the two contributions to the V_{th} shift [30].

It is important to notice that the magnitude of the effect of the interface traps on the I_d-V_g characteristic depends on the bending of the energy bands, and therefore on the biasing condition. In fact, a voltage applied to the gate of the transistor moves the energy level for each trap, as well as the conduction and valence band energy, with respect to the Fermi level. As a consequence, the sign of the trap state changes as soon as it crosses the Fermi level, turning into its more positive charge state when it overcomes the Fermi level, regardless if the trap is acceptor or donor-like. This implies that the effect on the I_d-V_g curve changes depending on the applied V_g.

Ideally, if the biasing pushes all the interfaces above the Fermi level, then they will shift the V_{th} in the same direction of a (positive) oxide trapped charge. To meet this condition, an n-type substrate (i.e. p-channel MOSFET) should work in inversion, whereas a p-type substrate (i.e. n-channel MOSFET) should work in accumulation. On the contrary, biasing the system in such a way to push all the interface states below the Fermi level, the shift of the V_{th} would be the opposite of the one given by positive oxide trapped charge. Accordingly, to obtain this effect, the transistor should work in inversion if the substrate is n-type, or accumulation if the substrate is p-type. These two border conditions allow to highlight that the direction of the V_{th} shift induced by the interface traps changes depending on the sign of the carrier: when the transistor conducts (i.e. the channel is inverted), the threshold voltage decreases for pMOS and increases for nMOS. Furthermore, this consideration helps to understand what happens when the population in the channel varies from depletion to accumulation, i.e. when the transistor works in *sub-threshold* ($V_{gs} < V_{th}$). Due to technology scaling, it has become more and more crucial over time to look closely at the density of carriers in these working region, which is

nowdays exploited as operational mode as much important as the cut-off, linear and saturation region. When the transistor works in sub-threshold, the change in the V_g gradually fills both acceptor-like and donor-like traps with electrons. The result of this progressive change in the V_{th} shift is the stretching out of I_d-V_g characteristic for $V_{gs} < V_{th}$, whose slope decreases as the density of interface states increases.

The contribution to the threshold voltage shift due to the interface trapped charge can be calculated in the same way as for the oxide trapped charge in the previous section, keeping into account that (i) interface traps are amphoteric and (ii) their distance from the gate is fixed to t_{ox}. According to Equation 2.5, the voltage shift due to the interface charge can be calculated as:

$$\Delta V_{it} = \pm \frac{t_{ox} \cdot Q_{it}}{\varepsilon_{ox}} = \pm \frac{Q_{it}}{C_{ox}}$$

Equation 2.6

Where Q_{it} is the superficial charge density at the interface, which is proportional to the interface traps density N_{it}, and the sign ± is necessary as the shift direction changes depending on the sign of the carriers in the channel, which determines the sign of the trapped charge.

2.1.4 Radiation-induced Interface Traps

As discussed in the previous section, the transition region between the subtrate and the insulator has a significant number of interface traps due to the different atomic structure of the two materials. In addition, several studies showed that the density of traps available at the interface increases with the radiation. The formation of new interface states is believed to be induced by hydrogen ions (protons) that are released when a hole jumps into an energy well during its travel towards the substrate, as well as when it is trapped in a long-term site (such as oxygen vacancies). Indeed, hydrongen is largely employed during the growing process of silicon dioxide to passivate dangling bonds due to both the structures mismatch at the interface and defects in the dioxide itself. The electric field pushes the released protons towards the Si/SiO_2 interface, where the density of strained Si-O bonds increases. Here, protons interact with Si-O bonds generating interface traps from the cleaving of the bonds [31].

The density of interface traps increases sub-linearly with the dose [32], although no-saturation has been observed for doses up to 10 kGy. This dependency has been explained by considering the repulsive interaction between interface trapped charge and holes travelling towards the substrate, which would decrease the effective amount of measurable trapped charge [33].

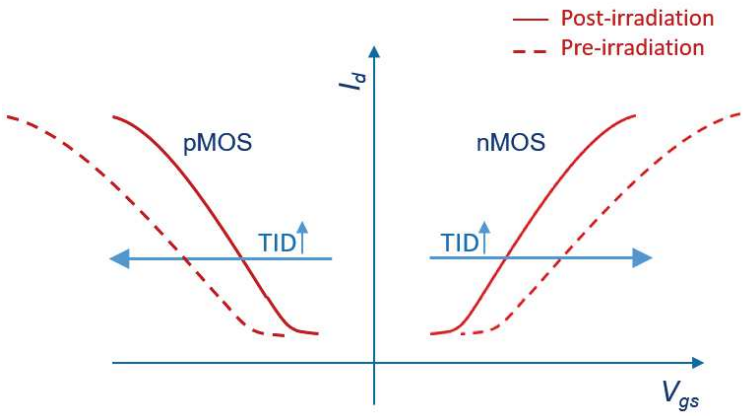

Figure 13. Effect of the amphoteric interface traps on the pMOS (left) and nMOS (right) I_d-V_{gs} characteristic.

The increase of the density of interface states leads to a major effect that is often non-negligible in MOS devices: as the number of the trapped carriers at the interface increases, the Coulomb interaction with the carriers becomes important, resulting in a reduction of the drift velocity in the channel. This leads to a degradation of the mobility that can be expressed through the following experimental relationship [34]:

$$\mu = \frac{\mu_0}{1 + \alpha(\Delta N_{it})}$$

Equation 2.7

where μ_0 is the pre-irradiation mobility, ΔN_{it} is the density of radiation-induced interface states and α is a parameter whose value, $(8 \pm 2) \times 10^{-13}$ cm^2, can be experimentally determined [35]. The mobility degradation directly affects the transconductance of the transistor and therefore the charateristic of the transistor, which will be stretched out. In Figure 13, the effect due to the combination of the two contributions resulting from the interface charge trapping (i.e. the V_{th} shift) and the mobility degradation, is depicted for both p- and n-channel MOSFET.

2.2 Reading Circuit

The reading circuit embedded in the RadMon system has been conceived to measure the dose by means of the RADFET, which can be placed either on the sensorboard or on the deported module. The former is housed on the RadMon, whereas the latter is connected to the sensorboard via cable in order to perform the measurements in those cases where the circuitry embedded in the RadMon could not work properly due to the high radiation levels [36].

The method employed to measure the V_{th} shift is simple. The idea behind the RadMon's reading circuit is to keep the transistor working in the saturation region and to force the drain current through

an external current source: in this way, the threshold voltage shift pushes the transistor to change the voltage between gate and source, to provide the same current. For the sake of simplicity, the expression of the current when the transistor works in saturation should be considered:

$$I_{sd} = \frac{1}{2}\mu C_{ox}\frac{W}{L}\left(V_{sg} - |V_{th,p}|\right)^2$$

Equation 2.8.

where μ is the charge-carrier effective mobility, W is the gate width, L is the gate length, C_{ox} is the gate oxide capacitance per unit area, and V_{sg} is the voltage drop between the source and the gate. Looking at this formula, it is clear that the V_{sg} must change as much as the V_{th} does in order to keep the current constant. To force the transistor into saturation mode, the drain and the source are shorted (the transistor is configured in the so-called *diode mode*), so that the saturation condition is always met:

$$V_{sd} > V_{sg} - |V_{th,p}|$$

Equation 2.9

The resulting circuit reading a pMOS transistor, such as the RADFET, is depicted in Figure 14 (a), where the shift of the output voltage V_{out} corresponds to the V_{sg} shift, and therefore to the ΔV_{th}.

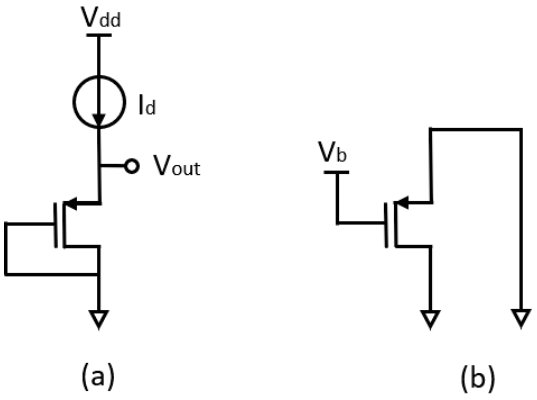

Figure 14. Reading circuit during (a) the measurement of ΔV_{th} and (b) the irradiation phase

To apply the proper bias to the sensor during the irradiation, the ΔV_{th} is not continuously read but is sampled with a certain frequency. Between each reading, the RadMon system allows to bias the RAD-FET in two different ways, configuring the circuit as shown in Figure 14 (b): (i) grounding all the pins of the transistor, or (ii) biasing the gate at +5V and connecting the drain and the source to ground. The latter configuration allows to obtain a much higher sensitivity, as the higher electric field in the oxide of the transistor decreases the recombination rate, resulting in a larger amount of collected

charge per unit dose. Since this biasing implies a larger variation of the output of the reading circuit, the measurable resulting dose range is lower. Indeed, the output of the reading circuit is converted in a digital number by means of a 16 bit ADC converter, whose full scale input is 5 V. To maximise the measurable dose range, a configurable resistive divider is placed between the reading circuit and the ADC in order to reduce the voltage input of the ADC when it overcomes 5V.

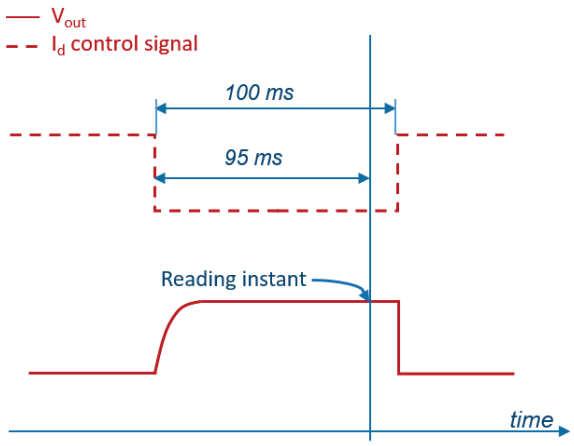

Figure 15. Reading portocol

In the reading protocol implemented on the RadMon, the current is set up as shown in Figure 15. The current flows in the channel over a period of 100 ms, while the V_{out} is read after 95 ms since the source current has been switched on. The duty cycle of the current square wave is 5%, which means that the current is off over a period of 1.9 s. Moreover, limiting the period of time during which the current flows in the transistor avoids the heating of the device.

2.3 RADFET - Radiation Response Characterization

The characterization of the radiation response for the RADFET employed at CERN by means of the RadMon system has been summarized in [36], where the radiation response of devices with different oxide thickness (100 nm and 400 nm) and operated in different bias condition (0V and 5V) was investigated with different radiation sources (γ-rays and 230 MeV proton beam) and temperatures (25 and 40 °C). Following this investigation, the higher reliability shown by the 100nm RADFET with respect to the thicker 400nm RADFET discouraged the use of the latter, although it would allow to reach higher sensitivity if biased to 5V. The calibration curve resulting from the characterization of a 100nm RADFET biased to 0V and 5V respectively is shown in Figure 16, along with the accuracy of ±8 % resulting from the analysis [36].

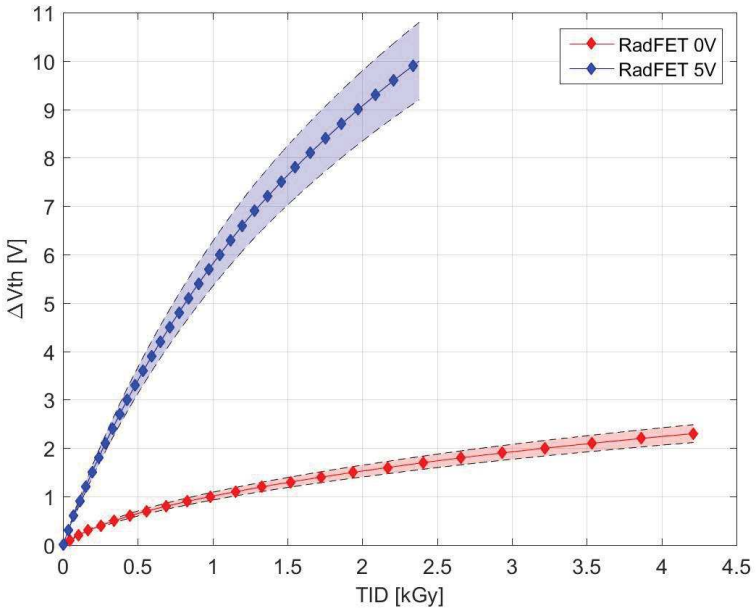

Figure 16. Calibration Curve for the 100nm RADFET biased to 0V (in red) and 5V (in blue).

The sensitivity of a silicon dosimeter is an important parameter as it determines the minimum detectable dose value that can be read by the sensor. It can be defined as the derivative of the voltage shift over the dose, i.e.:

$$S \triangleq \frac{\partial \Delta V_{th}}{\partial TID}$$

Equation 2.10.

As it can be deduced by the formula, since the radiation response of MOS dosimeters is sub-linear [37], the sensitivity will decrease over the dose, affecting the resolution. The sensitivity variation and the V_{th} variation is reported in Figure 17 and Figure 18, respectively for the RADFET biased to 0V and 5V. At the beginning of the irradiation, the biasing at 5V allows to obtain a sensitivity ~17 times higher than the RADFET biased at 0V.

The significant increase of fluctuations on the sensitivity of the RADFET biased at 5V at ~1.8 kGy (see Figure 19) is due to an actual increase of the noise in the detected V_{th} shift, although it is not evident from the plot. In fact, to avoid exceeding the input range of the ADC, the voltage divider has been enabled, significantly degrading the signal-to-noise ratio. This action was not necessary for the RADFET 0V, as the output voltage does not increase dramatically.

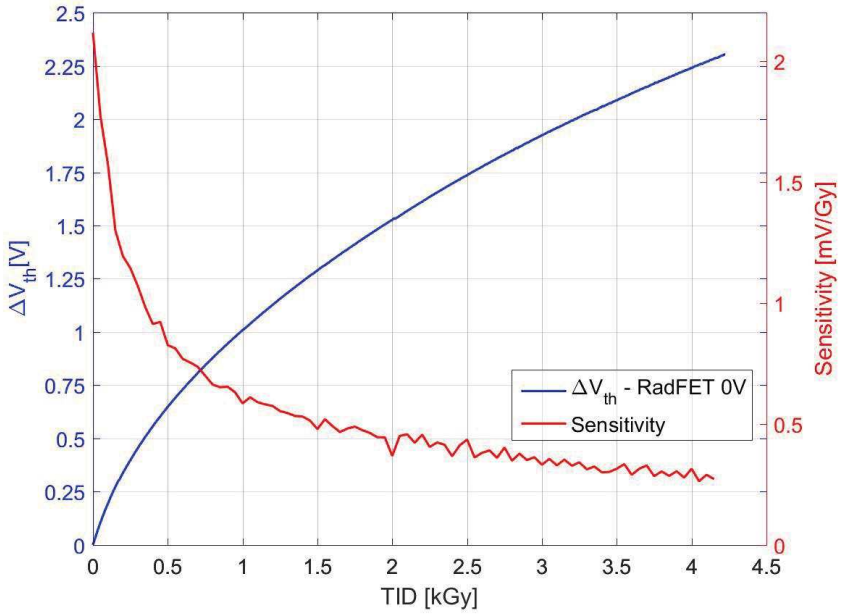

Figure 17. ΔV_{th} (in blue) and Sensitivity (in red) as a function of the dose for the RADFET biased to 0V.

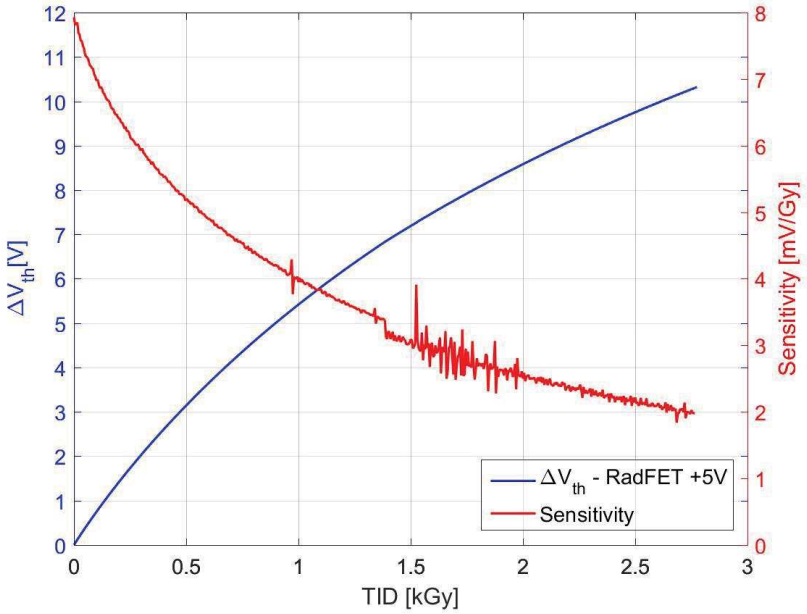

Figure 18. ΔV_{th} (in blue) and Sensitivity (in red) as a function of the dose for the RADFET biased to +5V.

To calculate the dose resolution, it is necessary to consider the minimum voltage variation readable by the readout system, V_{min}., which depends on the ADC resolution and on its noise. Since the Least Significant Bit (LSB) of the RadMon's ADC is 150 µV, considering an ADC noise of 3 LSB, the minimum

detectable voltage is 450 µV. The dose resolution can be calculated as the ratio between V_{min} and the sensitivity:

$$Resolution = \frac{V_{min}}{S} = \frac{3 \times 150\mu V}{S}$$

Equation 2.11

The dose resolution and the sensitivity versus the TID are reported in Figure 19 and Figure 20 for the two bias configurations. At the beginning of the calibration curve, the RADFET can provide a dose resolution of 212 and 57 mGy, respectively when biased at 0V and 5V. The decrease of the sensitivity with the dose makes the minimum detectable dose increasing with a rate of 350 µGy and 55 µGy per Gy, respectively for the RADFET biased at 0V and 5V.

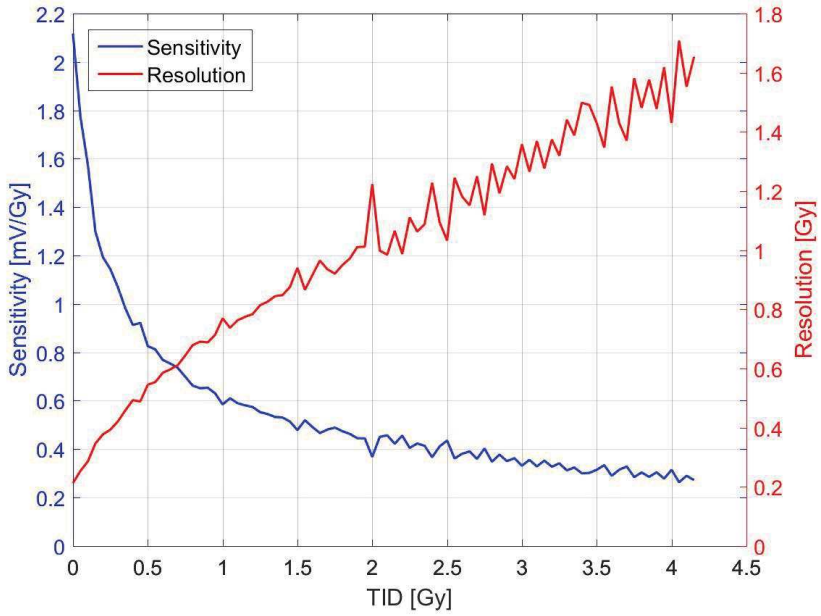

Figure 19. Sensitivity (in blue) and Resolution (in red) as a function of the dose for the RADFET biased to 0V.

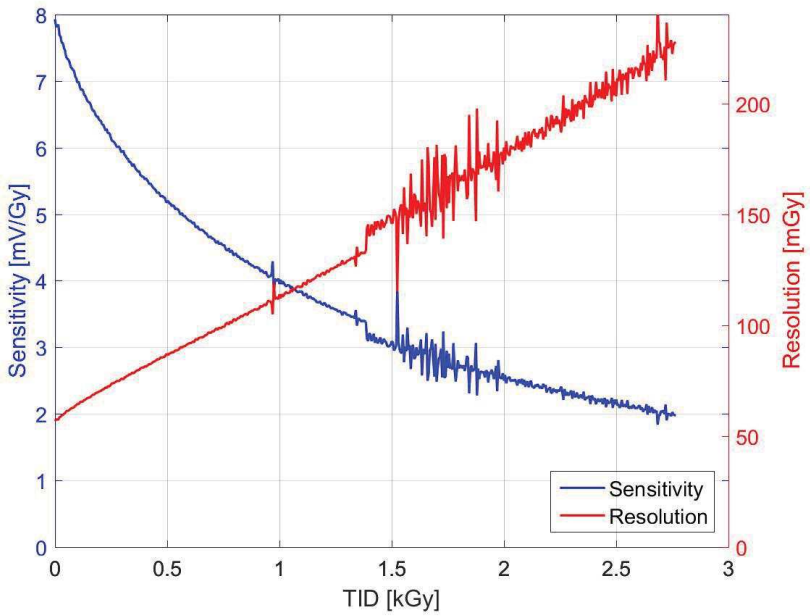

Figure 20. Sensitivity (in blue) and Resolution (in red) as a function of the dose for the RADFET biased to +5V.

2.4 NMOS - Radiation Response Characterization

The characterization of the radiation response is a necessary step to employ the NMOS as ionizing radiation detector. For this purpose, the calibration curve shall be obtained, as well as the measurement error. For this reason, several irradiations were performed at the CC60 facility at CERN, where a gamma field is generated by a ^{60}Co source.

The calibration curve of the sensor has been obtained by exposing the device to a dose rate of 2.7 Gy/h. In Figure 21, the V_{th} shift and the sensitivity are plotted against the TID. As can be observed, the initial sensitivity is ~5.3 mV/Gy and, as well as for the RADFET, it decreases with the dose.

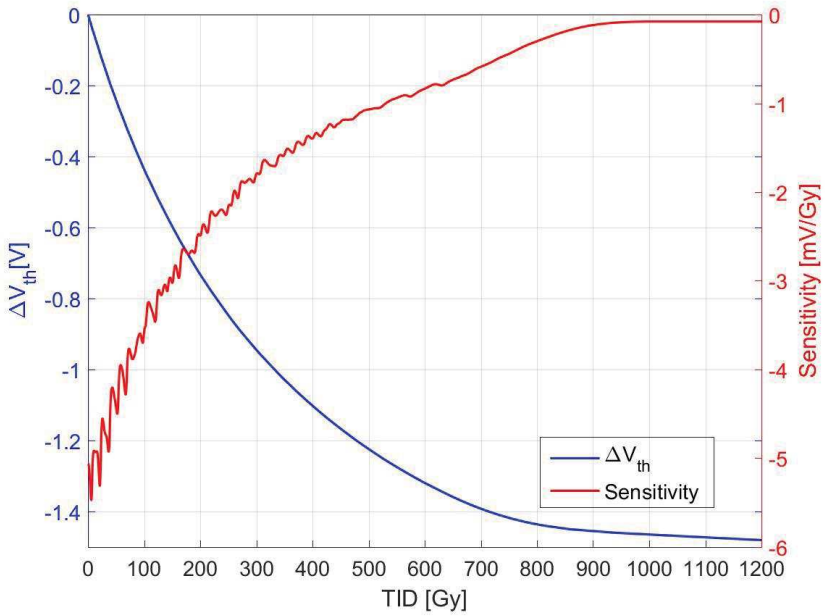

Figure 21. ΔV_{th} (in blue) and Sensitivity (in red) as a function of the dose.

In Figure 22, the resolution and the sensitivity are plotted against the dose. At the beginning of the irradiation, the dose resolution is ~90 mGy. However, due to the intrinsically non-linear radiation response of MOS devices, the slope of the curve decreases with the dose. As a consequence, the minimum detectable dose increases. Moreover, it is worth noting that the dose resolution trend abruptly changes between 600 and 800 Gy. This is due to the transfer function of the reading circuit, which is linear as long as the output voltage does not approach 0V.

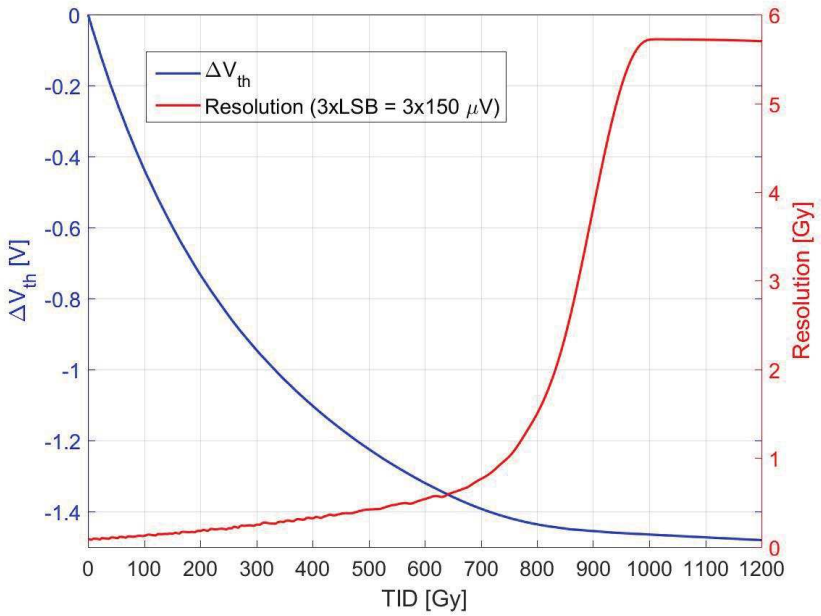

Figure 22. Sensitivity (in blue) and Resolution (in red) as a function of the dose.

A zoom on Figure 22, corresponding to the first 800 Gy, is plotted in Figure 23. In this plot it is possible to appreciate the limited degradation of the dose resolution in the first part of the irradiation. In particular, it is possible to detect dose variations larger than 420 mGy for doses lower than 500 Gy.

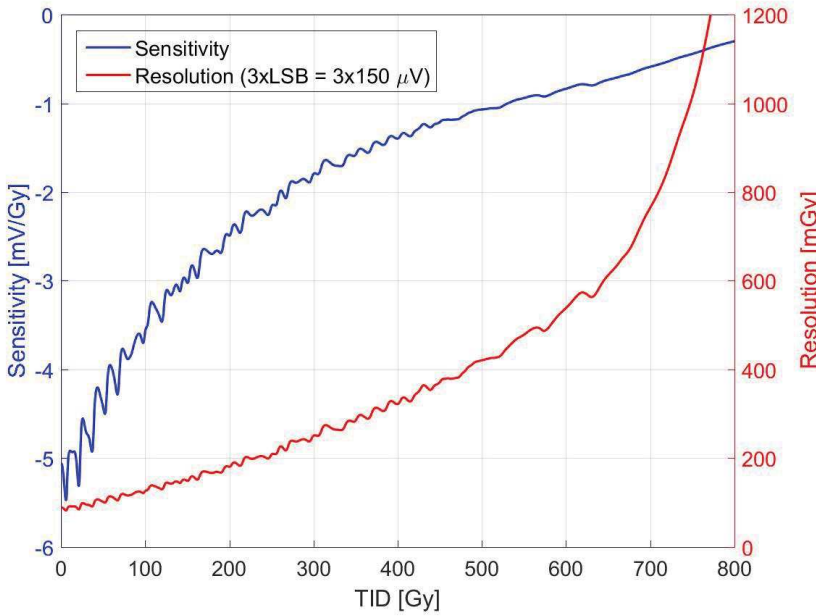

Figure 23. Sensitivity (in blue) and Resolution (in red) as a function of the dose – Zoom of Figure 22.

2.4.1 Sample-to-Sample variability

The radiation response of each sample can be slightly different due to the fabrication process variability, even though the samples belong to the same batch. Hence, the uncertainty introduced on the dose measurement must be evaluated. For this aim, the radiation responses of four samples irradiated in the same conditions were compared. The samples were irradiated up to ~150 Gy with a dose rate of 2.7 Gy/h.

The radiation response of the four samples is plotted in Figure 24, where the curve corresponding to each sensor is plotted in blue and the black line represents the mean of the curves. The red area around the average curve represents the spread among the sensors using a coffidence interval of 95%. The amplitude of the confidence interval has been computed considering a Student's t-distribution rather than a Gaussian distribution, because of the limited number of samples. It must be kept into account that the error on the radiation response of each sensor includes the error introduced by the reading system (i.e. the RadMon), and the uncertainty in the dose measurement given by the facility (by means of a ionization chamber).

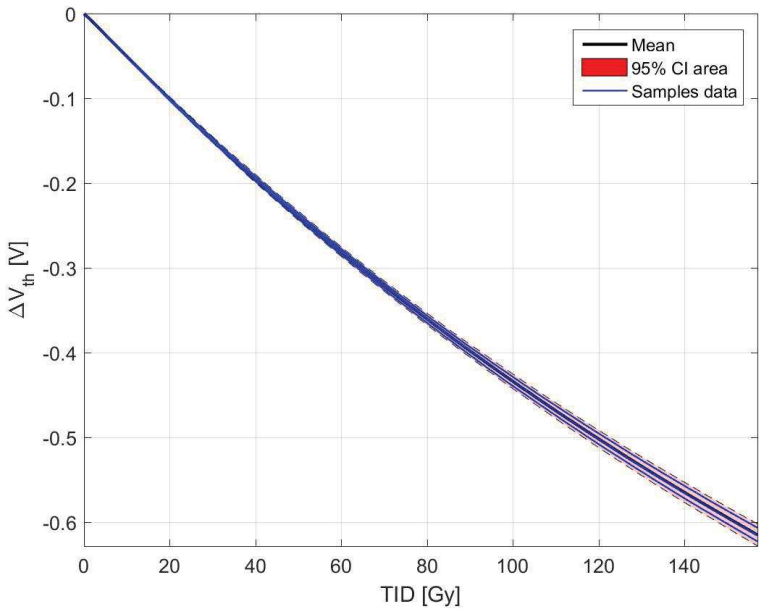

Figure 24. Sample-to-Sample variability – Radiation response obtained for four NMOS irradiated in the same conditions (in blue). The mean of the curves is plotted in black and the area corresponding to the 95% confidence interval is plotted in red.

The relative error, calculated as the percentage variation of the dose measured by each sensor with respect to the absorbed dose (i.e. measured by the ionization chamber), is plotted in Figure 25. In the same figure, the error introduced by considering the 95% confidence interval is shown.

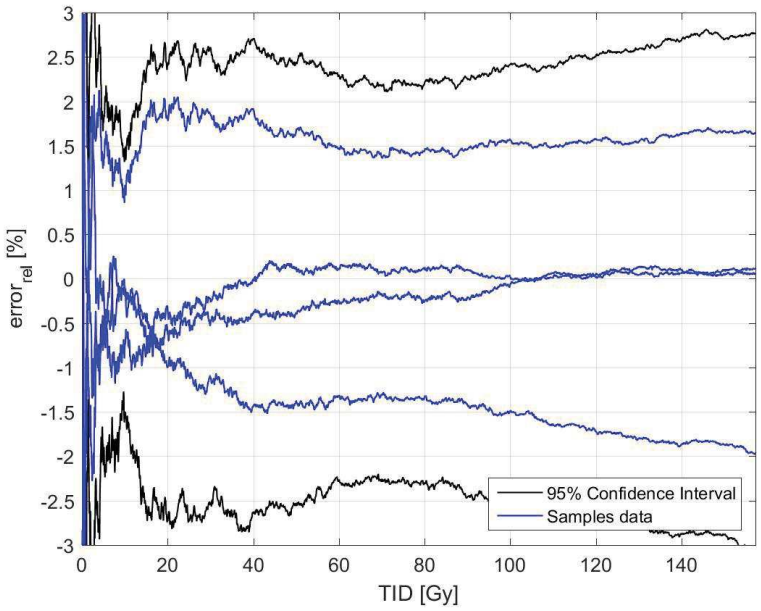

Figure 25. Relative Error – The error made by measuring the dose with respect to the absorbed dose is plotted in blue for each sample. In black, the error considering the 95% confidence interval

2.4.2 Batch to Batch variability

Considering the large amount of sensors necessary to monitor the radiation in large distributed facilities such as the CERN's accelerator complex, it is necessary to verify that sensors belonging to different batches show similar behaviour under radiation. Therefore, following the purchase of a new batch of NMOS transistors, the consistency of the radiation response has been verified by comparing three NMOS belonging to the new batch with the calibration curve obtained with the sensors belonging to the old batch (see Figure 26). The samples were irradiated up to 800 Gy with a dose rate of 5.6 Gy/h. Due to a malfunctioning of the air conditioning system, during the irradiation the sensors underwent to periodical temperature fluctuations, whose amplitude was about 2 °C. Since this NMOS has a temperature sensitivity of -4 mV/°C (as discussed in Section 2.4.3), the voltage variation has been com-

pensated. However, due to the limited resolution of the temperature sensor (which is the *pt100* installed on the deported module and read by the RadMon ADC), the temperature effect is not completely removed.

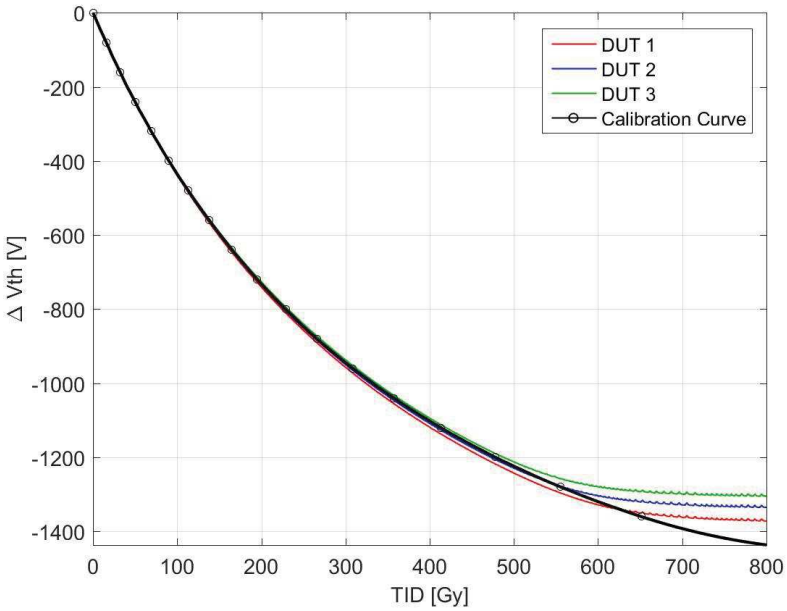

Figure 26. Batch-to-Batch variability – Radiation response of three sensors belonging to the new batch compared with the calibration curve.

As can be seen, the curve of the sensors belonging to the new batch are very similar to the calibration curve, although their response becomes considerably flat for doses higher than 650 Gy, contrary to the calibration curve.

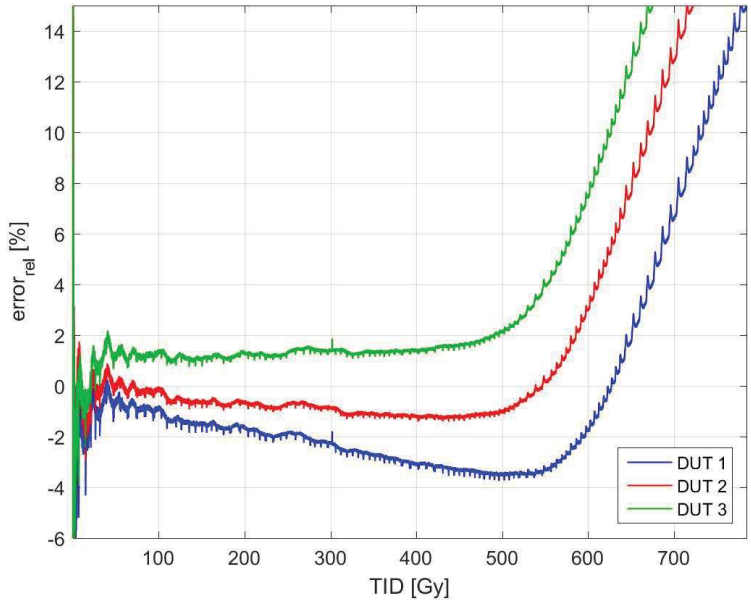

Figure 27. Relative Error - The error has been calculated as the percentage difference between the absorbed dose and the dose measured by the considered DUT.

To quantify this mismatch, in Figure 27 the relative error of the dose measured through the calibration curve with respect to the absorbed dose is plotted for each sensor. As observed, the error is relatively low (within ± 4%) for doses lower than ~550 Gy, which is consistent with the error due to the sample-to-sample variability and the measuring system. However, a significant increase can be noticed after this dose value. To explain this behaviour, it is necessary to consider that the output voltage of the reading circuit cannot drop below ground. Moreover, its trans-characteristic becomes non-linear when the output voltage approaches 100 mV. As discussed in Section 2.3, the full calibration curve shown in Figure 21 has been obtained by irradiating sensors belonging to the old batch, whose initial voltage is within 1.4 and 1.5 V. On the other hand, the initial voltage at the output of the reading circuit for the sensors belonging to the new batch is found to be ~100 mV lower with respect to the old batch. Consequently, using the new batch, the output voltage approaches the ground earlier, and the effect of the non-linearity due to the reading circuit makes the radiation response flat. This effect is clearly visible in Figure 26 for doses larger than 650 Gy.

The measurable dose range must be consequently limited to 550 Gy to keep the error within ± 4%. Nevertheless, the reading circuit might be changed in order to extend the dynamic range of the sensor.

2.4.3 Temperature Characterization

The influence of the temperature on the V_{th} of the NMOS transistor has been characterized by measuring the voltage variation (by means of the RADMON), while a controlled temperature profile was applied. The effect of the temperature on the ouput voltage of the transistor must be investigated to understand whether temperature fluctuations introduce an error on the dose measurement. The diagram of the experiment is represented in Figure 28. The DUTs were placed in an oven, whose temperature profile was programmed as depicted in Figure 29, while the temperature was monitored by means of a pt100 probe, which was read by a DAQ. In order to verify that the temperature dependency does not change over the irradiation, the experiment was repeated after irradiating the DUTs up to 400 Gy.

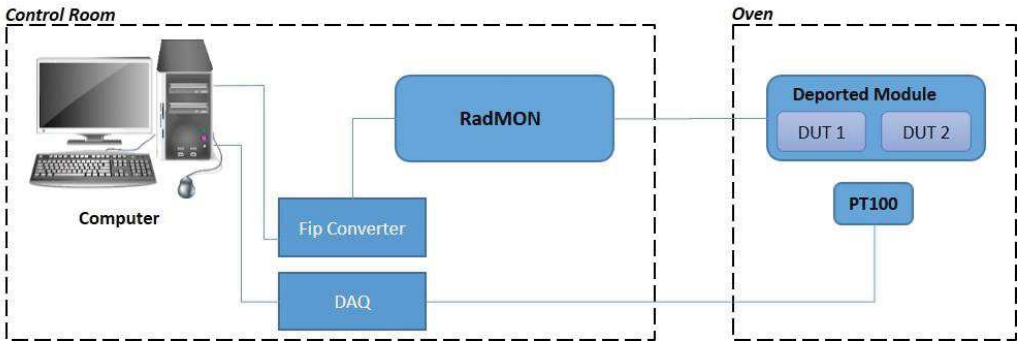

Figure 28.Temperature test setup

In Figure 30, the voltage variation against the temperature is plotted for both the pre and post irradiated sensor. The resulting temperature coefficient is -4 mV/°C and 3.9 mV/°C, respectively.

This means that for temperature variation of 1°C, the output voltage variation is 4 mV. Considering the sensor at the beginning of its calibration curve (where the sensitivity is 5.3 mV/Gy), this voltage variation would lead to a dose error of 0.75 Gy. However, as the sensitivity decreases with the dose, the error due to the temperature variation increases. For instance, considering that the sensitivity at 500 Gy is ~1 Gy/mV, a temperature variation of 1°C would lead to a dose error of 4 Gy.

The effect of the temperature can be easily compensated by measuring the temperature by means of a sensor (e.g. a thermocouple) and the accounting for the voltage variation through the temperature sensitivity, before converting the V_{th} shift into dose. The compensated V_{th} shift can be expressed as:

$$\Delta V_{tc} = \Delta V_{raw} + S_t \times \Delta T$$

Equation 2.12

where ΔV_{tc} is the temperature-compensated output voltage, ΔV_{raw} is the voltage variation read at the output of the reading circuit, S_t is the temperature sensitivity coefficient and ΔT is the temperature variation.

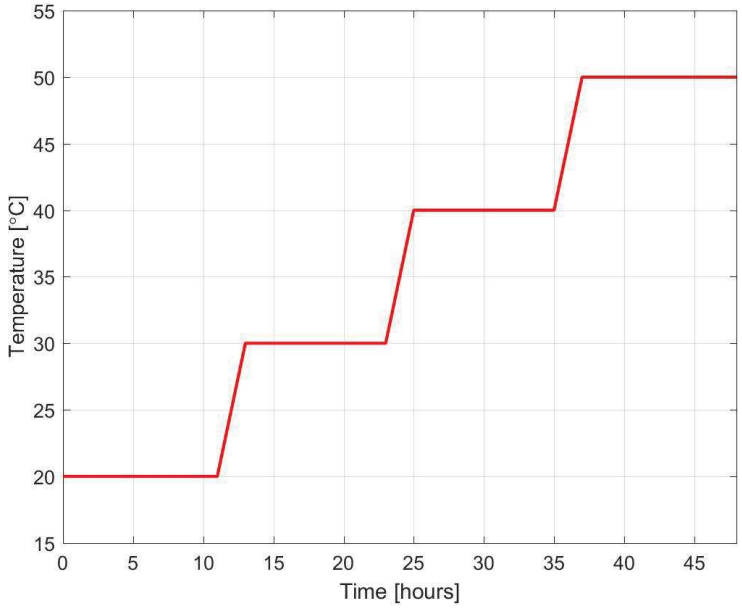

Figure 29. Temperature profile applied during the experiment

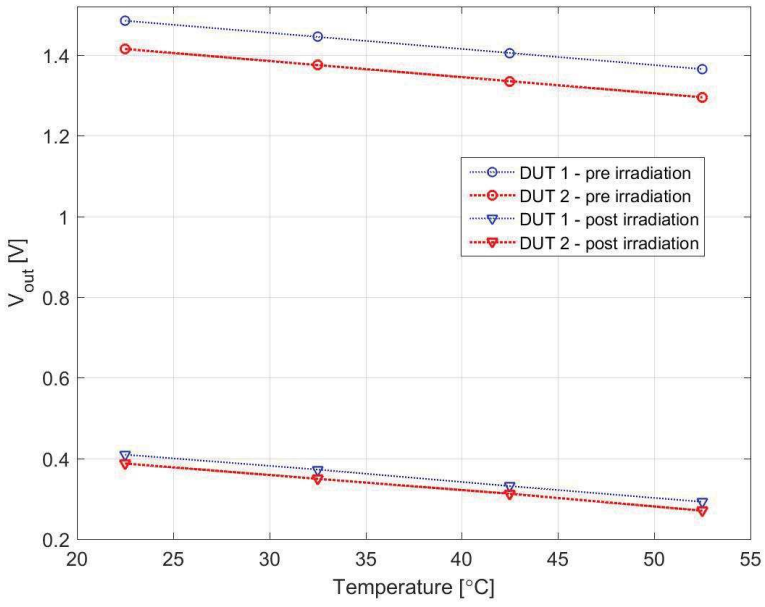

Figure 30. Output voltage as a function of the temperature

2.5 Conclusions

In this chapter, the radiation response of the 100nm RADFET and the NMOS DMN601 transistor has been discussed, aiming at addressing the suitability of the commercial device as ionizing radiation dosimeter for applications in the CERN environment. The investigation has been performed by employing the same reading system currently in suse to read the RADFET, i.e. the RadMon system.

The radiation response of the 100nm RADFET biased at 0V and 5V has been analysed. The calibration curve for both the biasing configuration, and the influence of the sensitivity degradation on the dose resolution has been discussed.

The NMOS DMN601 transistor has been characterized by exposing the sensor to gamma field at the CC60 facility at CERN. The sensitivity and resolution variation as a function of the dose has been discussed, as well as the error introduced by the sample-to-sample and batch-to-batch variation. Due to the lower initial voltage of the sensors belonging to the new batch, the measurable dose range needs to be limited to 550 Gy. In this range, the error on the measured dose is within the ±4%.

In Table 1, the characteristic of the RADFET and the NMOS are compared. As can be seen, the quality of the measurement performed by the NMOS transistor is comparable with the RADFET in terms of dose resolution, although the RADFET dose range is 4 times larger. However, the limited dose range of the NMOS does not depends on the radiation response of the sensor itself, but on the reading system employed.

TABLE I
MOS DOSIMETERS COMPARISON

Sensor	Bias	Sensitivity [mV/Gy]	Resolution [mGy]	Dose Range [kGy]	Error [%]
RadFET	0V	2.1	212	4.3	±8
	5V	7.9	57	2.3	±8
NMOS	0V	5.3	90	0.55	±4

Table 1. Summary of the characteristics of the MOS dosimeters analysed in this chapter. The error includes the sample-to-sample and the batch to batch variability for the NMOS sensor, whereas for the RadFET sensor it includes other terms of uncertainty such as temperature variation and different radiation sources (protons and gamma rays) [36].

The influence of the temperature on the NMOS has been investigated and a temperature sensitivity of -4 mV/°C has been measured, which is essentially constant over the dose. Hence, in order to perform accurate measurements, the temperature effect requires adequate corrective actions to compensate the output fluctuations induced by the changes in the temperature. For this purpose, the temperature must be measured and, through the temperature sensitivity, the output variation must be compensated for. This operation can be performed by means of the temperature sensor mounted on the deported module of the RadMon system.

Chapter 3 Total Ionizing Dose Sensors Based on Floating Gate Structure

In the past, several research groups have investigated the possibility to build a dosimeter based on a floating gate transistor. The first study on this concept was presented in 1991 by Kassabov at al. [38]. Although the layout of the device considered and the fabrication process are nowadays overcome [39], the results pointed out the intrinsic high linearity and high sensitivity to ionizing radiation, as confirmed by all the following investigations performed by different groups. The idea behind this dosimeter is to quantify the dose by measuring the variation of charge stored in the floating gate, which is induced by the dose itself. This mechanism can be exploited in different ways, such as by evaluating the charge variation of millions of floating gate cells embedded in commercial memories, as suggested in [40]–[43]. In these works, different approaches to determine the charge variation have been investigated, such as the counting of the switched cells in UVPROM memories or by measuring the time of UV exposure needed to fully erase the full memory. (A complete review of radiation effects in flash memories (i.e. devices based on floating gate transistor) can be found in [44]). It is possible to take advantage of the same principle by employing a single standalone floating gate transistor, whose layout can be designed to maximize the sensitivity: this approach has been proposed by several studies ([45]–[51]). This radiation sensitive structure is generally integrated on a more complex circuit, which provides several features to make its use simple, such as signal conditioning and temperature compensation circuits.

In this chapter, the study of a dosimeter designed by IC-Malaga, whose radiation sensitive circuit is based on a single standalone floating gate structure, will be presented. This radiation detector is named Floating Gate DOSimeter, shortly FGDOS. The working principle of the sensor will be discussed and the main parameters that affect the radiation response will be pointed out. In Section 3.2, the structure of the ASIC will be shown, and the different functional blocks explained. The characterization of the dosimeter under radiation will be deeply discussed in Section 3.3. Exposures to γ-rays were carried out to study the sensitivity and the linearity of the radiation response and to evaluate the influence of the dose rate. Several experiments were also performed to characterize the

dosimeter in terms of batch-to-batch variation. The effect of the temperature on the output signal has been characterized and a compensation method has been developed and implemented.

Finally, the characterization of the three different operational mode will be presented. As it will be shown, the FGDOS is a flexible system that can be configured in several ways, depending on the measurement requirements, such as the dose range, the dose resolution, the possibility of communicating with the sensor, etc. Indeed, the monitoring of the ionizing radiation is a crucial task for a wide range of applications, which is often tackled by developing tailored radiation monitoring systems. In the framework of monitoring the radiation levels of large and distributed infrastructures, such as particle accelerators or nuclear power plants, the measurement systems are permanently installed to facilitate the comparison of the dose values in time and space. In this context, a flexible system that allows the repositioning of the dosimeters to investigate unexplored areas, with easy access to the data and avoiding the design and installation of a cabled network would provide a large benefit.

The need of non-cabled radiation monitoring systems arises also when a highly accurate radiation field characterization is required, as it is the case for spallation sources or mixed field radiation facilities [52]. In particular, measurements on large surfaces or complex volumes require the mapping of the radiation field. In this context, the determination of the dose distribution on the device under test might not be straightforward, depending on the complexity of the device itself and the non-homogeneity of the radiation field.

The operational mode that allows to obtain the best performance in terms of dose resolution, accuracy and dose range is the Active Mode. As a drawback, the detector requires an intelligent system to control the recharge process and provide a high voltage to recharge the floating gate capacitor. In addition, the output signal acquisition must be performed online.

The Passive Mode permits to evaluate the dose by positioning the dosimeters where the radiation has to be measured: the output reading is performed before and after the irradiation and the sensors do not need any connection or supply during the radiation detection. As it will be shown, the dose range will be limited to the single discharge of the floating gate capacitor. To overcome this drawback, it is possible to use the sensor in Autonomous Mode, which allows the extension of the dose range up to the TID-lifetime of the sensor, i.e. the maximum dose that the sensor can afford. Thanks to the integration of the recharge circuitry on the FGDOS and the improvement of the communication controller, this functionality enables the sensor to provide the measurement of the data

every time the sensor is interrogated, according to the measurement needs. The digital interface allows the communication with a microcontroller meant for reading the data and configuring the sensor.

In this way, it would be possible to develop flexible monitoring systems, for example by implementing a network of detectors by reading each sensor through commercial wireless board capable of communicating by Serial Peripheral Interface (shortly SPI).

3.1 Working Principle

The radiation sensitive circuit allows measurement of the dose through the collection of negative charge generated by ionizing radiation in silicon dioxide. The simplest structure that can be conceived to implement this operation consists of a Metal-Oxide-Semiconductor (MOS) capacitor, whose metal plate is floating and positively charged before irradiation. The electric field in the silicon dioxide is given by two contributions: the difference between the metal and the silicon work functions, and the potential given by the charge stored in the metal plate. The electron-holes pairs surviving the first recombination are separated by the electric field, which pushes the electrons towards the metal plate and the holes towards the substrate. Ideally, the holes are entirely swept out of the insulator layer and pushed towards ground, where their net charge is totally neutralized. On the other side, the electrons are pushed towards the previously charged metal plate, whose net charge decreases by the number of carriers collected. The relationship between the ionizing radiation and the charge variation of the metal plate allows the measurement of the dose. The reading of the charge variation must be performed without altering the charge stored on the capacitor's plate. For this purpose, it is possible to measure the voltage variation on the capacitor by connecting the capacitor's plate to the gate of a transistor, whose current is directly modulated by the charge variation, and therefore by the dose absorbed. To avoid any charge redestribution that might affect the reading of the capacitor charge induced by switched commutation, the transistor and the capacitor's plate are permanently connected. In Figure 31, the discharge of the previously charged MOS capacitor and the reading circuit are represented.

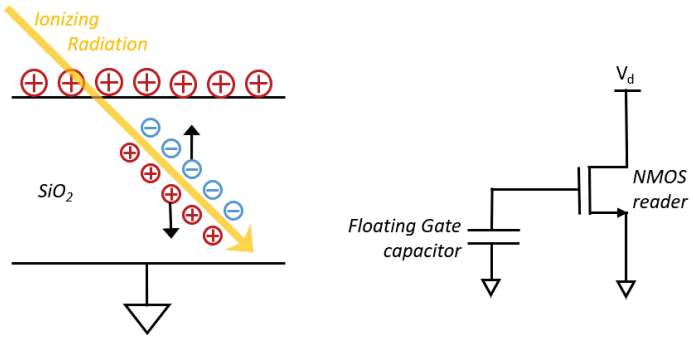

Figure 31. On the left the pre-charged Metal-Oxide-Semiconductor capacitor. The electron-hole pairs generated by the ionizing radiation are separated by the electric field. On the right, the circuit used to read the charge variation. The NMOS transistor does not alter the amount of charge stored in the capacitor.

It is worth to notice that, as a first approximation, the quantity measured by means of this structure corresponds to the charge yield, i.e. the amount of charge escaping the initial recombination. In fact, since the free electrons in the SiO_2 have a high mobility (20 cm2/V·sec) [23], it is reasonable to assume that all the electrons escaping the recombination reach the charged plate in picoseconds [53], [54]. On the other hand, the working principle of RADFETs and NMOS dosimeters is different, since in this kind of structures the quantity measured to obtain the dose, i.e. the shift of the Vth, is induced by the collection of positive charge in the silicon dioxide and at the Si/SiO2 interface. As explained in Section 2.1, the positive charge surviving the initial recombination induces the voltage shift only when they are trapped. In addition, the effectiveness of the single trapped charge depends on the charge position in the dioxide. The hole trapping efficiency is strictly related with the fabrication process, and can consistently change depending on the quality of the dioxide [25]. Radiation-hardened and unhardened devices can lead to a trapping efficiency of 1% and 99%, respectively. This qualitative analysis leads to conclude that the radiation sensitivity, intended as the derivative of the voltage on the MOS capacitor (either for the NMOS, RADFET and FG dosimeters) with respect to the dose, is higher for floating gate dosimeters than MOS dosimeters.

To have a quantitative model to describe the FG dosimeter working principle, some assumptions and considerations must be made. Firstly, the charge generated in the silicon dioxide can be obtained by the formula:

$$Q_{gen} = \frac{q \times E_{dep}}{W_{e-h}}$$

Equation 3.1

where q is the elementary charge, E_{dep} is the energy deposited by ionizing radiation and $W_{e\text{-}h}$ is the energy necessary to generate a single electron-hole pair. To highlight the dependence between the voltage variation and the dose, it is convenient to consider the deposited energy as follows:

$$E_{dep} = m \times D = \rho_{SiO_2} \times A \times t_{ox} \times D$$

Equation 3.2

where D is the dose and m is the mass, which can be expressed as the product of the dioxide density ρ_{SiO2} with the volume, i.e. the area A times the thickness t_{ox}. Assuming that (i) the all the electrons that survive the initial recombination reach the plate, (ii) no positive charge is trapped in the silicon dioxide or at the Si/SiO2 interface, the collected charge will be proportional to the generated charge, through the recombination rate R:

$$Q_{col} = Q_{gen} \times \big(1 - R(\mathcal{E})\big)$$

Equation 3.3

in which Ɛ indicates the electric field, which affects the charge yield by reducing the probability of recombination [55]. The second factor in Equation 3.3 represents the charge yield factor, i.e. the percentage of electron-hole pairs surviving the first recombination. Once the charge variation on the metal plate has been determined (i.e. the charge has been collected), it is straightforward to calculate the voltage variation on the capacitor as a function of the dose, through the capacitor relationship:

$$\Delta V = \frac{\Delta Q_{col}}{C}$$

Equation 3.4

where C is the capacitance of the capacitor, which can be expressed as:

$$C = \frac{\varepsilon \times A}{t_{ox}}$$

Equation 3.5.

In the previous equation, ε is the permittivity of the dielectric, given by the product between the relative permittivity of the material ε_r and the permittivity of the free space ε_0, and the other terms have been already introduced. Combining the above-reported equations it is possible to express the voltage variation as a function of the dose:

$$\Delta V = \frac{q \times \left(1 - R(\mathcal{E})\right) \times \rho_{SiO_2} \times t_{ox}^2}{\varepsilon \times W_{e-h}} \times D$$

Equation 3.6.

The relationship between the dose and the voltage variation expressed by Equation 3.6 shows a direct proportionality between the two variables. Nevertheless, the function is not completely explicit, as the charge yield depends on the electric field, which is, in turn, a function of the voltage variation. In Figure 32, the fraction of carriers surviving the recombination is plotted against the electric field for different particles (from [37]). Considering that the electric field in the insulator layer can be calculated as the ratio between the voltage on the capacitor (i.e. the difference between the initial voltage and the voltage variation) and the oxide thickness, it can be expressed as:

$$\mathcal{E} = \frac{V_{cap}}{t_{ox}} = \frac{V_{init} - \Delta V}{t_{ox}}$$

Equation 3.7

To make the relationship completely explicit, it would be necessary to know the analytic expression of the charge yield. The dependency of the charge yield on the electric field has been discussed in several studies (e.g. [25], [37], [55]–[58]), although no particular attention was paid to electric fields lower than 1 MeV/cm. Some mismatch can be found among these works for these electric fields. (This range is particularly interesting for the floating gate dosimeter here investigated, as the drop on the capacitor is ~70 keV/cm.) The curve relevant to the charge yield generated by ^{60}Co reported in Figure 9 shows a charge yield of about 0.3 for a null electric field. On the contrary, in more recent studies Schwank at al. [37] show that the charge yield is zero for null electric field. This means that for small electric fields, the charge yield can be approximated by a straight line crossing the axis origin (see Figure 32). This means that if no electric field drops on the insulator layer, then all the generated electron-hole pairs recombine with each other. On the other hand, the same curve reported in other works (e.g. [19], [25], [57]) does not cross the axis origin, meaning that a certain amount of charge escapes the recombination even though no electric field is applied.

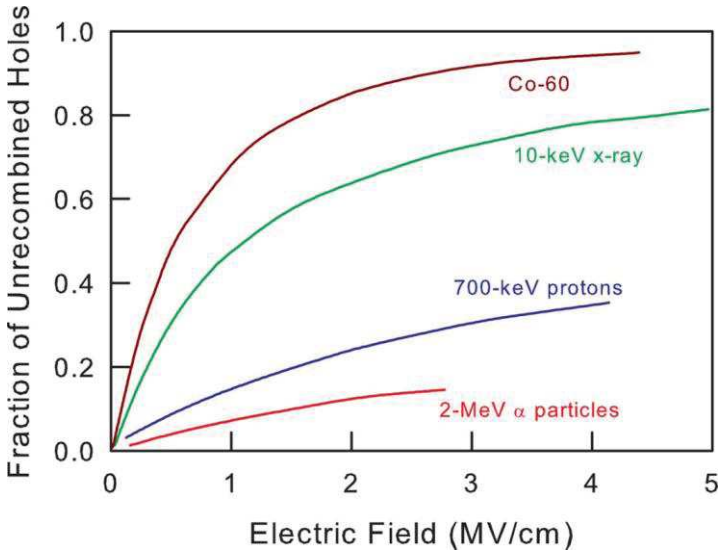

Figure 32. Charge Yield as a function of the electric field. (Source: [53]).

This phenomenon has been deeply investigated by Oldham and McGarrity in [58], where the charge yield is plotted on a logarithmic scale to magnify the spread among devices with different oxide thickness at low field (see Figure 33). As can be observed, the thicker the oxide, the lower the charge yield, being equal the applied field. This effect is caused by the difference between the metal and the silicon work functions of the MOS sandwich: being the devices built with the same materials, all of them have the same built-in potential over their insulator layer, and, consequently, the built-in electric field results lower for thicker oxides. Therefore, Figure 32 is consistent with this reasoning as the x-axis of the plot represents the net electric field in the insulator layer, given by both the applied and the built-in electric field.

The maximum charge that can be stored in the capacitor is limited by the technology, as the highest electric field that can be sustained by the gate oxides depends on the fabrication process. Hence, the amount of radiation sufficient to fully discharge the capacitor is limited as well: the resulting measurable dose range would not make this structure suitable for dosimetry purpose. To overcome this limitation, the charge must be restored every time the voltage on the capacitor drops below a certain threshold (whose role and choice will be clarified later in this chapter). This operation can be performed by using a p-channel MOS transistor whose gate is connected to the floating gate capacitor, whereas drain and source are shorted and connected to a switch that controls the access to a high voltage: when the switch is closed, the high voltage drops on the gate oxide of the pmos transistor, enabling a tunnelling current that recharges the capacitor. In this way, the amount of charge stored in the floating gate capacitor is perturbated exclusively during the injection. Being the capacitance of the injector much smaller than the capacitance of the floating gate capacitor, most of the high voltage

applied to the injector drops on the injector itself, whereas the potential of the FG capacitor does not change significantly: such an unbalanced voltage divider allows the measurement of contribution on the voltage exclusively due to the stored charge during the recharge phase, neglecting the contribution due to the high voltage coupling. This feature is extremely important to precisely control the amount of charge injected during the recharge. The tunnelling current is a quantum mechanics phenomenon that occurs when the high voltage drop on the thin oxide layer bends the energy levels of the insulator enough to make the probability for a carrier to cross the layer not negligible, even though the carrier has not enough kinetic energy to overcome the energy gap [59]. The same mechanism is exploited to program EEPROM memories [60].

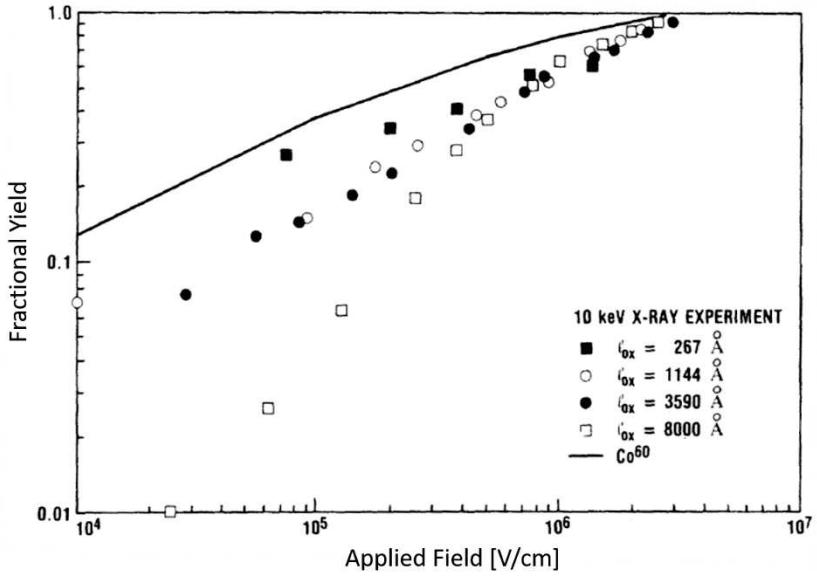

Figure 33. Charge Yield as a function of the electric field (for low electric field).

The recharge technique discussed above allows multiple discharges of the capacitor, considerably extending its measurable dose range. As it will be discussed in this chapter, the discharge can be iterated as long as some of the functional blocks of the ASIC are compromised by the radiation. Moreover, a fine control of the recharge process allows to exploit a limited portion of the discharge of the capacitor in such a way as to ensure a linear relationship between the absorbed dose and the output of the reading system. In fact, as shown by Equation 3.6, the voltage variation is not linear with the absorbed dose since the sensitivity of this structure depends on the electric field, which is a function of the voltage drop on the capacitor. Moreover, the voltage variation is read by a NMOS transistor (see Figure 31), whose I_d-V_{gs} characteristic can be considered linear only for small voltage variations. Constraining the capacitor discharge within a small range would allow to have a linear response between the dose and the current of the reading transistor. To ensure that the dose measurement is

not affected by the recharge process, two conditions should be met: (i) the recharge amplitude should be equal at each recharge, and (ii) the recharge time should be negligible (ideally instantaneous) with respect to the discharge time. The recharge amplitude corresponds to the working range of the sensor, whose lower and upper limits are named *threshold* and *target*, respectively. It is worth noticing that these limits can be defined in terms of charge stored in the capacitor, voltage at the floating gate, current in the channel of the reading transistor, or output of the signal conditioning circuit of the ASIC. In Figure 34, the implementation of the recharge process is represented. On the y-axis, the output has not been specified as the signal represented can refer to the charge stored in the capacitor, the floating gate voltage, the drain current or the output of the signal conditioning. Finally, the compensation of the jumps due to the recharges allows to achieve a linear radiation response.

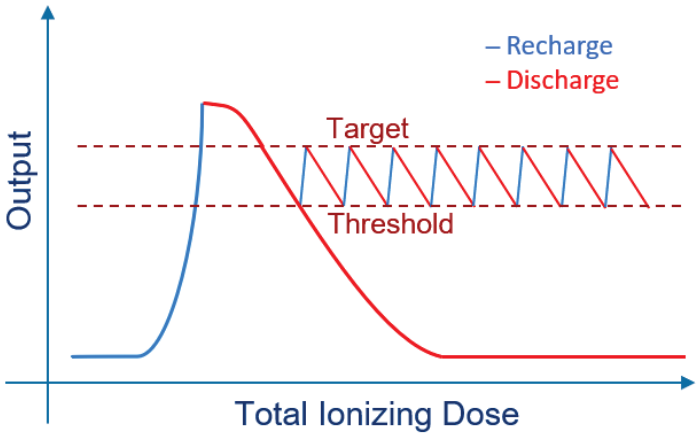

Figure 34. Linearization of the characteristic by means of the recharge process.

The development of the physics model here discussed has been carried out by assuming that the charge collection mechanism is not affected by hole trapping in the silicon dioxide. However, this hypothesis works as a first approximation, since the amount of trapped charge is negligible with respect to the electrons collected at the positively pre-charged plate of the capacitor. As mentioned before, this happens because the trapping probability for the holes pushed towards the substrate by the electric field is much lower than the collection efficiency for the electrons at the capacitor plate. Nevertheless, being the hole trapping a cumulative effect, the increase of positive charges distributed in the silicon oxide affects the sensitivity of the sensor.

Indeed, depending on the trapped charge position, the resulting electric field changes, influencing the recombination rate. To understand the role of the positioning of the charge in the insulator layer, it is helpful to imagine a sheet of charges located at distance x_d from the substrate-insulator interface, which is taken as origin of the reference system considered in Figure 35. The resulting field is given

by the superposition of the fields generated by (a) the charge stored in the floating gate plate and (b) the charge trapped in the insulator layer. The electric field generated by the positive charge stored on the capacitor plate is depicted in Figure 35-(a), whereas the one generated by the trapped charge layer is depicted in Figure 35-(b). The net electric field is given by the vectorial sum of the two contributions. The magnitude of the resulting field between the substrate-insulator interface and the trapped charge layer (i.e. for $0 < x < x_d$) will be higher, as the two fields have the same direction. On the other hand, in the region between the trapped charge layer and the floating gate plate (i.e. for $x_d < x < t_{ox}$), the resulting electric field will be weaker, as the two contributions have opposite direction. Therefore, the trapped charge layer increases the electric field between the charge layer and the interface, leading to a lower recombination rate. On the contrary, the electric field will be lower between the charge layer and the floating gate, resulting in a higher recombination rate. However, it is reasonable to assume that the distribution of trapped holes will be significantly higher near the interface than towards the floating gate for two reasons: (i) the trap density is higher close to the silicon dioxide [18], and (ii) the holes are forced to travel towards the substrate by the electric field: the probability for a hole to be trapped between its generation point and the floating gate is null. This qualitative analysis leads to conclude that the accumulation of positive charge in the silicon dioxide will affect the sensitivity of dosimeters based on this structure: this topic will be discussed in Chapter 4.

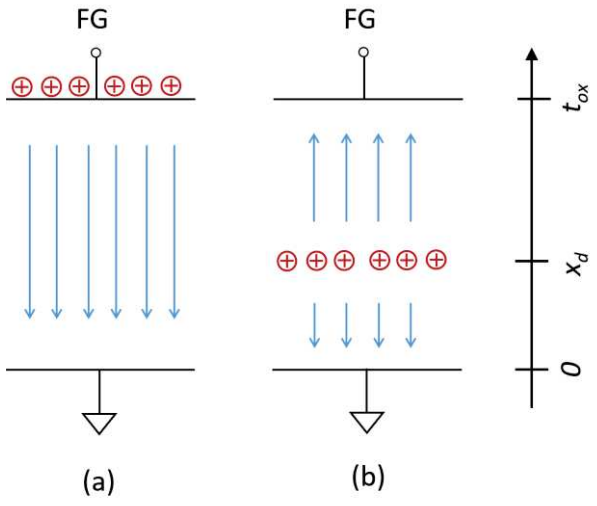

Figure 35. Effect of the positive trapped charge on the electric field. On the left (a) the electric field due to the positive pre-charge floating gate. On the right (b), the contribution due to the trapped hole layer.

3.2 FGDOS Structure

The FGDOS is a System on Chip (SOC) that can be described by the block diagram in Figure 36, where each block corresponds to a specific function integrated on the ASIC. The dosimeter is based on the structure discussed in Section 3.1: a floating gate transistor that can be modelled as a capacitor connected to the gate of a reading transistor, whose drain current is a function of the voltage variation on the capacitor and, therefore, to the absorbed dose: the floating gate transistor is the *radiation sensitive circuit* of the dosimeter. The drain current of the transistor is converted into a square wave signal, whose frequency is proportional to the current.

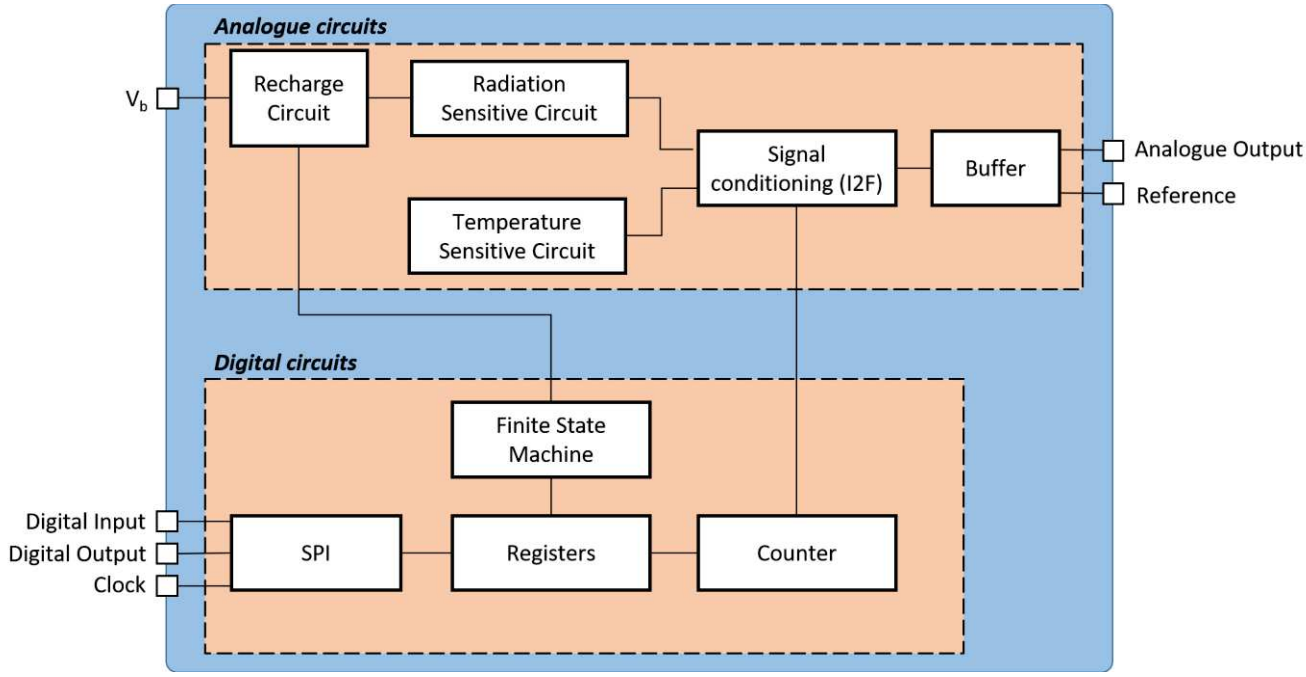

Figure 36. Block diagram of the FGDOS core sensor.

The *signal conditioning* allows the shaping of the signal in both analogue and digital form. The analogue signal is generated by the *buffer*, which produces a 0-5 V square wave that can be driven on loads such as PCB paths or 10 metres coaxial cable. In this case, the frequency variation needs to be computed out of the chip, e.g. through an FPGA. For this purpose, a board has been developed [61]. The digital form of the signal is provided by a counter, which evaluates the pulses in a specific time window and writes the value into a dedicated register. The reading of the frequency is performed by accessing to the registers through SPI by means of a microcontroller. In the same way, the communication with the FGDOS allows to set different configurations of the *finite state machine*, including, among other features, the control of the recharge process either by the internal *recharge circuit* or by enabling the high voltage V_b provided externally. The internal *recharge circuit* must provide a high

voltage (~18 V) to the injector of the *radiation sensitive circuit* in order to enable the tunnelling current to recharge the capacitor. Moreover, two configurations can be set to get different sensitivities, hereafter named High Sensitivity (HS) and Low Sensitivity (LS) configuration. Finally, to compensate for the effect of the temperature, a dedicated *temperature sensitive circuit* is embedded in the ASIC: its functioning will be presented in Section 3.2.1.

Such an articulated structure allows the measurement of the dose in different ways, depending on which features integrated on the FGDOS are exploited and taking advantage of the intelligence embedded in the ASIC. Accordingly, three different operational modes can be distinguished: Active Mode, Autonomous Mode and Passive Mode. The monitoring of the output signal characterizes each operational mode: the online monitoring and recording of the signal is required for the Active Mode, whereas for the Passive Mode the output reading must be performed before and after the irradiation. The Autonomous Mode allows to obtain the dose information without recording the frequency signal, giving the opportunity to perform the measurement whenever it is intended, by simply communicating with the FGDOS. Moreover, each mode can be exploited in different ways depending on:

- the communication with the sensor, which can be performed by an FPGA or a microcontroller through SPI;
- the counting of the pulses within a specific time window for the calculation of the output and reference frequency, which can be performed by the internal counter or externally, e.g. by the FPGA;
- the control of the recharge process, which can be performed by the FGDOS or externally, e.g. by the FPGA;
- the voltage to be applied to the injector for the recharging, which can be generated by the internal charge pump or provided externally.

In Figure 37, all the possible configurations of the FGDOS are reported. The operational modes (Active, Autonomous and Passive) can work in High or Low sensitivity configuration.

Being the FGDOS a complex integrated system that is required to work in harsh radiation environments, the whole chip will be somehow affected by ionizing radiation. In this concern, the degradation of the performance of the sensor must be carefully evaluated in order to prevent errors in the measurement. As it will be shown Chapter 4, the most significant effect of ionizing radiation on the operation of the sensor is related to the decrease of the sensitivity of the *radiation sensitive circuit*.

The mechanisms behind this phenomenon have been deeply investigated by performing dedicated experiments on test chips designed and fabricated on purpose. Moreover, the decrease of the sensitivity has been characterized to compensate the error in the measurement, as it will be shown in Section 3.6.2.

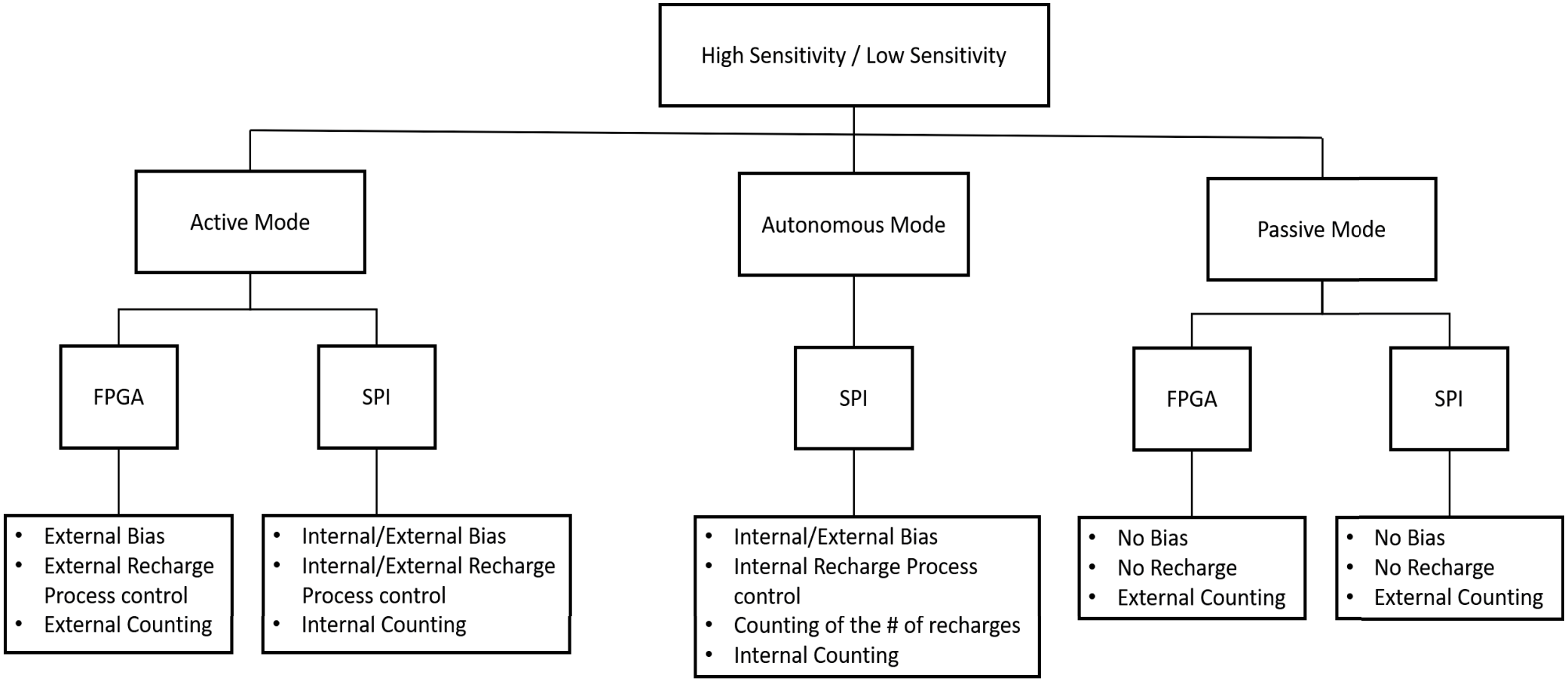

Figure 37. FGDOS operational configurations.

3.2.1 Radiation Sensitive and Temperature Sensitive Circuit

The radiation sensitive circuit of the FGDOS consists of a floating gate transistor, whose area is over-extended on the field oxide layer that acts as insulator placed between the gate and the bulk. This structure can be seen as a large capacitor, whose charge is read through the current flowing in the channel of the reading transistor. To restore the charge neutralized by the radiation, a PMOS injector is connected to the capacitor. In Figure 38, the layout of the core sensor, including the NMOS reader and the PMOS injector, is shown. The resulting radiation sensitive volume of the sensor corresponds to the field oxide that is covered by the floating gate [62].

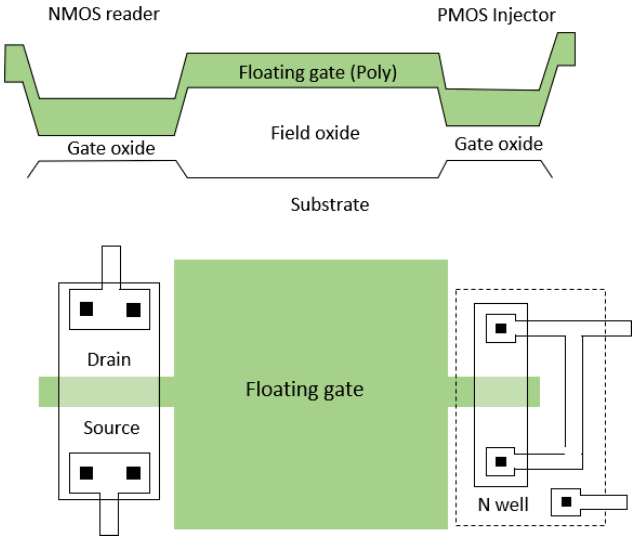

Figure 38. Layout of the Radiation Sensitive Circuit of the FGDOS.

The *radiation sensitive circuit* and the *temperature sensitive circuit* are depicted in Figure 39. As mentioned in Section 3.1, the capacitor is charged before the irradiation via the PMOS injector. The ionizing radiation measurement is performed by reading the current variation of the NMOS transistor, which is modulated by the voltage drop on the pre-charged capacitor. The charge generated by the separation of the electron-hole pairs in the tunnel oxide, partially neutralizes the charge pre-stored in the capacitor, leading to the reduction of the voltage. Consequently, the change in the gate-source potential of the NMOS transistor changes the current flowing in the channel.

The influence of the temperature on the current of the MOS transistor is known since many decades [63]. Not surprisingly, the drain current is influenced by the effect of the temperature on system floating gate capacitor/reading NMOS. For this reason, the compensation of the temperature effect is necessary. To cancel it, the idea is to generate a signal that has a similar temperature response, but is not affected by radiation. For this purpose, a twin NMOS transistor with the same size and geometry

of the reading transistor of the radiation sensitive circuit has been integrated in the chip. The current signal generated by this structure is converted in a frequency signal by the same signal conditioning circuit used for the radiation sensitive circuit and called *reference*, shortly F_{ref}. In order to have a temperature response as close as possible to the one of the radiation sensitive circuit, the reference NMOS is biased like the NMOS reader of the floating gate capacitor while it works within the range limited by the target and the threshold. Ideally, the signal cleaned from the temperature influence can be obtained by subtracting the signal generated by the temperature sensitive circuit, i.e. reference frequency F_{ref}, from the signal generated by the radiation sensitive circuit, i.e. F_{sens} , as suggested in [64]. However, this assumption makes the temperature compensation inaccurate: a different method will be proposed in Section 3.4.3.

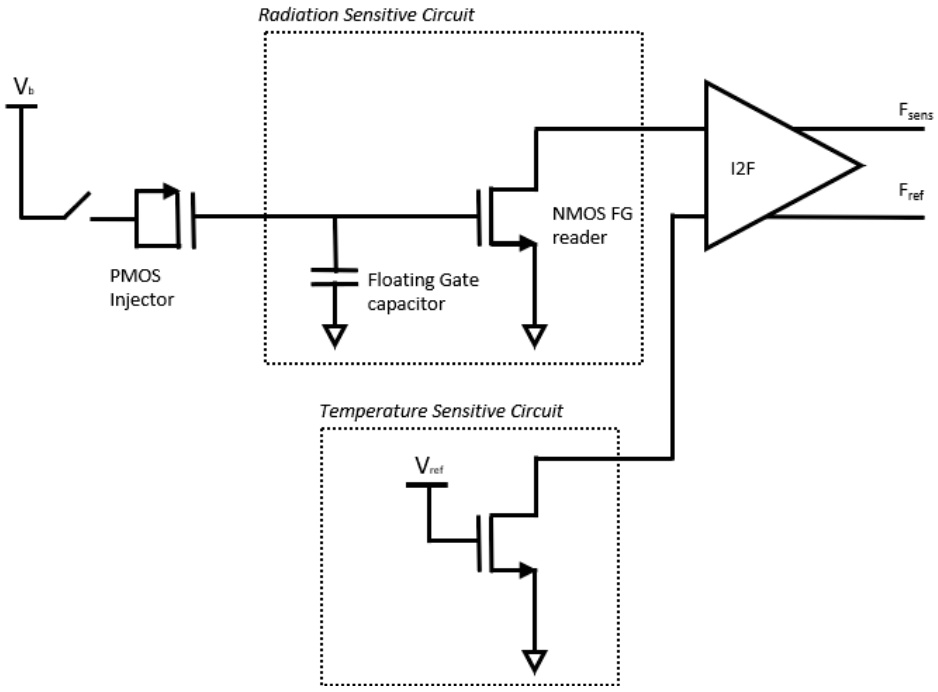

Figure 39. Block diagram of the FGDOS core sensor. The Floating Gate transistor is modelled by the Floating Gate capacitor and the NMOS transistor reader. The charge is injected in the Floating Gate through the PMOS injector.

Figure 39 shows the main elements of the core circuit of the FGDOS, although the schematic is not complete for the sake of clarity. For instance, the circuit used to change the High and Low Sensitivity of the sensor is not shown. These sensitivities are obtained by switching between two reading transistors, whose dimensions determine different transconductances, leading to different voltage to current gain.

3.2.2 Recharge Process and Linear Range

As anticipated in Section 3.1, since the *Radiation Sensitive Circuit* is intrinsically non-linear, the sensor is employed by exploiting a limited portion of its characteristic. In this way, the output variation is proportional to the absorbed dose. To force the sensor working in this limited range, the floating gate capacitor must be recharged up to a *target* value whenever the radiation discharges it below a certain *threshold*. The target and the threshold values limit the linear range in terms of both charge stored in the capacitor and output frequency. In Figure 40, the functioning of the recharge process is illustrated, where the radiation response of the sensor with and without the recharge process enabled are compared. The full discharge of the capacitor is represented by the red curve: during the irradiation, the recharge process was disabled, allowing to obtain the whole dynamic range of the sensor. The sawtooth wave signal represented by the blue curve is the output of the sensor while the recharge process was enabled: as can be noticed, the output frequency varies between two values, corresponding to the target and the frequency (depicted by the dashed black lines in the picture). The linearized output signal, which is obtained by compensating the jumps due to the recharges, is represented by the green curve. The resulting radiation response is practically a straight line. (The solidity of this statement depends on the operational configuration employed, as it will be discussed in this chapter.) Once the signal has been linearized, the dose can be easily retrieved by dividing the frequency variation by the sensitivity.

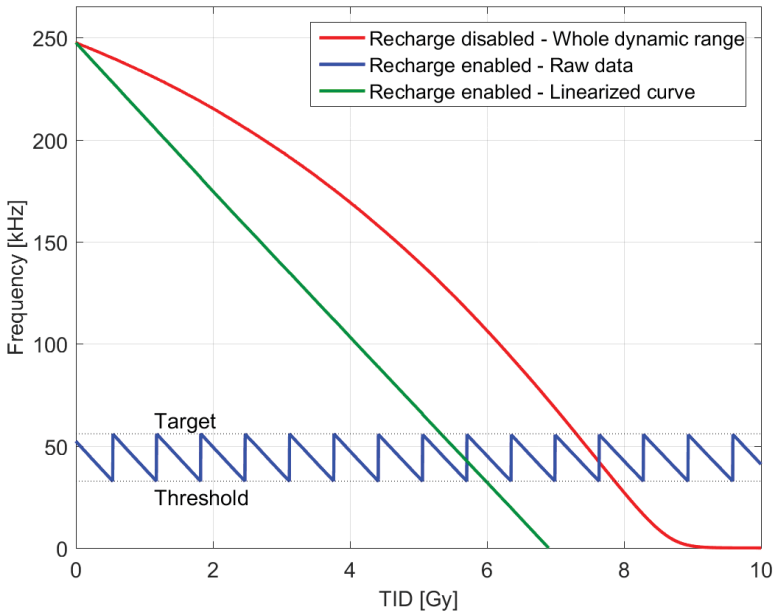

Figure 40. Linearization of the sensor response. The red curve represents the full characteristic of the FGDOS, whereas the blue curve shows the response obtained by limiting the working point in the linear region by means of the charge injection. In green, the radiation response obtained by compensating the jumps due to the recharge.

To properly recharge the capacitor, a system to control the recharge process must be implemented. The recharge control is responsible for comparing the output signal with the threshold value and apply the high voltage V_b to the injector for enabling the recharge of the floating gate capacitor. The high voltage must be disabled as soon as the output reaches the target frequency. The recharge process control can be implemented externally (i.e. by an FPGA), or internally, as the *Finite State Machine* of the FGDOS has the capability to control the recharge. In this latter case, the threshold and the target frequency can be set by writing them in the registers of the sensor. Moreover, the number of recharges is stored in the registers: this feature characterizes the Autonomous Mode and allows the calculation of the absorbed dose by knowing the number of recharges and the frequency at the reading. If the control is performed by the FPGA, the frequency limits must be managed externally.

3.3 Radiation Response Characterization

In order to use the FGDOS as dosimeter, its radiation response has been fully characterized from several points of view, evaluating the calibration parameters necessary to carry out the measurement and assessing its suitability for the radiation environment produced by the particle accelerator. For this aim, several irradiation tests were performed at the CC60 facility at CERN, where a homogenous gamma field is generated by a ^{60}Co source. The response curve of sensors belonging to different batches has been compared to understand if the calibration of each batch must be performed prior to their use. This is important for large distributed systems like the LHC, where hundreds of sensors can be installed and could potentially not belong to the same lot. In addition, the spread among the responses of sensors belonging to the same batch has been evaluated to verify if the fabrication process influences the radiation response. Irradiations with different dose rates were performed to evaluate the dose rate effect on the response. This is a necessary step to understand if this dosimeter is suitable for dose measurement in locations where the dose rates can be very different depending on the installation location, as is the case in the CERN accelerator complex [65].

For charge trapping dosimeters, such as RADFETs and NMOS, a calibration curve is necessary to compensate for their intrinsic non-linearity. To understand if this will also be an issue for the FGDOS, the linearity of the radiation response has been measured and discussed.

The temperature sensitivity has been investigated as it can play an important role in a very large facility such as the accelerator complex. Indeed, as discussed in Section 3.2.1, the output signal of the dosimeter is sensitive to temperature fluctuations and, for this reason, a temperature compensation

method different from the one proposed in [64] has been developed and implemented in order to improve the robustness to temperature variation.

The results of this characterization were presented at the Radces Conference held in Bremen (Germany) in September 2016, and published in the conference proceedings [50].

3.4 Active Mode

The aim of the device characterization was to delineate the behaviour of the sensor under radiation, in particular evaluating the performance of the *radiation sensitive circuit* or the FGDOS. For this reason, the experiments were performed by using the sensor in Active Mode, i.e. reading the output and the reference frequency through an FPGA, which was also in charge of the control of the recharge process. Moreover, to ensure fast recharges of the floating gate capacitor, the high voltage was provided externally. In this configuration, most of the secondary features embedded in the sensor, such as the control of the recharge process and the generation of the high voltage by means of the internal charge pump, are not exploited. The reading system used to control and read the FGDOS is called TIDMON (Total Ionizing Dose MONitor) and has been presented in [61]. This operational configuration can be easily identified in Figure 37, as it fits with the first branch on the left.

3.4.1 Batch-to-Batch and Dose Rate variation

The variability between batches and the effect of the dose rate have been investigated by irradiating two batches named *batch A* and *batch B*, made up of four FGDOS sensors each, at dose rates of 3.2 and 0.32 Gy/h, hereafter tagged as Low Dose Rate (LDR) and High Dose Rate (HDR), respectively, while the temperature was kept constant at 20°C. The radiation response, i.e. the output signal variation as a function of the dose, have been compared for the LDR and HDR experiments.

The spread among the radiation responses of the samples has been evaluated for each batch irradiated at HDR and LDR. The maximum difference among the sensors has been calculated with respect to the average of the radiation responses obtained by each sensor. The amplitude of the confidence interval of 95%, which is indicated as $\pm 1.96\sigma_{REL}$, has been computed considering a Student's t-distribution rather than a Gaussian distribution, because of the limited number of samples. Spread and confidence intervals for each run are reported in Table 2. The spread due to the sample-to-sample variation is within 3%, which leads to the same variation in terms of dose measurement, thanks to the linearity of the sensor (as will be shown in the following paragraph).

TABLE II
SUMMARY OF THE RADIATION RESPONSES

BATCH	DOSE RATE	SENSITIVITY [KHZ/GY]	±1.96σ [%]	MAX SPREAD W.R.T. THE AVERAGE [%]	DOSE [GY]
A	HDR	34.0	5.7	2.3	10
	LDR	31.7	6.3	2.7	5
B	HDR	29.6	7.9	2.9	20
	LDR	34.7	10.1	2.4	3

Table 2. Results of HDR and LDR irradiation runs for batches A and B. The spread among the curves is evaluated w.r.t. the average.

The behaviour of the two batches has been compared by irradiating the sensors in the same conditions. For each batch, the average of the four sensor curves has been considered. With the aim to understand the variation of the dose measurement performed by sensors belonging to different batches, the difference between the two average curves (batch A and B) has been evaluated and expressed as percentage of their mean value. This calculation has been done for both HDR and LDR irradiation, and the results are reported in the first two rows of Table 3.

TABLE III
IRRADIATION COMPARISON

		MAX SPREAD W.R.T. THE AVERAGE [%]	DOSE [GY]
Batch comparison	HDR	1.9	10.0
	LDR	3.7	3.0
Dose Rate comparison	Batch A	3.7	5.0
	Batch B	9.5	3.0

Table 3. Comparison of the runs performed by irradiating batches A and B at HDR and LDR. The percentage difference is evaluated w.r.t. the average of the response curves for the doses indicated in the last column.

To evaluate the potential influence of the dose rate, a comparison among runs performed at high and low dose rate both for batch A and B, is carried out. As it has been done for the batch comparison, the spread is expressed as percentage of the average. The results concerning the dose rate compari-

son are reported in the last two rows of Table 3. In Figure 41, the radiation response curves are compared up to 3.0 Gy. The average sensitivity weighted on the cumulated dose of each run is 31.4 kHz/Gy. The highest dose level reached during these experiments was 320 Gy, although FGDOS were irradiated with γ-rays and protons up to 280 and 200 Gy, respectively [49].

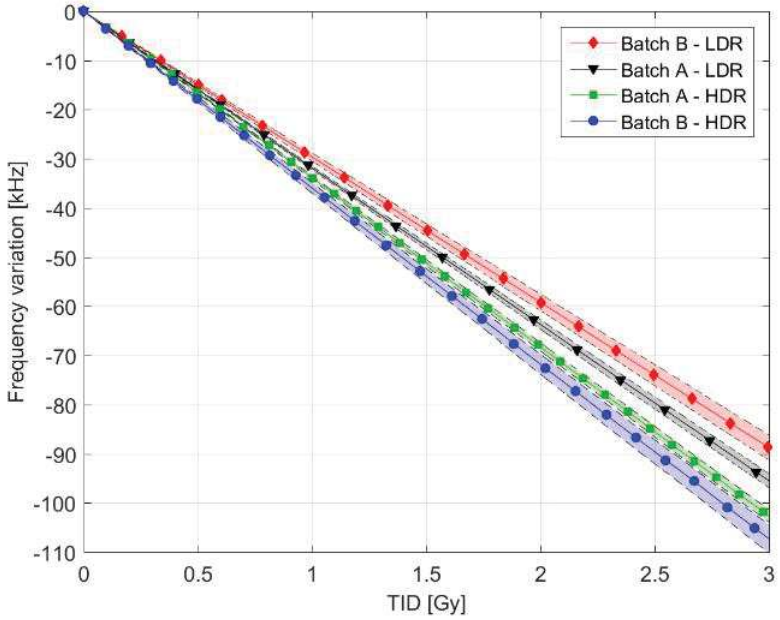

Figure 41. Frequency output as a function of TID for gamma ray exposure. The curves show the radiation responses of the batches A and B, irradiated with dose rates of 3.20 and 0.32 Gy/h, respectively indicated as HDR and LDR. The highlighted areas represent the confidence interval of 95%, considering a t-student distribution, while the solid curves show the average curve of each batch.

3.4.2 Resolution and Linearity

Considering both the noise of the sensor and the one introduced by the reading circuitry of the readout TIDMON board, the minimum frequency detectable is approximately within 5 Hz. The noise has been evaluated by removing the effect of the temperature on the output signal, i.e. by subtracting the filtered data to the raw data (see Figure 42). The dose resolution calculated as the ratio between the frequency noise and the sensitivity, is 160 µGy.

In order to obtain the linear radiation response, the jumps due to the recharge are compensated, obtaining the green curve already shown in Figure 40, which represents the frequency variation only due to dose. The whole dynamic range has been therefore achieved, as shown by the red curve again

in Figure 40. This process is implemented by the readout board and it will be hereafter named the auto-recharge process.

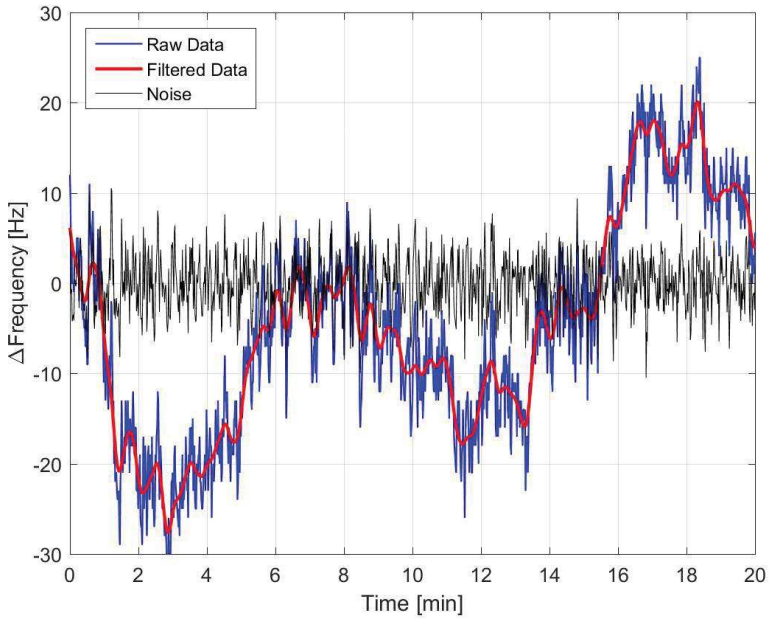

Figure 42. Noise on the output signal obtained by reading the FGDOS with the TIDMON. The raw data are represented in blue, while the red curve is the filtered signal.

In order to evaluate the linearity obtained with and without the recharge process, two sensors were irradiated at the same time with a dose rate of 2.8 Gy/h. The sensors were read by means of the TIDMON board, which controlled the recharge process and provided the high voltage during the irradiation (only of one of the sensors). The results of the experiment are plotted in Figure 40, which has been commented in Section 3.2.2 to explain the recharge process. Here, the blue curve represents the output of the sensor whose recharge process was controlled by the FPGA, while the green cure represents the same signal whose jumps due to the recharges were compensated. The red curve was obtained by recharging the sensor to the maximum frequency achievable (i.e. injecting the maximum amount of charge allowed on the floating gate), before the irradiation. For the sake of comparison, the compensated curve has been shifted to the starting point of the curve obtained by irradiating a sensor previously recharged.

The linearity has been evaluated considering the maximum distance between the curve achieved by irradiating the sensor and a linear fitting curve,which is defined as the straight line having its slope equal to the average sensitivity of the radiation response curve within the linear range. For convenience, it is expressed as a percentage of the linear fitting curve. In formula:

$$\Delta Freq_{rel}[\%] = 100 \times \frac{\left|Freq_{out} - Freq_{fit}\right|}{Freq_{fit}}$$

Equation 3.8

The linearity has been evaluated both for sensors forced to work in the linear range by the recharge process enabled and sensors charged to the maximum achievable frequency, which were irradiated until the floating gate was completely discharged. The recharge process allowed to achieve a very linear response, whose linearity resulted lower than 1.8% over a cumulated dose of 20 Gy. On the other hand, is the recharge process is disabled, the sensor can swing over its full range (depicted in red in Figure 40), with significant linearity degradation. Indeed, in this last case, considering a frequency swing from 247 to 0 kHz (corresponding to a cumulated dose of 9.60 Gy), the resulting linearity is 26%.

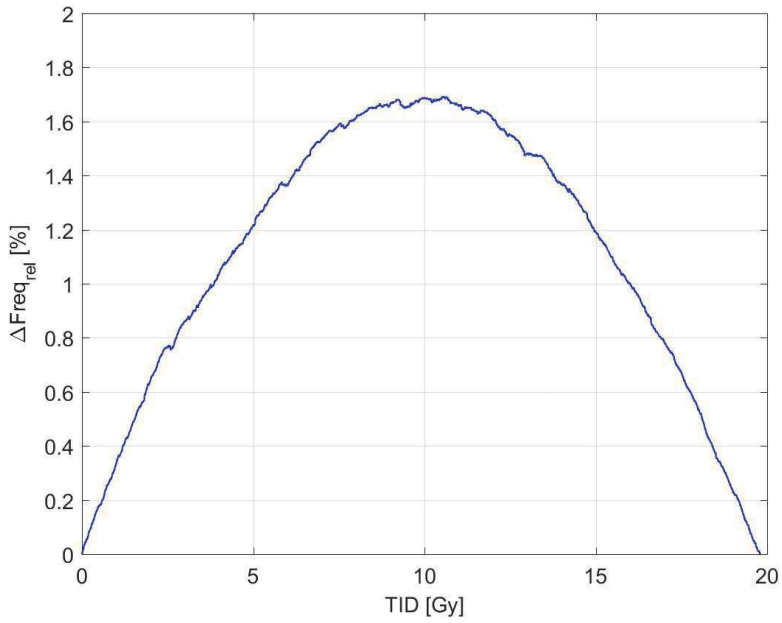

Figure 43. Relative frequency error for the signal obtained by compensating the jumps due to the recharge process (green curve in Figure 40).

3.4.3 Temperature Effect Compensation

As discussed in Sectio 3.2.1, the output signal of the FGDOS is influenced by temperature fluctuations and, for this reason, compensation is necessary. To implement the compensation, an NMOS transistor identical to the one reading the FG capacitor and biased in similar conditions, is integrated on the chip. The idea is to generate a signal which follows the temperature fluctuations exactly in the same way as the signal generated by the *radiation sensitive circuit*, but is instead immune to the ionizing

dose. The frequency signal given by the twin NMOS is taken as reference. Two conditions are essential to implement this method: (i) the a reference signal must not change with the dose, and (ii) the temperature sensitivity should be the same for both the *radiation* and *temperature sensitive circuits*. Dose independency of the reference signal has been evaluated for the irradiated batches: a variation smaller than 1% over a cumulated dose of 230 Gy has been measured. Therefore, if the temperature would influence the two circuits in the same way, it would be sufficient to considerer the output signal given by the difference of the two frequency outputs to remove the temperature effect. (This technique has been proposed in [64].) However, a significant disagreement between the response to temperature variation of the reference and the output frequency has been observed, which forces to find a different solution. This difference can be quantified by considering the temperature sensitivity S_t, which can be calculated as:

$$S_t = \frac{\partial Freq}{\partial T}$$

Equation 3.9

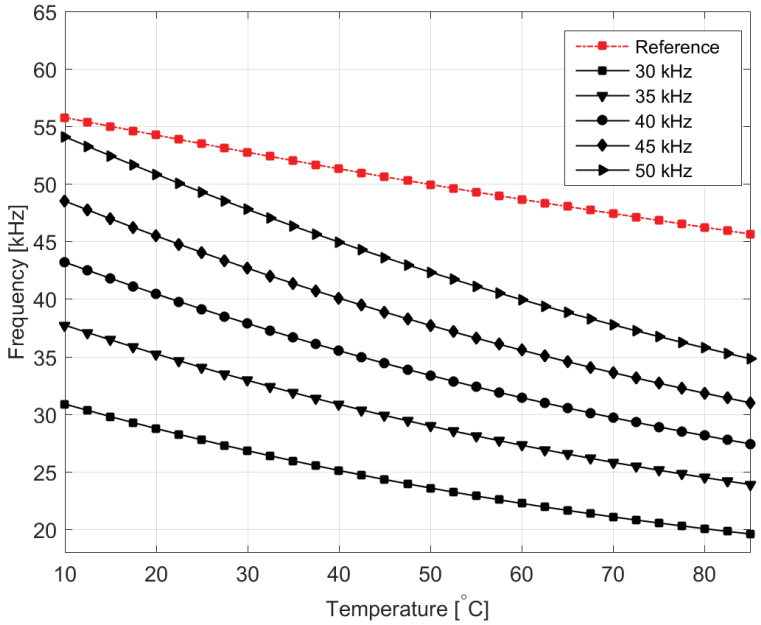

Figure 44. Frequency as a function of temperature. The uppermost curve shows the frequency variation of the twin MOSFET, i.e. the reference frequency. The lower curves show the frequency variation of the floating gate transistors for different amounts of charge stored in the floating gate. In the legend, the initial frequency at 20 °C is reported.

This behaviour has been characterized by performing several tests. Since the linear range for this version of the sensor spans from 30 to 50 kHz, the initial working point was set up by charging the sensor in order to get an output frequency of 30, 35, 40, 45 and 50 kHz¸ keeping the temperature constant at 20°C. On the other hand, the potential at the gate of the twin transistor is fixed to a value corresponding to a reference frequency of 55 kHz at 20°C, ensuring a working point similar to the one of the reading transistor of the floating gate capacitor. After being recharged, the FGDOS was placed in the oven, applying a trapezoidal temperature profile whose limits were 10°C and 85°C. This range fully covers the working temperature range of the LHC.

The temperature variations were minimized (5°C/hour) to allow the whole chip to reach the measured temperature. The frequency variation versus temperature is shown in Figure 44, where it can be observed how the output variation of the floating gate transistor depends on its working point, which is determined by both the charge stored in the floating gate and the temperature. Indeed, injecting charge in the floating gate to rise the output frequency from 30 kHz to 50 kHz, leads the temperature sensitivity to drop from -315 Hz/°C to -200 Hz/°C at 20°C. To highlight this effect, the temperature sensitivity has been plotted in Figure 45 both for the reference and the output signal. As expected, since the frequency variation of the twin transistor is almost a straight line (see the red curve in Figure 44), the temperature sensitivity does not change significantly from its mean value, i.e. -135 Hz/°C.

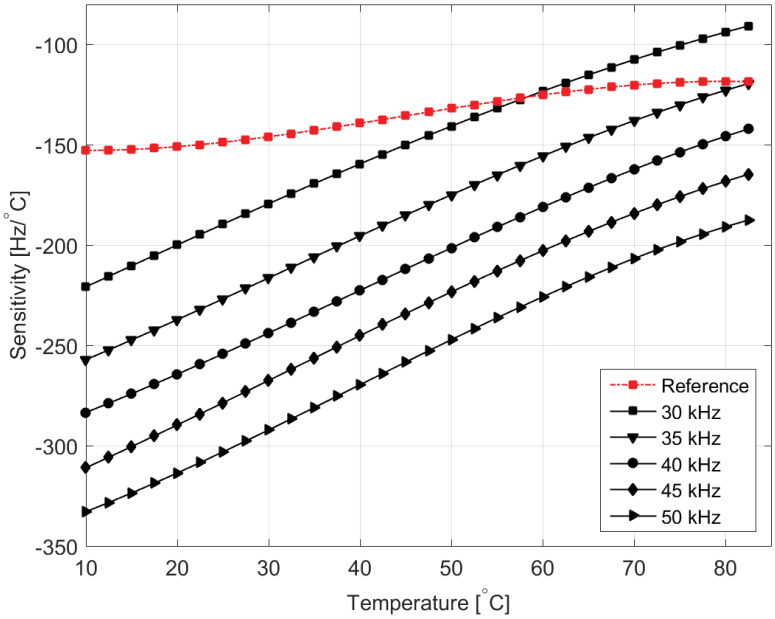

Figure 45. Frequency as a function of temperature. The uppermost curve shows the temperature sensitivity of the twin MOSFET, i.e. the reference frequency. The lower curves show the temperature sensitivity of the floating gate transistors for different amounts of charge stored in the floating gate.

This calibration allowed the implementation of a temperature compensation method based on the information achieved from these experiments: a look-up table has been defined, by means of which it is possible to obtain a signal immune to the temperature variation, without employing any temperature sensor. The compensated frequency is obtained by summing a delta frequency Δf to the output frequency. The Δf is computed by considering the reference frequency and the charge initially stored, i.e. by gauging the output frequency at 20ºC before irradiation.

Since the output frequency is restricted within a range of 20 kHz by the recharge process, the temperature effect has been characterized by considering five different starting points within this range, corresponding to the initial frequency of the experiment explained above: 30, 35, 40, 45 and 50 kHz. Evaluating the starting point makes it possible the selection of the correct curve of Figure 44, whereas the reference frequency variation allows to determine the shift to be considered on the selected curve. The latter can be graphically visualized by substituting the x-axis of Figure 44 with the reference frequency. The shift to be applied to the output frequency can be directly achieved by reading the reference frequency variation and moving on the appropriately selected curve.

An example of the temperature effect compensation is shown in Figure 46, where the temperature profile set by the oven is represented by the red curve, the floating gate output variation is shown in

black and the signal achieved by means of the look-up table is depicted in blue. The look-up table was chosen according to the output frequency at 20°C, which was set to 30 kHz. The blue curve shows how the output variation due to the temperature can be fully compensated by means of the look-up table.

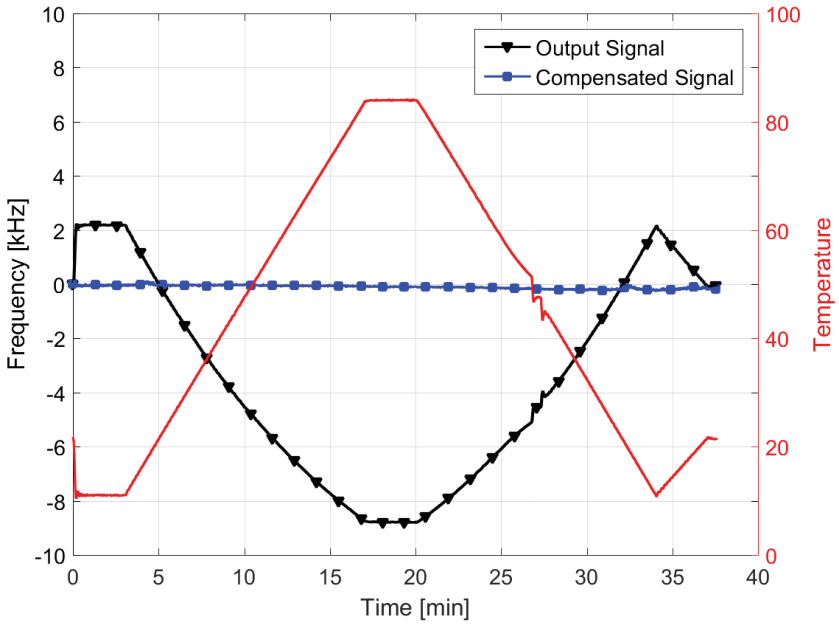

Figure 46. Compensation method implementation. The output signal variation is depicted in black, while the temperature compensation method is applied on the same signal and plotted in blue. In red, the temperature variation

3.5 Passive Mode

The Passive Mode is implemented by evaluating the output frequency before and after the irradiation: the frequency variation obtained can be converted in dose either by using the sensitivity of the FGDOS as a calibration factor or by exploiting the full characteristic as a calibration curve. The first method makes it possible to calculate the dose by linearly approximating its characteristic, whereas the second method requires the use of the whole calibration curve that needs to be stored and implemented through a lookup table.

The characterization of the radiation response is necessary to implement the Passive Mode measurement. For this reason, several irradiations were performed by exposing the FGDOS to the gamma field generated by the ^{60}Co source at the CC60 facility at CERN. Here, the complete calibration curve has

been achieved by irradiating the sensor configured in High and Low Sensitivity. In Figure 47, the calibration curve and the sensitivity (i.e. the derivative of the output frequency with respect to the dose), are plotted against the dose for both the configurations. As can be observed, the High Sensitivity configuration, which is represented by the solid line, makes it possible to obtain a much higher sensitivity than the Low Sensitivity configuration, although the measurable dose range is larger for the latter. The frequency interval corresponding to the linear range is (50 ÷ 80) kHz and (150 ÷ 180) kHz for the HS and LS configuration, respectively. The corresponding measurable dose range results in 0.51 and 2.72 Gy.

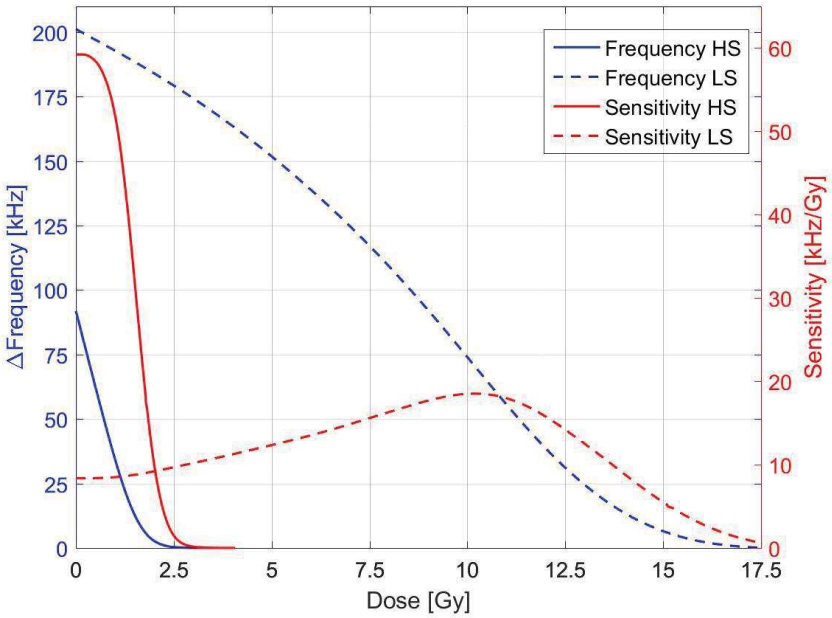

Figure 47. Calibration Curves (in blue) and Sensitivity (in red) are plotted for the HS and LS configuration.

3.5.1 Linear Approximation

The measurement of the dose through the linear approximation is obtained as the ratio between the frequency variation and the average of the sensitivity within the linear range, shortly S_{LR}. (The calibration of S_{LR} is also essential for the operation in Autonomous Mode, as it will be shown in Section 3.6). As long as the frequency variation stays within the linear portion of the characteristic, the error introduced will be negligible, as it will be shown. In the case where the cumulated dose exceeds the linear range, the error introduced will strongly depend on the amount of dose exceeding the linear range, as can be observed in Figure 48, where the error has been evaluated as the difference between the absorbed dose and the dose estimated by the linear approximation.

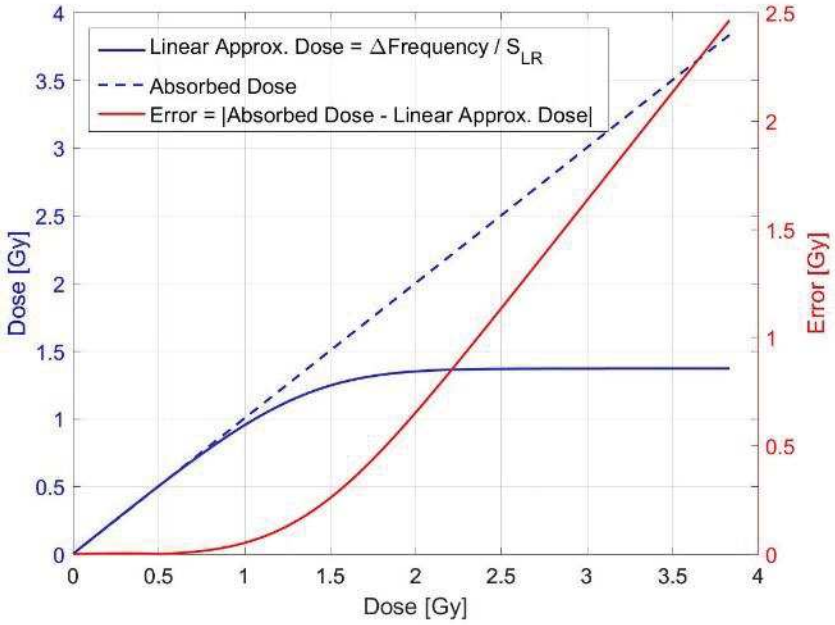

Figure 48. Absolute Error for the Linear Approximation (HS). The error (in red) is related to the right y-axis.

As it can be seen, the error increases abruptly as soon as the dose exceeds the linear range. However, if the measurement is not required to be highly accurate, the dose range can be extended according to the maximum accepted error. For instance, to get an error lower than 15%, the dose range can be extended to 1.43 and 5.53 Gy respectively for the HS and LS configuration. On the other hand, the maximum error given by the linear approximation within the linear range is 2.6 and 90 mGy for the HS and LS configuration, repectively. In case these ranges are not sufficient to cover the expected dose and the error constraints are more restrictive, it is convenient to evaluate the dose by considering the whole characteristic of the sensor.

3.5.2 Calibration Curve

The use of the whole characteristic as a calibration curve is more complicated. A lookup table is required to convert the frequency variation to dose, on the contrary to the only value needed by the linear approximation, i.e. average sensitivity of the linear range. However, this restriction is compensated by two important advantages: it allows the extension of the measurable dose range, and it does not introduce the error due to the approximation of the curve. The dose range extension can be evaluated by fixing the minimum measurable dose allowed by the measurement: since the dose resolution can be calculated by dividing the minimum detectable frequency by the sensitivity, the dose

resolution depends on the working point of the sensor, which depends on the absorbed dose. As a consequence, the lower the sensitivity, the larger the minimum detectable dose, i.e. the dose resolution. This implies that in the lower part of the characteristic, where the sensor loses most of its sensitivity, the minimum detectable dose increases. As the minimum detectable frequency was 30 Hz, the corresponding dose resolution has been evaluated and plotted against the dose in Figure 49 for the HS configuration.

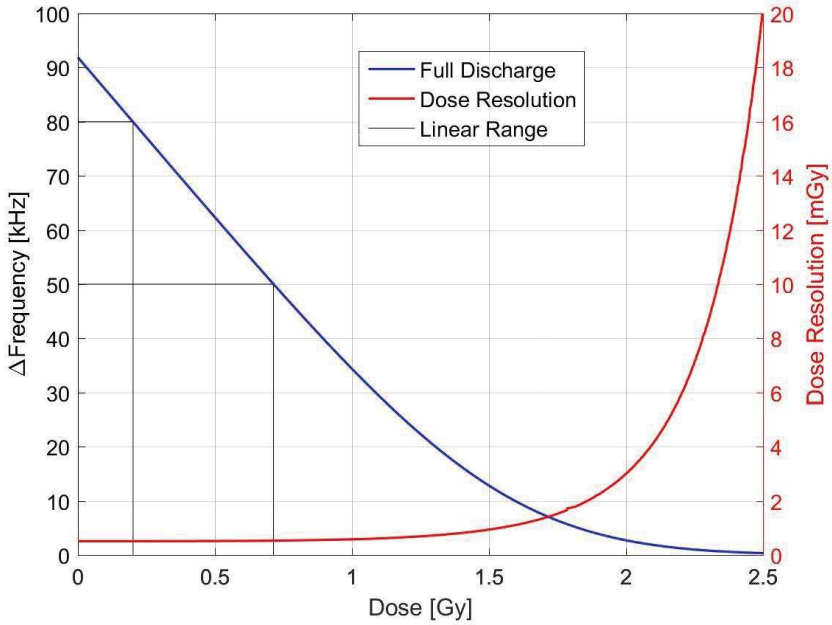

Figure 49. Dose Resolution considering a frequency noise of 30 Hz for the HS configuration

The resolution obtained in the linear range is 0.5 and 3.1 mGy respectively for the HS and LS configuration. The span of the dose range is therefore limited by the maximum accepted resolution. For example, considering acceptable a dose resolution 50% higher than the one achieved in the linear range, the corresponding dose range is 1.18 Gy (HS configuration) and 12.25 Gy (LS configuration). In this way, it is possible to increase the dose range respectively by a factor of 2.3 and 4.5, repectively.

3.5.3 Experiments in Passive Mode

The Passive Mode has been tested by irradiating the FGDOS in both the HS and LS configuration with a dose rate ranging from 0.9 to 2.7 Gy/h at the CC60 facility of CERN. The dose was measured by means of an ionization chamber, which was placed alongside the dosimeter. The distance from the source was enough to achieve high homogeneity of the radiation field to ensure a correct measure

of the dose. The sensors were pre-calibrated by reading the frequency variation throughout the irradiation (hereafter named Active Mode) and compared with the Passive measurements in Table 4. The effect of the temperature on the output frequency has been removed by applying the temperature compensation method presented in[64], which required the temperature characterization of each sensor and the implementation of a correction. In the last column, the percentage difference between the Active and Passive mode with respect to the sensitivity measured in Active mode is reported. As can be observed, the spread among the results is within 2 %, except for the linear approximation in LS configuration, which was found to be much larger. This large difference is due to the non-optimal choice of the linear range, which makes the sensor working in a rather extended portion of the characteristic, where the sensitivity changes significantly (see Figure 47). In order to reduce this effect, the linear range should be shifted in a lower part of the curve, where the sensitivity variation is lower, such as for frequencies ranging from 50 to 80 kHz.

TABLE IV
IRRADIATION TEST RESULTS

CONFIGURATION	MODE	DOSE [GY]	SPREAD W.R.T ACTIVE [%]
High Sensitivity	Active	0.227	-
	Calibration Curve	0.228	0.6
	Linear Approx.	0.230	1.6
Low Sensitivity	Active	0.849	-
	Calibration Curve	0.842	0.8
	Linear Approx.	0.768	9.5

Table 4. Comparison of the Active and Passive Mode sensitivity obtained by irradiating different FGDOS in HS and LS configuration. The percentage difference is evaluated w.r.t. the Active Mode sensitivity and is indicated in the last column.

3.6 Autonomous Mode

The Autonomous Mode is a functionality that allows the reading of the dose by accessing the data through the digital interface, without the need of either recording the online measurement or externally controlling the recharge process. This function can be enabled by writing in the registers of the FGDOS through an SPI interface. The Autonomous Mode allows the calculation of the cumulated dose by the formula:

$$Dose = \frac{nr * LR - \Delta Freq}{S_{LR}}$$

Equation 3.10

where *nr* is the number of recharges, *LR* is the frequency span corresponding to the linear range (i.e. the difference between the target frequency and the threshold frequency), *ΔFreq* is the difference between the post-irradiation and the pre-irradiation frequency, and S_{LR} is the average sensitivity of the linear range. In order to control the recharge process, the logic of the ASIC reads and checks if the output frequency is below the threshold frequency. In this case, the logic triggers the recharge until the target frequency is reached. The number of recharges is stored in the registers to allow the computation of the dose. This technique allows to extend the measurable dose range to be extended up to the TID-lifetime of the sensor, which was found to be in 300 Gy.

3.6.1 Finite Recharge Time

The dose calculated by Equation 3.10 does not keep into account the finite time required for the recharge process to increase the frequency from the threshold to the target value. In fact, the formula approximates the recharge as an instantaneous event, although its duration is finite. As discussed in Section 3.2.2, the charge injection in the floating gate capacitor is triggered by applying a high voltage over the gate dioxide of a transistor, through the Fowler-Nordheim tunnelling mechanism [5]. The high voltage is generated internally by the recharge circuitry, which includes a configurable charge pump chain. The time necessary to perform the recharge is hardly quantifiable because it depends on the dose rate. In fact, if the dose rate is too high, the charge generated by the radiation in the field oxide can neutralize a significant portion of the charge injected through the injector, consequently increasing the recharge time. Nevertheless, this phenomenon has been observed only for dose rates higher than 20 Gy/h. Assuming the recharge time independent of the dose rate, it is possible to estimate the relative error as the ratio of the recharge time over the time of a single discharge. This calculation overestimates the actual error because it does not keep into account the first and the last discharge, where no error due to the recharges is introduced. Therefore, since the time for a single discharge depends on the dose rate, the relative error can be expressed as a portion of the dose rate too. Since the recharge time has been measured for the HS and LS configuration in 10 and 65 seconds, the multiplying factor to calculate the relative error is calculated as $5.4 \cdot 10^{-3}$ and $6.6 \cdot 10^{-3}$, respectively. To get an idea of the influence of the error due to finite recharge time, a dose rate of 10 Gy/h leads to a relative error of 5.4 and 6.6 % for the HS and LS configuration, repectively. As a consequence, the dose calculated through Equation 3.10 underestimates the actual absorbed dose depending on the dose rate. However, to reduce the error, it is worth making the recharge time as short as possible.

For this reason, the number of stages involved in the charge pump chain has been made configurable, so that the injector voltage can be chosen among a set of fice voltage values ranging between 17 V and 19 V. Nevertheless, if the highest value is not large enough, the charge pump can be disabled and the voltage can be applied through an external supply.

3.6.2 Sensitivity Degradation

For dosimeters based on floating gate structures, the sensitivity can decrease with the dose because of the progressive accumulation of positive charges in the field oxide, which decreases the electric field by leading to a higher recombination rate: therefore, the carriers available per unit dose for the neutralization of the charge stored in the floating gate decreases [66]. To investigate the reliability of the sensor over its TID-lifetime, the change of the sensitivity has been investigated by irradiating the sensor working in Autonomous Mode with a dose rate of 25 Gy/h. The sensitivity was measured for each discharge as the ratio between the frequency variation and the dose variation in the linear range. In Figure 50 the sensitivity and percentage variation with respect to the initial value are plotted.

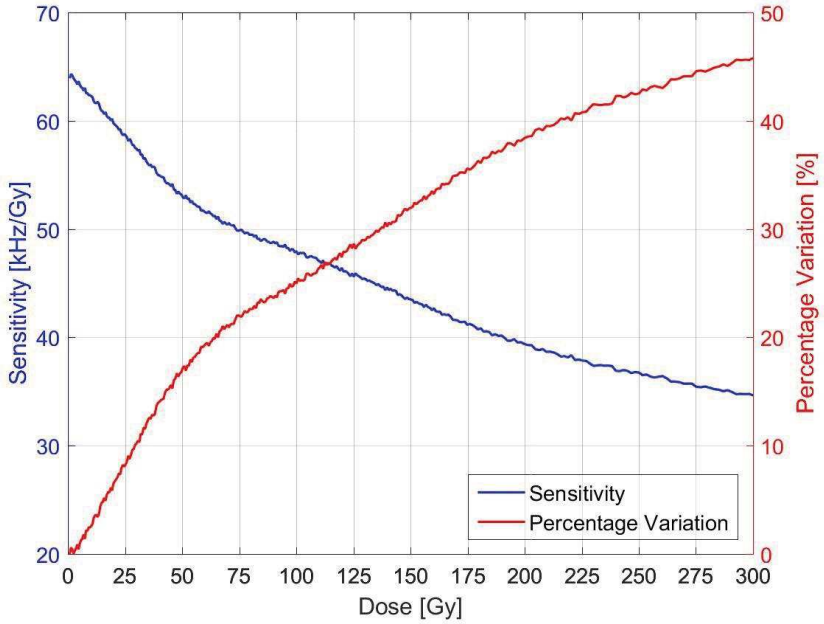

Figure 50. Sensitivity variation over the dose is plotted for the HS configuration. On the right y-axis, the percentage variation of the sensitivity with respect to its initial value is reported.

As can be observed, the sensitivity significantly decreases over the TID-lifetime of the sensor. The highest degradation rate occurs in the first 50 Gy, where the sensitivity changes with a rate of 0.34 % per Gy. Afterwards, it decreases with a rate of 0.14 % per Gy between 50 and 200 Gy and it reaches 0.07 % per Gy in the last 100 Gy. The higher sensitivity degradation rate corresponding to the lower

doses might be due to the larger availability of empty traps that are gradually filled throughout the irradiation.

The sensitivity variation affects the measurement of the dose by introducing an error. Indeed, the calculation of the dose while the sensor works in Autonomous Mode made through Equation 3.10 considers the sensitivity constant during the irradiation. Therefore, since the sensitivity decreases, the dose is underestimated by Equation 3.10. However, although the dose rate was constant during the experiment, the dose interval between each recharge increased with the dose due to the loss of sensitivity. In fact, despite the frequency range was kept constant by the logic of the sensor, which controls the recharge process, the dose interval between each recharge changed depending on the discharge rate, i.e. the sensitivity.

In addition, the finite recharge time contributes to underestimate the dose, since it increases the dose interval between each recharge. Assuming the discharge perfectly linear, the percentage variation reported in Figure 50 can be read as the additional cumulated dose that should be kept into account for each discharge. In Figure 51 the absorbed dose and the dose measured by Equation 3.10 are compared, while the relative error with respect to the absorbed dose is reported on the right y-axis. It is important to notice that the relative error increases with the dose since it integrates the error made for each single discharge, which increases with the dose due to the sensitivity decrease. Therefore, in order to drastically reduce the error two different approaches can be used depending on the irradiation duration. For short irradiations, the sensor should be pre-calibrated to replace the sensitivity value S_{LR} in Equation 3.10. For longer irradiations and in case it is not possible to calibrate the sensor, the characterization reported in Figure 50 has to be used to compensate for the sensitivity degradation.

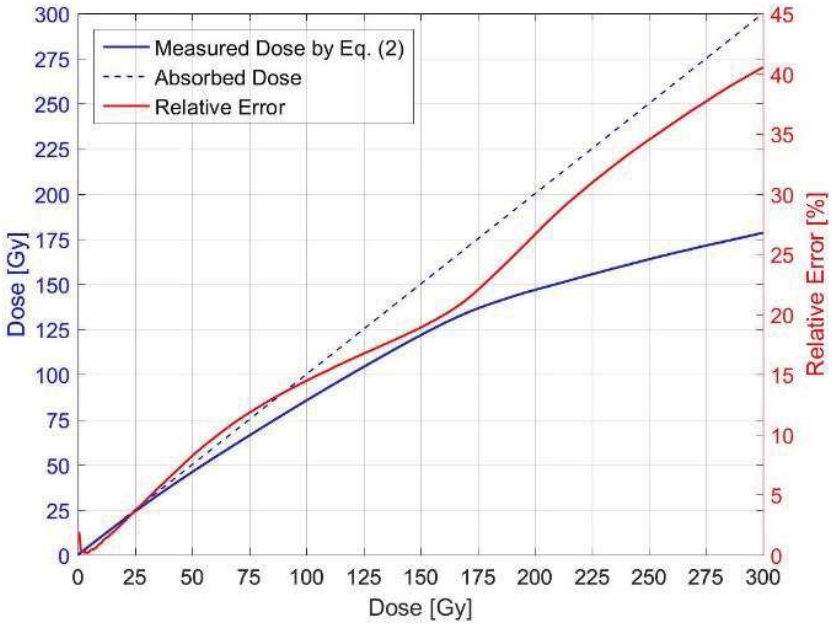

Figure 51. The absorbed dose and the dose calculated by Eq. (2) are compared (left y-axis). The relative error with respect to the absorbed dose is reported on the right y-axis.

3.7 Conclusions

In this chapter, the silicon dosimeter based on a floating gate structure produced by IC-Malaga has been investigated. Firstly, the working principle of the radiation sensitive circuit has been deeply discussed, highlighting the mechanisms that lead to its high sensitivity. Afterwards, the structure of the ASIC has been presented, and the operational modes that can be exploited have been discussed and characterized by performing specific irradiation experiments. In particular, the FGDOS has been analysed to qualify different aspects and to investigate its suitability as TID detector for particle accelerators. The consistency of the radiation response to γ-rays of sensors belonging to the same batch and irradiated in the same conditions has been evaluated and reported in Table 2. The maximum spread obtained is 2.9%: this means that sensors belonging to the same batch behave basically in the same way. On the other hand, a divergence among the radiation response curve of each run has been observed and reported in Table 3.

According to the results obtained through γ-ray irradiations and the sensitivity obtained by considering all the irradiation runs, it is possible to measure the TID by means of the FGDOS making an error lower than 10%. Incidentally, to achieve extremely accurate measurements, the spread among the radiation responses would require to calibrate each sensor prior to its use.

The irradiation tests can take advantage of the excellent linearity of the FGDOS sensor, achieved by using only the most linear portion of the sensor's response curve through use of the

recharge system. Moreover, a test without the process recharge system being enabled has been carried out in order to understand the non-linearity of the full sensor. This is useful in order to know the dynamic of the entire sensor and to better understand its working principle. Indeed, the shape of the curve shows that if the floating gate stores the maximum charge allowed, the sensitivity is lower than that of the value obtained in the linear range, although it should be easier to remove charge from the floating gate when it is saturated. Indeed, the higher the injected charge, the higher the electric field that hinders the recombination. This is due to the trans-characteristic of the reading transistor, which converts the voltage of the floating gate to current.

It is worth to emphasizing that the resolution achieved considering the noise due to both the readout board and the FGDOS itself, is 160 μGy. This value is much smaller than the resolution achievable by means of 100nm RADFET biased to +5V, which is 60 mGy, according to[36].

The Passive and Autonomous Mode have been developed and characterized and summarized in Table 5. For the Passive Mode, two different methods have been shown. The error made by using the calibration curve was found to be very low for both the configurations. The measurements made by the linear approximation werein good agreement with the absorbed dose when the sensor works in HS configuration. On the contrary, the LS configuration showed a significant mismatch between the measurements, due to the non-optimal choice of the linear range. In this concern, the linear range should be shifted where the sensitivity does not change so dramatically. However, to correctly implement this change, the biasing of the radiation sensitive circuit and the temperature sensitive circuit must be modified in the next release of the sensor. This study has also a direct impact on the Autonomous Mode as the choice of the linear range would affect the recharge rate and, as a consequence, the dose error.

TABLE V
MODE COMPARISON

MODE	METHOD	SENSITIVITY	DOSE RANGE [GY]	ERROR [MGY]
Passive	Linear Approx.	High	0.51	2.6
		Low	2.72	90
	Calibration Curve	High	1.18	0.5
		Low	12.25	3.1
Autonomous	Equation 3.10	High	~ 300	5.4·10-3 x DR
		Low	~ 300	6.6·10-3 x DR

Table 5. Summary of the characteristics of the operating modes. For the Autonomous Mode, the error depends on the dose rate (DR).

The operation principle of the Autonomous Mode has been presented. The analysis on the error introduced by the finite recharge time showed its dependency on the dose rate. To overcome this drawback, a faster recharge can be obtained by applying the high voltage externally. The use of the internal recharge circuitry requires the re-design of the charge pump chain, which is in progress. In addition, the ratio between the discharge and the recharge time can be further improved by increasing the linear range, i.e. reducing the dose rate dependency. However, the linear range extension is limited by the worsening of the resolution, which would make difficult the detection of threshold and target value performed by the embedded recharge process. Finally, the self-consistency of Equation 3.10 requires that the sensitivity does not change with the dose. However, the irradiation test showed in Section 3.6.2 highlights that the sensitivity degradation plays a crucial role in the measurement of the dose, introducing a significant error that might invalidate the dose measurement, depending on the requirements of the application. For this reason, it is crucial to understand the sources of this decay, in order to implement a technique that would allow to compensate for this effect. The investigation of this phenomenon will be presented in Chapter 4.

Chapter 4 Investigation on The Sensitivity Degradation

The degradation of the sensitivity limits the performance of the FGDOS in all the operational modes presented in Chapter 3. The error introduced on the dose measurement can be large enough to invalidate the information. A simple way to avoid this problem consists in recalibrating the sensor before every measurement: of course, this requires large availability of means (e.g. access to radiation facilities) and time. The understanding of this phenomenon becomes therefore necessary to improve the accuracy of the measurements. Specifically, it is worth investigating the effects of the cumulated dose on each element that composes the *radiation sensitive circuit* of the FGDOS. For this aim, a test chip has been designed and fabricated, allowing to perform dedicated experiments and to individuate and separate different effects. The control of the recharge process was implemented through a dedicated LabVIEW software that monitored the output current of the *radiation sensitive circuit* and enabled the high voltage whenever it was necessary. The accuracy of the recharges was not as good as the one performed by the TIDMON or the FGDOS itself, although it was enough for the aim of the tests. The results of the recharge process applied to the radiation sensitive circuit is reported in Figure 52, where the dashed curve shows the drain current during the capacitor discharge induced by radiation, while the solid blue curve shows the drain current constrained within the limits by the recharge process.

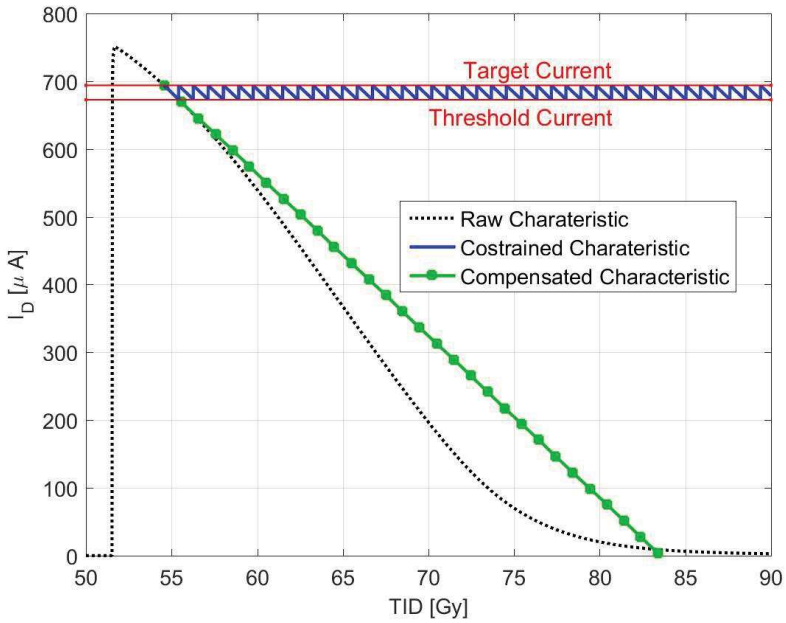

Figure 52. Linearization of the sensor response. The black curve represents the intrinsic characteristic of the core structure, whereas the blue curve shows the response obtained by limiting the working point in the linear region by means of the charge injection.

4.1 Key Elements

In accordance with the description of the working principle discussed in Section 3.1, it is evident that the key elements of the core circuit can be identified as the floating gate capacitor and the reading MOS. Aiming to investigate the behaviour and the performances of each key element, two different structures have been designed and embedded on a test chip. The first structure is equivalent to the NMOS transistor that reads the charge stored in the floating gate capacitor: its drain, gate and source are electrically accessible through the pins of the chip. The second structure reproduces the FGDOS core circuit as in Figure 53, i.e. the floating gate capacitor, the reading transistor and the injector. The two structures are hereafter named *reading structure* and *core structure*, respectively. In Figure 53, a block diagram shows the structures used in the experiments.

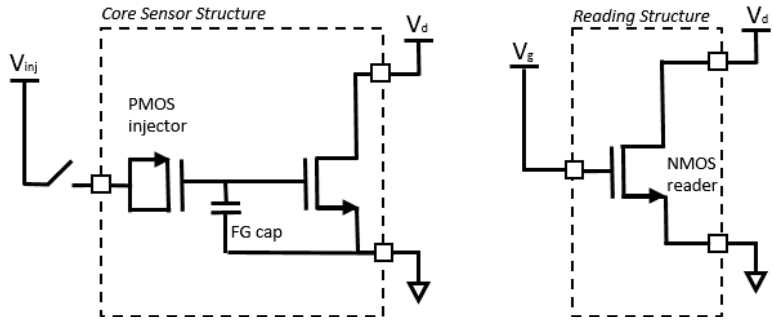

Figure 53. Block diagram of the structures used for the investigation of the FGDOS core circuit. The core structure (left) allowed the investigation of the whole core circuit, which includes the floating gate capacitor, the reading transistor and the PMOS injector. The charge is injected in the Floating Gate through the PMOS injector. The reading structure allowed the analysis of the degradation of the isolated reading transistor.

The aim of the test on the simple reading MOS is to investigate the degradation of its characteristic under irradiation. To do that, the voltage threshold drift and the Id-Vg characteristic were measured during the irradiation test. This allowed to gather important information concerning the influence of the transistor degradation on the radiation response of the core sensor and to try to separate the causes of the sensitivity reduction. The sensitivity of the *radiation sensitive circuit*, i.e. the current variation induced by the absorbed dose, can be expressed as follows:

$$S = \frac{\partial I_d}{\partial Dose} = S_{cap} \times gm$$

Equation 4.1.

where I_d is the drain current of the NMOS transistor, S_{cap} is the sensitivity of the capacitor and *gm* is the transconductance of the transistor. The sensitivity of the capacitor can be defined as the variation of the capacitor voltage induced by the absorbed dose:

$$S_{cap} = \frac{\partial V_{cap}}{\partial Dose}$$

Equation 4.2.

In the next sections both the capacitor sensitivity and the transconductance will be deeply analysed to have a clear picture of the total dose effect on the functioning of the sensor. It is important to bare in mind that the capacitor sensitivity can be reduced by the charges trapped in the field oxide, which would decrease the electric field. In fact, a lower electric field leads to a higher recombination rate, which leads to a smaller fraction of charge surviving the recombination and therefore available for the detection. The reduction of the electric field is proportional to the variation of the voltage on the capacitor, which can be expressed in this way:

$$V_{cap} = V_g - \Delta V_{ot}$$

Equation 4.3

where V_g is the voltage on the gate, and ΔV_{ot} is the shift of the voltage due to the trapped charge. From the reading side, as the recharge process forces the transistor to work in a specific range, a change in the characteristic could lead to a drift of the working point (potentially affecting also the capacitor sensitivity) and to a variation in the transconductance, i.e. modifying the gain of the reading circuitry. For example, the decreasing of the V_{th} induced by the radiation would lead to a decrease of V_g: indeed, the recharge process would inject less charge to reach the target current, as the transistor requires a lower V_g to compensate for the V_{th} shift. In the same way, recharge enabling would occur for lower V_g. Therefore, the change in the electrical properties of the reading transistor leads to a change in the working point of the whole system.

The balance of these elements is crucial for the understanding of the sensitivity degradation. The investigation here presented aims to separate the different effects through analysis of the results obtained from the experiments performed on the *reading* and the *core structure*. In particular, the role of the working point of the reading transistor and the decrease of the electric field in the capacitor due to the charge trapped in the field oxide will be discussed in detail.

4.2 Experiments

Several chips were irradiated with gammas at the CC60 facility at CERN, by means of a ^{60}Co source. For each experiment, two chips were irradiated. The total dose reached was 2.5 kGy with a dose rate of 18 Gy/h. Different tests were performed depending on the structure, aiming to identify and isolate the origin of the degradation for each element.

4.2.1 Reading Structure

Two kinds of reading structure were designed by using different transistor layouts: a standard layout and a ring-shaped layout, commonly named Enclosed Layout Transistor, or ELT [67]. The standard layout is the same as the one implemented in the *core structure*, as well as on the FGDOS: its analysis is fundamental for the understanding of its behaviour. On the other hand, the enclosed layout was tested to investigate a different design that would improve the performance of the sensor. The standard layout was irradiated by biasing the gate of the transistor at 5V or 0V, while the enclosed was biased only at 5V. Both the standard and the enclosed layouts were designed to have the same equivalent W/L ratio. The different biasing allowed to reproduce the best (0V) and the worst (5V) operating conditions. The 5V polarization set the transistor in a working condition similar to the one normally

used by the FGDOS. The drain voltage was also set according to the FGDOS polarization. A first experiment was performed by measuring the V_{th} shift in these bias conditions. During the reading phase, the transistor was configured in diode mode[3] and a constant current was forced at the same time. This configuration made it possible to measure the V_{th} shift by reading the drain voltage (V_d) shift [36].

To have more information about the total dose effects on the reading structure, the characteristic of the standard transistor whose gate was biased to 5V was measured during the irradiation. Aiming to cover the operational range of the sensor, the voltage on the gate was swept between 0V and 6V. Since this process takes a few minutes, it has been necessary to stop the irradiation to guarantee the correctness of the measurement.

4.2.2 Core Structure

The irradiation of the core structure was performed by measuring the drain current of the transistor and the sensitivity variation over TID. Aiming to investigate the influence of the electric field across the capacitor on the sensitivity, the core structure was irradiated by changing the injection rate and the working point of the transistor. The former consists in the amount of dose to be cumulated before activating the injector. The latter is the voltage range on the floating gate that allows the circuit to work between the threshold and the target current. Both these parameters affect the electric field since it is directly related to the average charge stored in the capacitor over time. To force the sensor to work in a specific working point, with a certain injection rate, the charge injection process was suitably controlled during the experiments.

Three different runs were performed, hereafter referred to as Run 1, Run 2 and Run 3, each of which was characterized by specific conditions. Different injection rates were used during the experiments: in Run 1, the charge injection was activated every 60 Gy in the first 200 Gy and every 120 Gy for the rest of the irradiation. During Run 2, the injection interval was changed several times throughout the irradiation from 3 Gy to 24 Gy. In particular, it was kept constant to 3 Gy for the first 300 Gy, and to 6 Gy for the following 600 Gy. Run 3 was performed by keeping the injection rate constant to 5.25 Gy, which is comparable to the one used during Run 2. To make the discussion simpler, irradiations with injection periods shorter than 30 Gy, i.e. Run 2 and Run 3, will be indicated as *High Injection Rate* (HIR), whereas longer injection periods (i.e. Run 1), will be named *Low Injection Rate* (LIR).

[3] In this mode, the drain and the gate are shorted: the transistor works in the saturation region, and the drain current is given by the formula: $I_d = \frac{1}{2}\mu\, C_{ox}\, {}^{W}/_{L}\, (V_{gs} - V_{th})^2$

The low injection rate used during Run 1 was fundamental to measure the sensitivity corresponding to a very low electric field. Indeed, since the injector is activated with a much lower frequency with respect to the other runs, the average stored charge is low as well, and so the electric field. Higher electric field values were explored by biasing the sensor in two different working points, i.e. setting the recharge process to fix the two different current ranges for Run 2 and Run 3. Specifically, during Run 2 the sensor was biased within the High Working Point (hereafter HWP) range, which corresponds to the polarization used in the FGDOS, i.e. with the voltage drop on the floating capacitor ranging 20 mV around 4.15 V. During Run 3, the sensor was biased in the Low Working Point (or LWP) range, which corresponds to a voltage drop of 2.3 V, keeping the same voltage range of 20 mV: this condition implies an electric field almost halved with respect to the HWP polarization range.

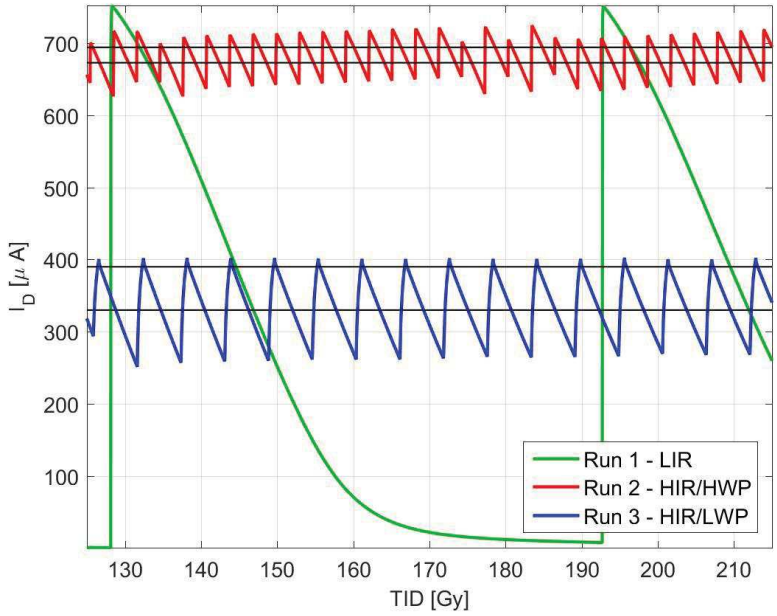

Figure 54. Output current of the core structure under irradiation during the two runs. The injection interval was 60 Gy and 3 Gy for Run 1 and Run 2, respectively. The linear range is the portion of the curves included within the horizontal red lines.

In Figure 54, the output current for all the runs is shown. To make the figure comprehensible, a short irradiation range has been plotted, where the injection interval was 60 Gy, 3 Gy and 5.25 Gy for Run 1, Run2 and Run 3, respectively. It is evident that such short injection periods used in Run 2 and Run 3 lead to a current range much lower than the one achieved during the first run, although the current excursion allows to cover the whole linear range in all the runs.

The HWP and LWP ranges are highlighted in the figure by the horizontal lines: in both cases, the span of the voltage on the capacitor is 20 mV, which is converted to different current ranges through the characteristic of the MOSFET. In Table 6, the combinations of injection rate and working point are summarized for each run.

TABLE IV
EXPERIMENT CONFIGURATION

	INJECTION RATE	WORKING POINT
Run 1	Low	High
Run 2	High	High
Run 3	High	Low

Table 6. Experiment conditions for each run

4.3 Results

The results here presented concern only one of the two chips irradiated during each experiment, as the chips behaved in the same way and their difference was negligible. The variation of the V_{th} shift and the output current slope was found to fall respectively within the 2% and 5%, for all the runs.

4.3.1 Reading Structure

In Figure 55, the variation of the drain voltage obtained by applying a fixed current to the transistor is represented for different biasing and layouts. Assuming that the V_{th} shift is the main change among the electrical properties of the transistor, its variation would correspond to the V_d variation. As it will be pointed out, this hypothesis will not be confirmed for the standard layout biased at 5V.

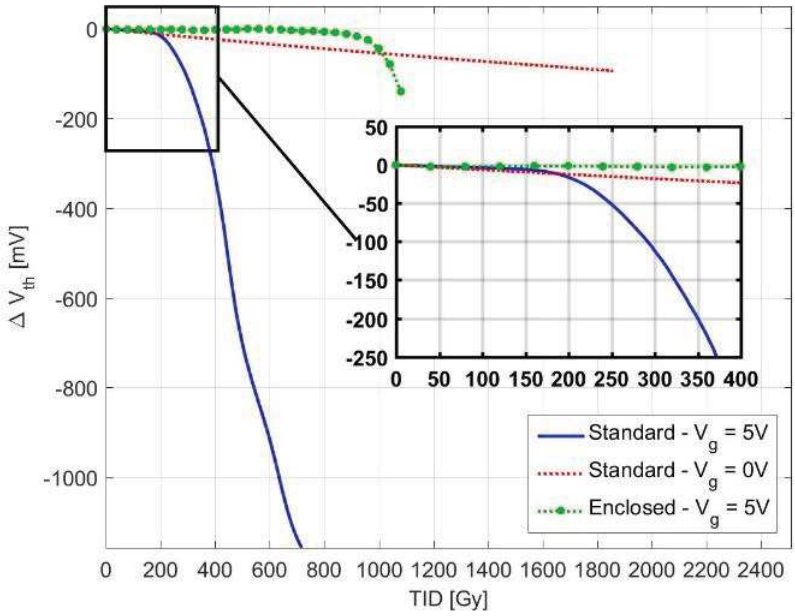

Figure 55. V_{th} variation of the reading transistor exposed to ionizing radiation. The shift of the V_{th} was measured by keeping the transistor in diode mode and reading the V_d variation while a fixed current was forced in the channel. Here, the standard transistor biased to 5V and 0V and the enclosed structure biased to 5V are shown.

However, as can be observed in the zoomed area box, the voltage of the standard transistor biased to 5V starts to drop quickly after 200 Gy, although the drop before this value is negligible (lower than 16 mV). It is worth noting that the method used to measure the V_{th} shift does not allow the evaluation of variations that would lead the drain voltage V_d below the ground.

In addition, the standard layout was also irradiated with 0V on the gate, instead of applying 5V, resulting in a much softer degradation. The shift of the V_d in this test is proportional to the radiation with a rate of 50 mV per 1 kGy.

On the same chart, the voltage shift of the enclosed transistor biased to 5V has been plotted. To improve the radiation tolerance of the sensor preserving the same aspect ratio, the layout has been designed by implementing the rules presented in [68]. In this case, the voltage drop is extremely low compared to the standard layout biased at the same potential, as it reaches 16mV at 1 kGy.

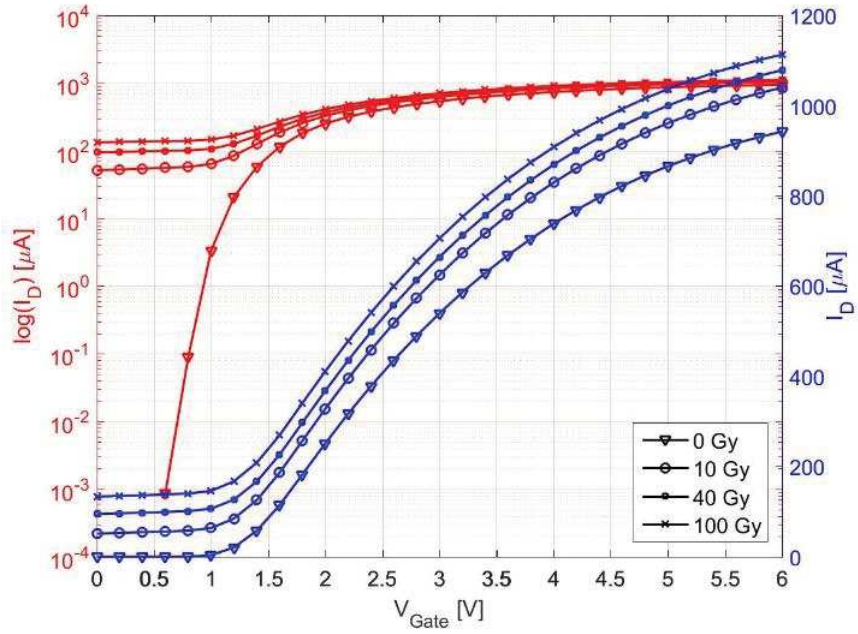

Figure 56. I_d-V_g characteristic of the reading transistor for different doses. The curve was obtained by sweeping the V_g and keeping the drain at 0.5 V, as in the operational mode. During the irradiation, the gate was set to 5V.

Aiming to verify the matching between the V_d and the V_{th} shift, the characteristic of the reading transistor biased to 5V has been measured and reported in Figure 56 for different doses. As can be seen, the curve considerably moves upwards with the dose, which indicates a leakage current flowing in parallel to the transistor. In order to emphasize the influence of leak on the characteristic, the same curves are reported in a logarithmic (left y-axis) and linear (right y-axis) scale, respectively in red and blue. The logarithmic curves clearly show the influence of the leakage current for low voltages, where the offset significantly changes the behaviour of the transistor. On the other hand, the small shift towards left that indicates the decrease in the threshold voltage is negligible, as well as the change of the slope of the characteristic, which is related to the degradation of the mobility [25].

4.3.2 Core Structure

In Figure 57, the drain current of the core sensor during the first run is shown. As can be observed in the first part of the graph, a recharging interval of 60 Gy was enough to completely switch off the transistor, i.e. to obtain a capacitor voltage drop lower than V_{th}. Nevertheless, after a few recharges, the 60 Gy intervals were increased to 120 Gy to achieve the whole discharge of the capacitor: at this moment, we assumed that the decrease of V_{th} required a lower voltage on the capacitor to completely switch off the transistor. This hypothesis was proved wrong by the analysis of the experiments reported in Figure 56: as the leakage current started to contribute to the read current, this offset could not be compensated for by neutralizing the charge in the capacitor through the increasing of the

interval between injections. The increment of the bottom of the current over the dose in Figure 57 shows the effect of the leakage path that drains current even when the capacitor is completely discharged.

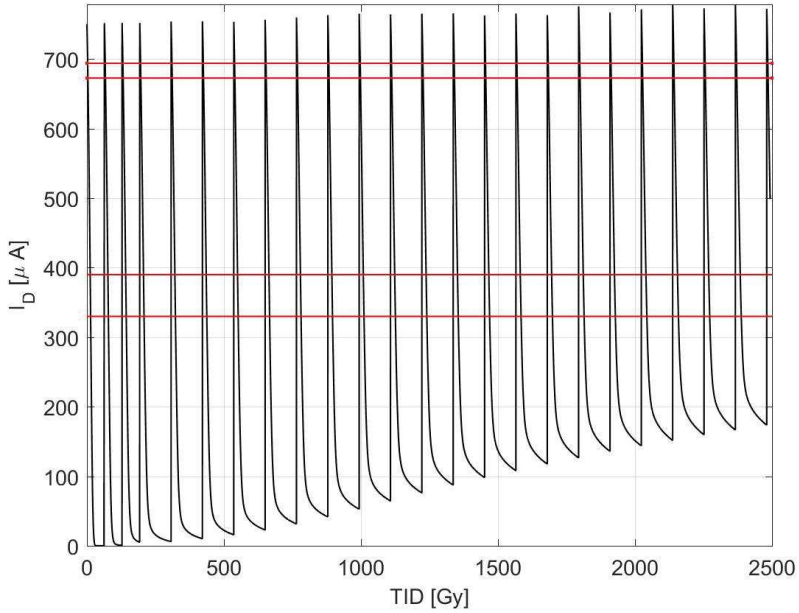

Figure 57. Drain current of the core structure under irradiation. The injection of the charge allows sweeping a large portion of the characteristic, which include the linear range (corresponding to the current range limited by the two horizontal red lines).

A comparison of the sensitivities as a function of the dose is shown in Figure 58. The sensitivity has been evaluated by the current variation over the dose variation in the considered range. As can be seen, the initial sensitivity strongly depends on the working point of the sensor: for the HWP and LWP the sensitivity is 31.0 and 39.4 µA/Gy, respectively. Considering that the LWP region implies a lower electric field, the capacitor sensitivity S_{cap} will be reduced. Consequently, to obtain a higher sensitivity according to Equation 4.1, the increase of the *gm* has to compensate the S_{cap} reduction. As it will be explained in the next section, to make the transistor working with its highest *gm*, the gate has to be biased to ~1.8 V.

For all the runs, it is evident that the worsening of the sensitivity is more intense in the first part of the irradiation, after which becomes flat for Run 1 (where the low injection rate was used), whereas it continues lowering for both Run 2 and Run 3 with a similar rate.

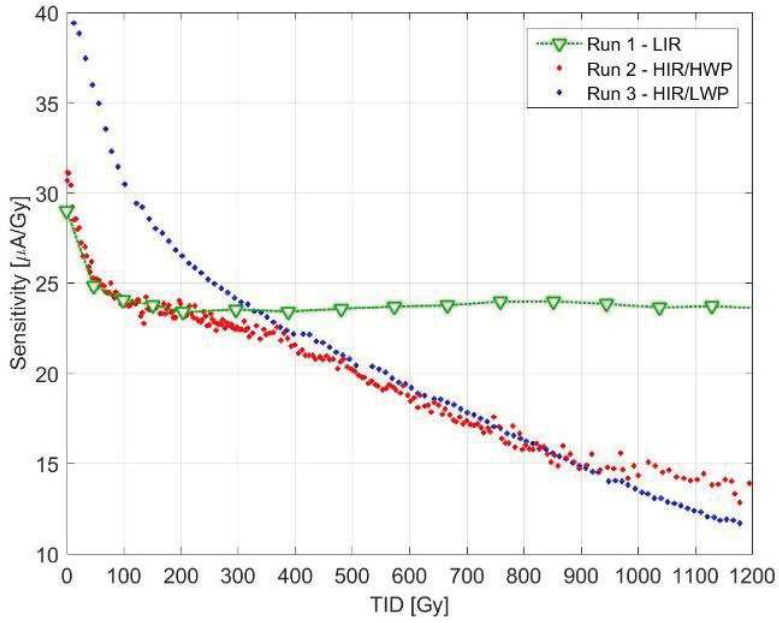

Figure 58. Sensitivity variation over the cumulated dose. The red and blue symbols represent the second and the first run, respectively. Each recharge interval is represented by a specific symbol, as reported in the legend.

4.4 Discussion

In this section, the role of the elements affecting the functioning of the sensor will be analysed. In order to properly interpret the graph of Figure 58, it is necessary to separate two different effects. Hereafter, the influence of the leakage current on the working point will be discussed in detail, focusing on the change in the *gm* and the V_g, as well as the impact of the charge trapped in the insulator layer of the capacitor, i.e. the field oxide, on the sensitivity of the sensor.

4.4.1 Working Point Drift

As pointed out in Section 4.2.1, the main effect on the standard transistor biased at 5V caused by radiation is a leakage current flowing in parallel to the channel of the drawn transistor. This kind of leakage can be generated by the positive charge trapped in the oxide of the Shallow Trench Insulator (STI), used to isolate the transistor from the rest of the circuit [69]. To understand the effect of the current offset on the behaviour of the transistor it is convenient to analyse the shift of the characteristic and the variation of the transconductance at the same time. In Figure 59, the *gm* and the drain current I_D as a function of the dose are shown for different doses. A first major consideration concerns

the influence of the leakage current on the transconductance: observing the superimposition of the *gm* curves, it is evident that the current offset does not have a direct effect on the transconductance. In addition, the invariance of the *gm* confirms that the leakage current flows parallel to the transistor and not through the gate.

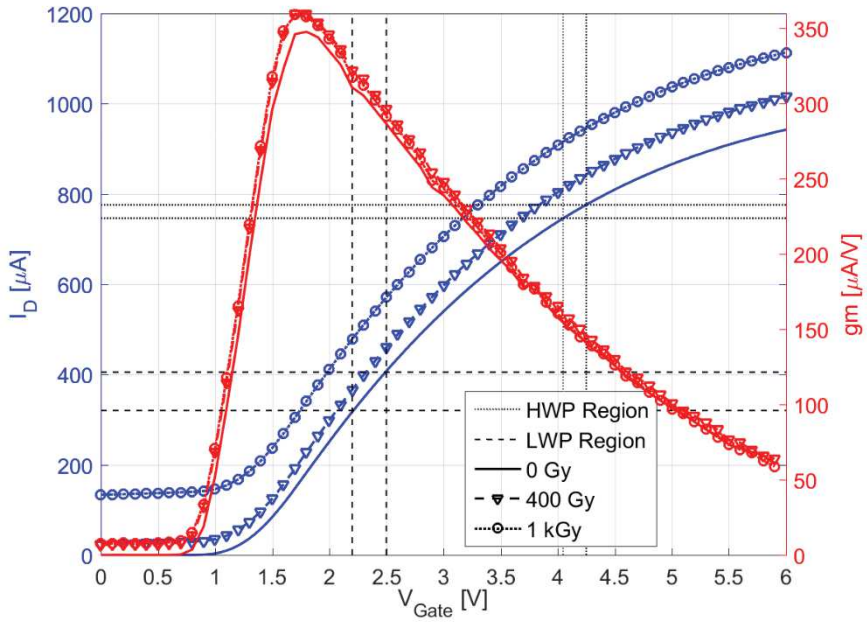

Figure 59. The I_d-V_g curve and the *gm* of the transistor of the reading structure for different doses. The characteristics are drawn in blue and are linked to the left y-axis, while the transconductance are drawn in red and they are linked to the right y-axis. The two working regions (HWP and LWP) are circled for the pre irradiated characteristic.

A second important consideration concerns the leakage current that entails a drift of the working point: as mentioned before, the current range is externally fixed by the recharge process, which monitors the output current and does not change during the irradiation. This means that, when the I_d-V_g curve shifts upwards, the V_g must change to achieve the current required by the recharge process. Therefore, the current offset modifies the working point of the transistor by lowering the V_g to obtain the same current. Consequently, both the *gm* and the V_g will change affecting the global sensitivity. As pointed out, the transconductance is directly related to the sensitivity through Equation 4.1. At the same time, the lowering of V_g affects the capacitor sensitivity and therefore degrades the global sensitivity.

Depending on the working region, the effect of the shift of the characteristic on the *gm* will be different. Starting from HWP region, the increase of the current offset (i.e. the decrease of the V_g) pushes the working point towards higher *gm* values, as long as the gate voltage is lower than ~1.8 V, where the maximum transconductance is reached. On the other hand, starting from the LWP region leads

to a higher *gm*, which might abruptly drop if the offset of the current forces the V_g to values lower than 1.8V. Moreover, looking at the pre-irradiated characteristic in Figure 58 makes it possible to explain the source of the higher global sensitivity for the sensors working at LWP: the increase of transconductance is enough to compensate the decrease of electric field in the oxide due to the lower V_g.

4.4.2 Trapped Charge in the Capacitor's Field Oxide

As mentioned above, the drift of the working point is not the only phenomenon that influences the functioning of the sensor: the charge trapped in the field oxide has an impact on the efficiency in collecting the charge generated by radiation. In fact, since lower electric fields result in higher recombination rates, the fraction of electron-hole pairs surviving the recombination, i.e. the charge available for detection, is lower if some charge is trapped in the capacitor [56]. As a consequence, the sensitivity of the capacitor will decrease with the decrease of the voltage dropping on the capacitor itself: the charge trapped in the oxide will reduce the electric field generated by the charge stored in the floating gate, and thus the sensitivity. According to Figure 1 in [70], the charge yield increases linearly with the electric field, at least in the 0-1 MV/cm range, which extensively covers the values involved in the functioning of the sensor. In the same way, it is reasonable to approximate the capacitor sensitivity as a linear function of V_{cap}:

$$S_{cap} = k_1 V_{cap} + k_2$$

Equation 4.4

Where the slope k_1 and intercept k_2 have been experimentally deduced by the initial sensitivity for the HWP and LWP region shown in Figure 58. Indeed, combining equation Equation 4.1,Equation 4.3 and Equation 4.4, considering that in the beginning of the irradiation ΔV_{ot} is zero, it is possible to calculate both the parameters.

To deeper investigate the S_{cap} variation, it is important to make some considerations about rate of the trapping charge. It is reasonable to assume that the voltage shift due to the trapped charge ΔV_{ot} is proportional to the charge yield modulated by the trapping probability [25]. Again, the charge yield will be linear with the electric field, and therefore with the V_{cap}. To verify this statement, it is possible to compute the degradation rate in the first 100 Gy for Run 2 and Run 3, during which different bias conditions were applied being the same the injection rate. In this dose range, the transistor does not change its characteristic, as can be seen in Figure 55. Hence, the only effect influencing the sensitivity will be the S_{cap} degradation due to the trapped charge.

Concerning the effect of the trapped charge on the transistor characteristic, it is important to notice that a positive charge trapped in the field oxide of the capacitor would shift both the I_d-V_g and the *gm* curve in horizontal towards left in Figure 59: being equal the current range considered, the working point does not move on the characteristic, and so the *gm*. Therefore, the effect of charge trapped in the floating gate capacitor affects only the capacitor sensitivity. On the other hand, the vertical shift due to the leakage current indirectly affects the capacitor sensitivity (by lowering the V_g) and the *gm*.

4.4.3 Combination of the Effects due to the Working Point Drift and the Trapped Charge

The two factors determining the sensitivity, i.e. the capacitor sensitivity and the transconductance, are simultaneously affected by the shift of the working point. At the same time, the charge trapped in the capacitor insulator layer decreases the $S_{cap.}$ To highlight the role of the two effects, the sensitivity can be expressed by combining Equation 4.1, Equation 4.2 and Equation 4.4:

$$S = gm \times \left(k_1 V_{cap} + k_2\right) = gm \times \left[k_1\left(V_g - \Delta V_{ot}\right) + k_2\right]$$

Equation 4.5

The sensitivity resulting from Equation 4.5 is shown in Figure 60 as a function of the V_g. The pre-irradiated characteristic of the transistor is illustrated in blue and it is related to the left y-axis, whereas the red curves are related to the right y-axis and represent the evolution of the sensitivity for three specific amounts of trapped charge. In particular, the solid line shows the sensitivity before the irradiation, i.e. without any charge trapped in the oxide: as expected, the highest value is about 40 µA/Gy and corresponds to the LWP region, in agreement with the results presented in Figure 58. The dotted line shows the sensitivity after 100 Gy for Run 2 (HIR-HWP), whose corresponding equivalent voltage shift ΔV_{ot} results 0.67 V. The dashed red line shows the sensitivity after 100 Gy for Run 3 (HIR-LWP). The equivalent voltage shift ΔV_{ot} at this point results in 1.12 V. It has been possible to retrieve this information only considering the first irradiation range, where the transistor properties were not altered yet and the effect of the trapped charge could be isolated. In this way, it has been possible to show that the degradation of the S_{cap} due to the trapped charge pushes the sensitivity curve downwards, attenuating the global sensitivity for any polarization.

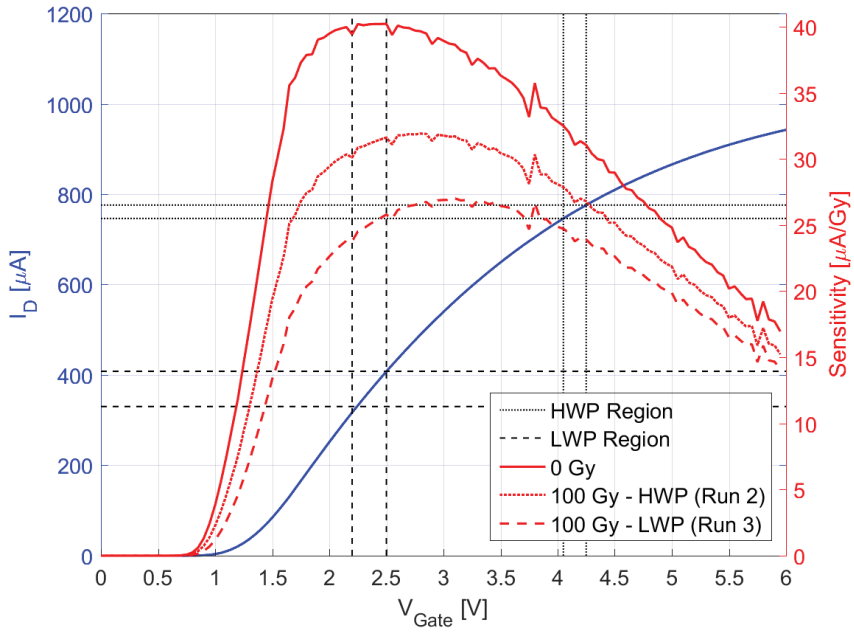

Figure 60. Drain current (in blue) and sensitivity (in red) as a function of the gate voltage. Different sensitivity curves are shown: the solid line represents the pre irradiation sensitivity, the dotted line shows the sensitivity after 100 Gy with the sensor working in the HWP region (Run 2) and the dashed line is the sensitivity after 100 Gy with the sensor working in the LWP region (Run 3).

The effect due to the drift of the working point produced by the leakage current, i.e. shift of the characteristic upwards, can be discussed by focusing on one of the sensitivity curves, for instance the pre-irradiate curve. As shown before, this shift does not change the shape of the transconductance, although it modifies the working point of the transistor: in other words, to keep the same current range, the V_g has to be lowered as the characteristic goes up. In principle, according to the figure, starting from the HWP and moving towards lower voltages would lead to an increase of the sensitivity. Nevertheless, it must be kept in mind that while the working point drifts, the capacitor sensitivity decreases because of the trapped charge. The effect on the chart would be to move the working point towards left (because of the working point drift) meanwhile the curve is pulled down by the lowering of the V_{cap}.

By means of this analysis, it is possible to explain the behaviour of the sensor shown in Figure 58 for the different irradiation conditions. For example, as already pointed out, the degradation rate strongly depends on the voltage dropping on the capacitor. This explains why during Run 1 the sensitivity degradation becomes negligible after the first drop: in this experiment, the capacitor was charged very few times with respect to the whole irradiation period, applying, on average, a much lower electric field on the capacitor oxide than for the other experiments. It is also reasonable to assume that this condition is more similar to a transistor biased to 0V rather than 5V, as the one

represented by the dashed curve in Figure 55. Thus, it can be deduced that during Run 1 the shift of the transistor characteristic is consistently lower than the one represented in Figure 56, the absorbed dose being equal. For this reason, the working point would not move as fast as of the other runs. On the other hand, the average electric field was very low and a minor amount of charge became available throughout the irradiation for the oxide trapping. Assuming that the transistor was not affected by any leakage during Run 1, then the only source of the sensitivity variation would be the capacitor degradation. However, after 200 Gy, the abrupt lowering of the sensitivity degradation rate (which is evident also for the other runs) suggests that the decrease in the V_{cap} is not the only responsible of this effect (otherwise the degradation rate would have been constant). This phenomenon can be explained by a sudden drop in the trapping probability, which would make the charge trapping more difficult and, consequently, reduce the degradation rate.

The same arguments cannot be applied for Run 2 and Run 3, since the two effects act simultaneously, except for the first part of the irradiation (where the transistor does not change its properties). The comparison of Run 2 and Run 3 (i.e. HWP versus LWP) in the first 200 Gy has been discussed in Section 4.4.2. After this point, both the working point shift and the trapped charge affects the sensitivity. In Run 2, during which the sensor was set to work in the HWP region, the offset of the current leads to an increase of the sensitivity, as long as the V_g is lower than 2.4 V (see Figure 60). Therefore, in this voltage range, the offset of the current increases the *gm*, in contrasts with the decrease of the capacitor sensitivity due to the trapped charge. However, the increase of the *gm* is not enough to compensate for the decrease of the S_{cap}. During Run 3, the evolution of the sensitivity is different. In this case, the sensor works in the LWP region, which corresponds to the highest sensitivity value. Thus, the offset of the characteristic leads to a lowering of the sensitivity. Moreover, if the current offset is enough to require voltages lower than 1.6 V, the sensitivity drops abruptly. Therefore, for the LWP region, both the working point drift and the trapped charge lead to a decrease of the global sensitivity.

4.5 Conclusions

In this chapter, the contributions of the sensitivity degradation of dosimeters based on floating gate structure have been deeply examined. The analysis of the results allowed the understanding of the factors influencing the functioning of the core sensor: to do so, the sensitivity has been analyzed by splitting the sensor in two different stages, namely the floating gate capacitor and the transistor. The influence of the total dose on each stage acts through two different mechanisms,

which have been identified in the trapped charge in the field oxide and the change of the characteristic of the reading transistor. In particular, the trapped charge reduces the sensitivity of the capacitor and shifts the curve of the transistor in horizontal. Although the horizontal shift does not have any impact on the gain of the reading stage, the degradation of capacitor sensitivity significantly affects the sensitivity of the sensor. On the other hand, the functioning of the transistor is influenced by a parasitic channel generated by the trapped charge in the STI, which drains a current in parallel to the channel of the transistor. This current, which does not depend on the $V_{g,}$ shifts the characteristic of the transistor upwards, affecting both the capacitor sensitivity and the transconductance of the transistor itself at the same time. Indeed, since the current range is externally forced, the V_g shifts to compensate the offset of the current. This drift in the working point leads to a change in the *gm*, which could increase or decrease depending on the initial working point, and to a decrease of the V_g, which implies a lower electric field in the field oxide of the capacitor: as a consequence, the capacitor sensitivity decreases. It is important to notice that the capacitor sensitivity is affected by both the current offset and the trapped charge.

The analysis here presented allowed the separation of the phenomena impacting on the working of the core circuit of the FGDOS. The investigation on the reading transistor highlighted the importance to employ a radiation hardened layout, which would cancel out the variation of the gain of the reading stage (i.e. fixing the *gm*), and the contribution on the degradation of the capacitor sensitivity due to the decrease of the V_g induced by the shift of the characteristic. The radiation hardness of the transistor is crucial to fix the working point and improve the performance of the sensor: the enclosed transistor tested would be suitable for this purpose.

Concerning the analysis on the capacitor sensitivity, it has been shown that its degradation depends essentially on the electric field across the capacitor and on the quality of the field oxide. The former directly affects the degradation rate and can be reduced by using the sensor in the LWP region, which would make sense only if the transistor does not change the working point. The latter is strictly related to the fabrication process: since the field oxide is much thicker than the gate oxide, it is usually grown by means of rapid processes, which induce a poorer quality of the oxide[71]. As it may be difficult and more expensive to implement a better quality process, the effect due to the trapped charge needs to be mitigated in a different way. A possible compensation method is currently under study and can be performed by using the injector and the floating gate capacitor as a capacitive voltage divider. In principle, the decrease of electric field can be compensated by applying a specific voltage on the injector, which will be divided between the injector and the capacitor. Of course, this

voltage has to be calculated according to the degradation of the sensor and the transistor working point. In addition, it must be lower than the injection threshold.

An alternative method can be implemented by exploiting the effect induced by the leackege current: the idea would be to generate a controlled current that flows in parallel to the current of the reading transistor. This current would shift the working point of the reading transistor towards a higher *gm*, compensating the lowering of the capacitor's sensitivity. The parallel current can be easily generated by integrating an NMOS transistor in parallel to the one used to read the floating gate capacitor. The voltage gate of the parallel transistor should be properly tuned to control the sensitivity compensation.

Moreover, the strong degradation seen in the first part of irradiation can be reduced or canceled by pre-irradiating the sensor before being used. Indeed, according to the investigation here presented, it is reasonable to assume that the trapped charge is the main responsible for this initial degradation. In fact, looking at the trend of the sensitivity of Run 1 (HWP-LIR) in Figure 57, assuming that the current leakage is negligible (as the polarization condition is closer to the standard transistor biased to 0V in Figure 55), the degradation rate should be constant over the cumulated dose. However, the knee of the curve around 200 Gy is in contrast with this statement, probably because the trapping probability changes at this point. This might be explained with the presence of a considerable amount of empty traps in the field oxide, which are easily filled by the charge generated by the separation of the electron-hole pairs in the first part of the irradiation.

Chapter 5 Qualification for Accelerator-like Environments

The behaviour of the NMOS and the FGDOS in mixed radiation field environments needs to be investigated to understand the suitability of these dosimeters for TID measurement along the CERN accelerator chain, where radiation fields can be very different in terms of intensity, composition, and spectrum [72]. For this purpose, accelerated radiation tests in representative environments were performed at CHARM, the new mixed field facility available at CERN [14], where it is possible to achieve different radiation fields by changing the facility configuration. Here, the radiation response to the mixed field of FGDOS and NMOS has been compared with the RADFET, which is the semiconductor dosimeter currently used for TID monitoring at CERN.

5.1 Accelerated Irradiaton Tests at CHAM

The Cern High energy AcceleRator Mixed field (shortly CHARM) is a unique mixed radiation test facility, which can reproduce radiation environments representative of particle accelerators, as well as some of the radiation fields met by ground, atmospheric and space applications. This facility has a crucial role in reducing the downtime of the accelerator, as it improves the qualification process for electronic equipment installed in the tunnel and its adjacent area. Indeed, due to radiation-induced (permanent or temporary) failures, it might be necessary to dump the beam to intervene for repairing or replacing the equipment. These operations can require a considerable amount of time during which the accelerator does not work, reducing the efficiency of the machine. To minimise the failures due to cumulative and stochastic effects induced by radiation, electronic systems placed along the accelerator chain needs to be qualified before their installation. The qualification process involves accelerated testing in radiation environments similar to the one foreseen in the operational area. Before the test phase, Fluka simulations are performed to model the radiation field expected during the operation of the accelerator where the equipment will be installed. These simulations allow predicting the kind of particles, their fluence and energy spectrum that compose the radiation field in the considered area. This information is then translated into quantities measurable by the RadMon system, therefore defining the targets to be reached during the accelerated tests in terms of TID, 1-MeVeq, HEH and ThN fluence.

At CHARM, the radiation field is achieved as the result of a 24 GeV proton beam impinging on a target. The beam is delivered by CERN's Proton Synchrotron in bunches of protons lasting 300 ms, whose intensity is monitored through a Secondary Emission Chamber (SEC) placed upstream from the facility. In Figure 61, the layout of the irradiation room is depicted. The size of the room (approximately 70 m^3) allows the irradiation of large systems such as whole satellites or power converters for supplying the magnets and the radio frequency systems deployed along the hadron collider. The irradiation of more systems or many components (for example for batch testing) at the same time is also possible, according to the needs of each single test.

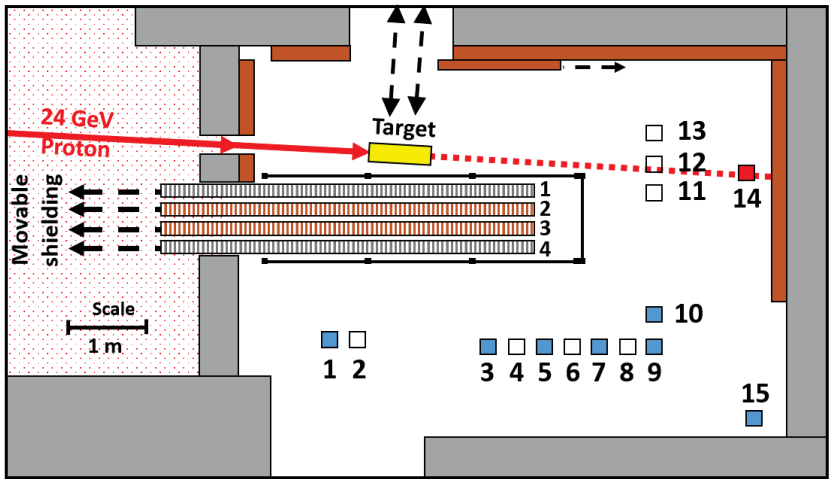

Figure 61. Layout of the irradiation room at CHARM

The particle shower generated by the interaction between the beam and the target has different characteristics depending on the test position, the density of the target and the shielding configuration used. Depending on the position, both the intensity and the energy spectrum of the radiation field change. Due to the momentum conservation, the lower the angle between the beam's directrix and the straight line that goes from the target to the test position, the harder the spectrum. This implies that for position 10-15 (so-called *longitudinal positions*) the environment is "hard", as the energy of the particles can reach 10 GeVs. On the other hand, for wider angles (i.e. for positions 1-9 that are called *lateral positions*), the energy of the particle does not exceed 2 GeV and the spectrum becomes "softer".

The target is a key element of the facility, as the secondary particle shower that propagates in the irradiation room is generated directly by the interaction between the primary beam and the target itself. The target consists of a cylinder 500 mm long with a diameter of 80 mm. To achieve several different radiation environments, three different targets are available: a copper target (labelled Cu) and two aluminum targets with different densities (labelled Al and AlH). The effective density of the

AlH target is reduced by alternating empty and bulky aluminium slices to assemble the cylinder. The three targets are mounted on a revolver that can be remotely controlled, allowing to switch target during the irradiation. In a first approximation, by changing the target it is possible to modulate the intensity of the radiation field over the room: the higher the density, the higher the number of particles laterally scattered, and consequently the dose rate and the fluxes.

The shielding consists of four movable walls that can be remotely insert or extracted from the irradiation room, depending on the desired field composition. As can be noticed by observing Figure 61, the shielding can be placed between the target and the lateral positions, affecting mainly the lateral positions. The interaction between the particle shower emitted from the target and the shielding reduces the flux of charged hadrons and increases the quantity of neutrons: the dose rate and the high energy hadron flux will be reduced, whereas the so-called R-factor[4] will increases. On the other hand, the effect of shielding on the position downstream the beam will be negligible.

To compare the LHC's spectra with the ones reproduced at CHARM, one can consider the normalized reverse integral of the high energy hadron fluence, which is obtained by integrating the HEH spectrum of the considered radiation field, and normalizing it from 1 to 20 MeV. In Figure 62, some typical environments of the LHC are compared with the spectra obtained at CHARM for some specific configurations and positions.

[4] The R-factor is defined as: $R = {\Phi_{ThN}}/{\Phi_{HEH}}$ [73]. It is an important parameter to characterize the radiation field as it expresses the amount of thermal neutrons with respect to the high energy hadrons, which is helpful to properly consider the operation of thermal neutron sensitive devices, such as old components using Borophosphosilicate glass (BPSG) to cover the chip, or in scaled technologies using boron ^{10}B as doping element. Indeed, since boron has a high thermal neutron capture cross section (3848 barns [9]), thermal neutrons can easly induce SEEs when it is absorbed by ^{10}B.

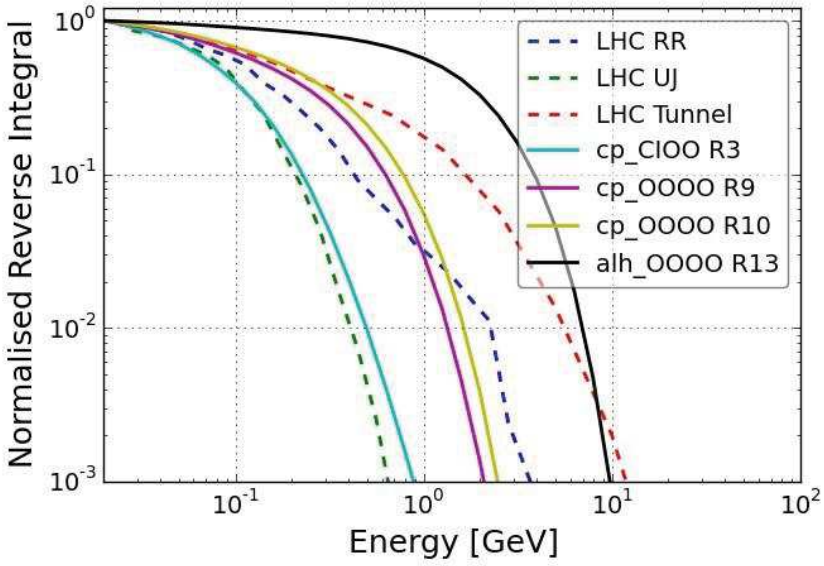

Figure 62. A plot of the reverse integral spectra for test positions at CHARM (in grey), compared with different radiation environments, normalised to 20 MeV. (source: [74]). In the legend, the last part of the labels indicates the CHARM configuration.

5.1.1 Facility Calibration and K-factor

In general, the complexity of the systems irradiated as well as the TID reached during an irradiation run do not allow the deployment of the number of RadMon systems necessary to fully characterize the radiation field permeating the test area. In normal conditions, the irradiation run at CHARM lasts a week, during which the fluence and dose targets are met by choosing the test position and the facility configuration accordingly. In view of the High Luminosity upgrade for the LHC [75], the radiation hard assurance requires the increase of the dose levels that the electronic equipment needs to withstand [76]. Consequently, it is not rare that the dose targets are higher than the TID-lifetime for the RadMon system, which is 250 Gy. For this reason, a different approach is necessary to characterize the radiation environment. Relying on the assumption that the physical quantities used to characterize the radiation field (namely the dose and the fluences) are proportional to the integrated intensity of the beam, it is possible to determine the dose and the fluences by knowing the number of proton impinging on the target and the calibration factor, as follows:

$$\begin{cases} Dose = k_{Dose} \times POT \\ \Phi_{HEH} = k_{HEH} \times POT \\ \Phi_{ThN} = k_{ThN} \times POT \\ \Phi_{1MeV} = k_{1MeV} \times POT \end{cases}$$

Equation 5.1.

where POT is the number of proton impinging on the target, whereas k_{Dose}, k_{HEH}, k_{ThN} and k_{1MeV} are respectively the calibration factors for the Dose, the High Energy Hadron fluence, the Thermal Neutron Fluence and the 1-MeV equivalent neutron fluence. These parameters are measured by means of the RadMon system for each position and configuration during the commissioning phase of the facility that occurs every year after the Year End Technical Stop (shortly YETS), according to the accelerator schedule.

It is important to note that the calibration factors depend on the test position and the facility configuration (i.e. the target material and the shielding position). The dose calibration factor k_{Dose} can be seen as the dose normalized by the beam intensity and it expresses the dose produced by a single proton hitting the target. The same reasoning applies to the calibration factor defined for the fluences, hence k_{HEH}, k_{ThN} and k_{1MeV}. According to the configuration of the shielding and the type of target used, every position of the irradiation room can be characterized in terms of dose and fluences through the ratio between measured dose (or fluences) and the POT.

The measurement of the calibration factor can be a helpful technique to characterize the radiation environment along the accelerator, as well as in the shielded areas, where the dose rate is extremely low. The calibration factor for the accelerator can be calculated as the ratio between the dose measured at the considered location and the cumulated beam intensity. However, as it will be shown, a certain amount of dose needs to be cumulated to properly measure the calibration factor. This quantity strongly depends on the sensitivity of the dosimeter employed. Consequently, in locations where the cumulated dose is low, an high-sensitive radiation dosimeter is necessary to measure the calibration factor over a reasonable period of time.

In this concern, it is important to consider that the measurement of the k_{Dose} factor is performed by evaluating the ratio of two cumulative physical quantities (the POT and the dose measured by the RADFET) and, since both of them are generally affected by noise and the dosimeter resolution is physically limited, a certain amount of time is needed to cumulate enough data for achieving an acceptable stabilization of the k_{Dose} value. As a consequence, the rate of stabilization increases with the sensitivity of the instrument employed to detect the TID. As will be shown, the resolution plays a central role throughout measurements of the k_{Dose} factor.

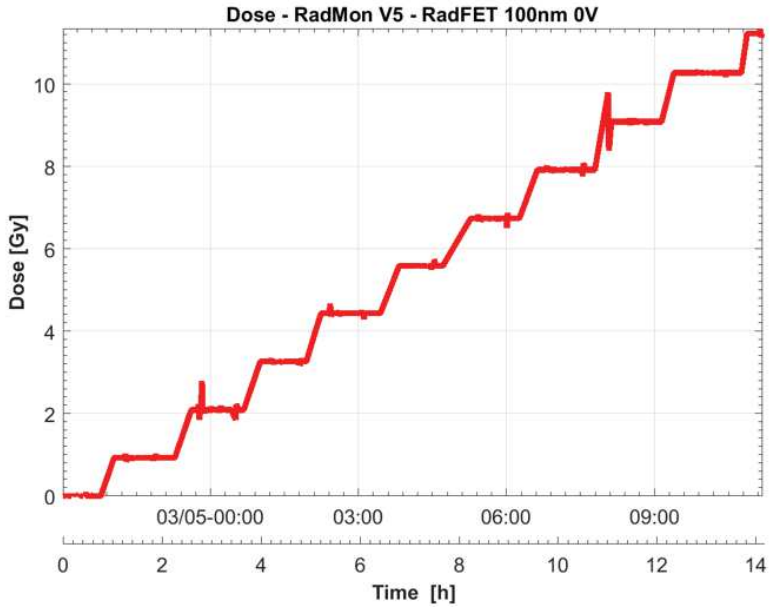

Figure 63. Dose measurement performed by the RadMon V5 (old version) at CHARM in position 10, with Aluminum target and shielding out.

To have an idea of the influence of the resolution on the measurement of the calibration factor and, more specifically, on its stabilization, the measurement of k_{Dose} was performed by using an old version of the RadMon [13] with a 100nm RADFET biased to 0V: due to the fewer bits available of the ADC embedded in this RadMon's version, this setup has a relatively poor resolution of 1 Gy. The facilty configuration during this experiment induced a field whose dose rate was about 0.7 Gy/h at the test location. In Figure 63, the measurement of the dose is reported: the effect of the lower resolution is clearly visible as the resulting curve shows a stair-step pattern. Consequently, the measurement of the calibration factor oscillates around its real value until the cumulated dose does not become significantly larger than the dose resolution, as can be seen in Figure 64.

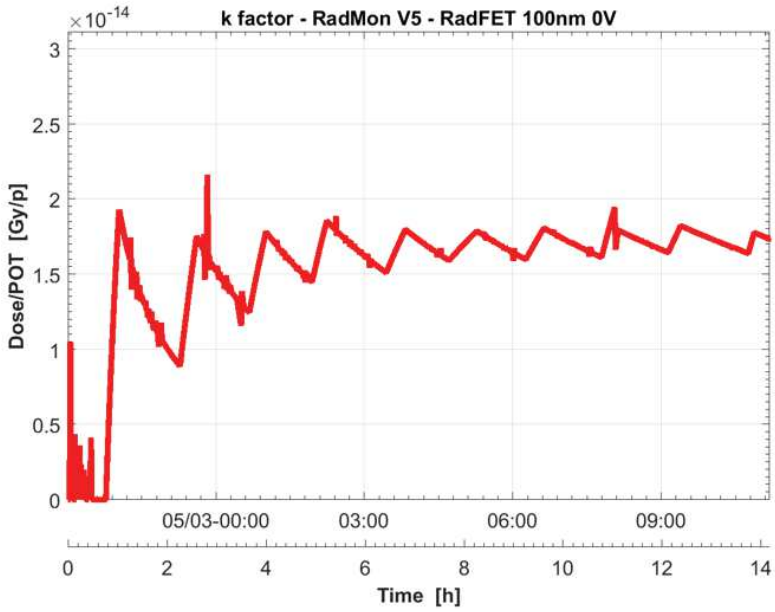

Figure 64. k_{Dose} measurement performed by the RadMon V5 (old version) at CHARM in position 10, with Aluminium target and shielding out.

5.2 FGDOS and RADFET

The FGDOS and the RADFET have been irradiated together for three different configuration of the facility. During the experiment, four FGDOS were controlled and read online during the irradiations, by means of the TIDMON board. The spread among doses measured by each sensor falls within the 2% of the mean value. Therefore, only one of the sensors is considered to show the results of the experiments. Two 100 nm RADFETs were installed next to the FGDOS in order to compare the measured dose and the calibration factor. The RADFETs were read online by means of the RadMon. The gate of the RADFET was biased to 0V and +5V, which leads to a sensitivity of 2.1 and 7.9 mV/Gy, respectively. As discussed in 0, the resolution is 212 and 57 mGy respectively for the sensor biased to 0V and +5V. The FGDOS radiation response has been drawn by considering the sensitivity achieved through the irradiation performed with a γ-ray source, whereas the RADFET radiation responses have been traced by means of the calibration curves obtained by γ-ray irradiations and verified by a 230 MeV proton beam [36]. Of course, the RADFET requires a specific calibration curve depending on the bias applied to its gate.

The test location and the facility configuration for the experiments were chosen to emulate the radiation environment where the dose might be too low to be detected by the RADFET. The sensors were placed in position 1 (see Figure 61), and the shielding were parked inside the facility. Three different runs were performed by using the three targets available.

Figure 65 presents the dose response of the FGDOS and the RADFET as function of the cumulated POT, while the copper target was used. However, similar results have been obtained by the experiments performed with the aluminium targets and are summarized in Table 7. As can be seen, the cumulated dose measured by the three sensors is comparable, although the response of the RADFETs is noisier, especially for the one biased to 0V. The sensitivity of the FGDOS and the RadFET cannot be directly compared, as the nature of their output signals is different. However, comparing the two RadFETs biased at different voltages, whose output is affected by the same electronic noise, it can be noticed that the higher the sensitivity of the RadFET biased at 5 V leads to a lower noise on the dose measurement. This is due to the higher signal-to-noise ratio that can be obtained by the more sensitive RadFET. The same consideration can be applied to the FGDOS sensor: due to its working principle, this sensor is more sensitive to ionizing radiation than the RadFET: as pointed out in 0 and Chapter 3, the dose resolution for the FGDOS is 160 µGy, whereas for the RadFETs biased at 0 V and 5 V is respectively 212 and 60 mGy. A zoom of Figure 65 is reported in Figure 66 to highlight how the higher resolution of the FGDOS allows for a much more accurate measurement for low doses. On the top of these plots, the time is reported to have an idea on dose rate received at the test location, although it is important to consider that the intensity of the beam is not constant over the time, and therefore the relationship between time and POT is not proportional: consequently, the curves are plotted against the cumulated POT.

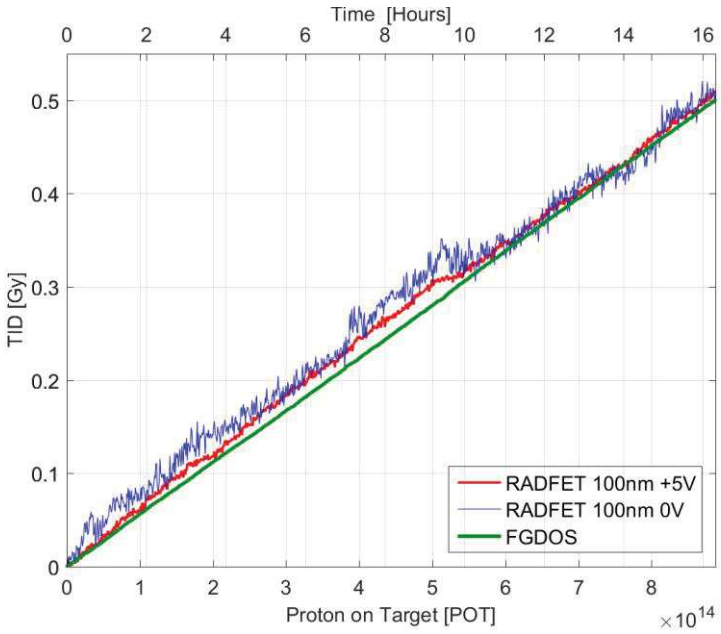

Figure 65. Dose measured by RADFETs (biased to 0V and +5V) and FGDOS. The irradiation was performed in position 1 of the irradiation room, while the mixed field was generated by the interaction between the 24 GeV proton beam and a copper target, labeled as Cu. The movable shielding was parked inside the irradiation room.

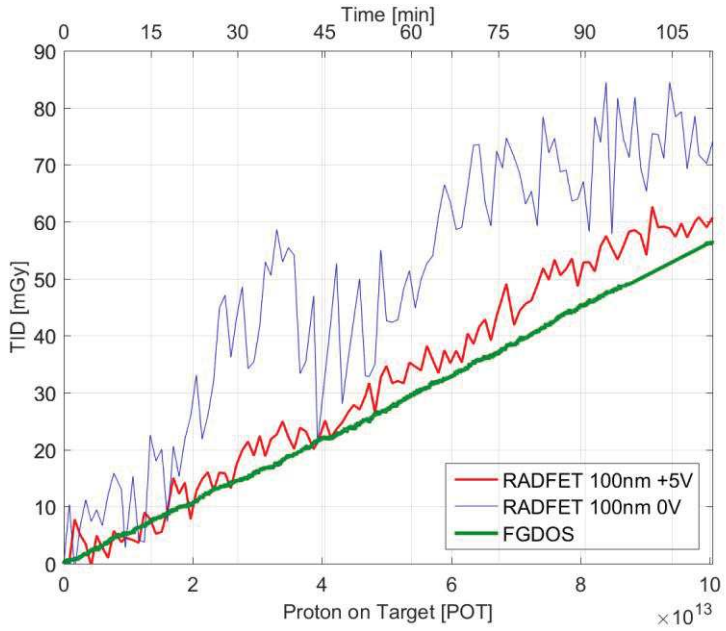

Figure 66. A zoom of Figure 65 is reported to show the influence of the resolution on the measurement for low dose levels

In Figure 67, the comparison of the k_{Dose} measurements performed by FGDOS and RADFETs is shown, whereas a zoom of the same plot is shown in Figure 68. The same comparison is summarised in Table 7: for each run, the calibration factor has been measured by the RADFETs and the FGDOS. The values measured by RADFETs are in agreement with the one measured by the FGDOS in every run. The maximum spread between the FGDOS k_{Dose} and RADFET k_{Dose} is within the 11%, both for biased and unbiased RADFET. It is important to notice that the spread depends on the run: the variation of the radiation field affects the response of the dosimeters, although, without any other references of dose measurement, it is not possible to state either the magnitude of this effect, or which sensor is effectively influenced by the field change. According to the TID measured by the FGDOS, the dose rate was 36.7, 48.8 and 27.6 mGy/h respectively for the Cu, Al and AlH runs. During the run with the Cu target, the dose rate was lower than the one got during Al run, despite the higher density of the Cu target. This is due to the lower intensity of the beam delivered during the Cu run.

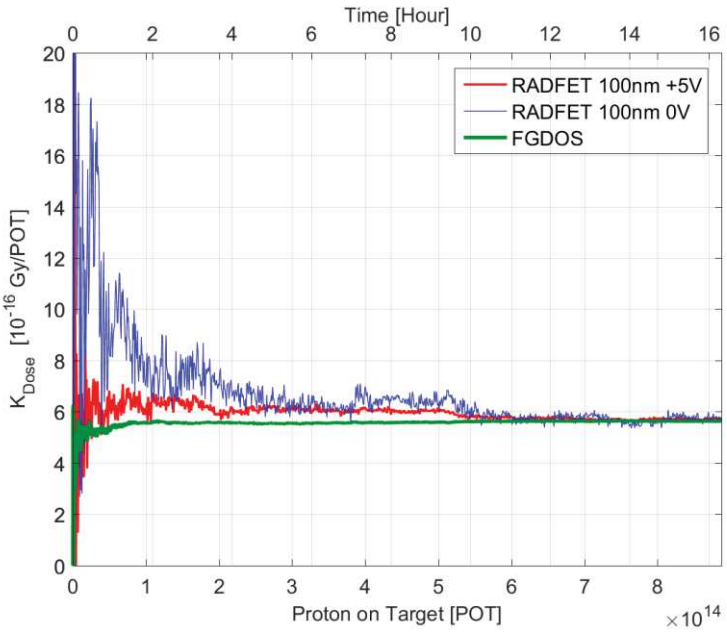

Figure 67. k_{Dose} factor measurements in position 1, copper target and all the movable shielding placed inside the irradiation room.

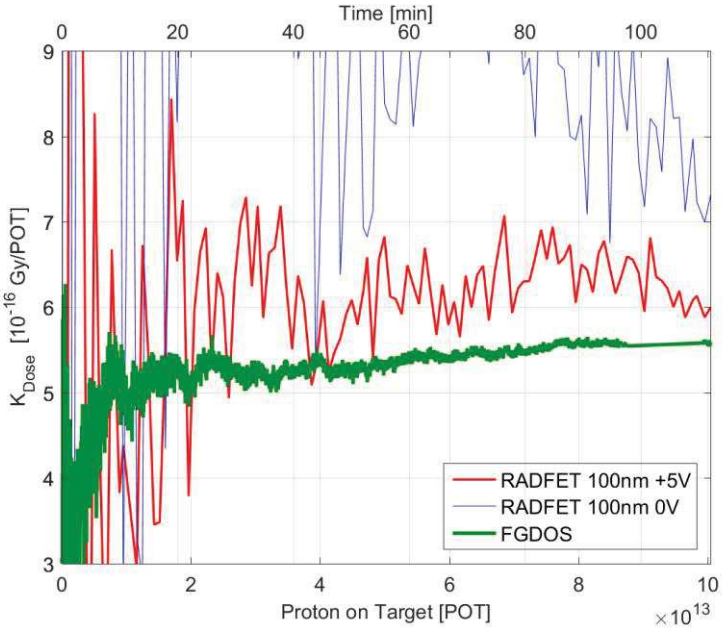

Figure 68. Blow up of the irradiation shown in Figure 67, emphasizing the influence of the resolution on the measurement for low dose levels.

The oscillations of the k_{Dose} around its final value are dumped as a result of the increase of the shift of the dosimeter output signal. Because of its higher sensitivity, the oscillations of the RADFET biased to +5V are dumped faster than the ones of the unbiased RADFET. The output signals of RADFET and FGDOS sensors are not comparable because of their different nature, as well as their sensitivity. Nevertheless, by observing Figure 67 and Figure 68 , it is clear that the stabilization of the k_{Dose}, within the

same run, is faster for the FGDOS compared with the RADFETs, and this is due to the higher resolution.

To be able to compare different runs, the variable to be considered is the cumulated POT, rather than time. Aiming at quantifying the velocity of the k_{Dose} factor stabilization, the cumulated POT is evaluated as soon as the k_{Dose} factor oscillation becomes lower than ±5% of its final value.

The cumulated POT, the dose, and the time needed to dump the oscillations within the ±5% of the final value are respectively named $POT_{\pm5\%}$, $\Delta D_{\pm5\%}$ and $\Delta T_{\pm5\%}$. In Table 7, these quantities are compared for each run. The amount of POT necessary to achieve the k_{Dose} factor stabilization is extremely low for the FGDOS: from 9 to 20 times lower than the RADFET biased to +5V and from 14 to 50 for the unbiased RADFET. The dose to be cumulated is computed by multiplying the calibration factor by the $POT_{\pm5\%}$, whereas the $\Delta T_{\pm5\%}$ is computed by considering the amount of proton impinging on the target on average, i.e. $1 \cdot 10^{+15}$ POT/day. The latter gives a general idea about the time needed to obtain the stabilization of the calibration factor, without keeping into account any change of the intensity. On the other hand, both $POT_{\pm5\%}$ and $\Delta D_{\pm5\%}$ are specific information which are valid for any run, irrespective of the beam intensity.

As can be observed in Table 7, in the best-case scenario, the measurement performed by means of FGDOS allows to achieve the k_{Dose} factor by cumulating an amount of dose that is about eight times lower than the dose needed by using the RADFET biased to +5V. This would lead to a significant improvement of the TID monitoring along the LHC and its injection lines. Taking the integrated number of collisions in the LHC experiments (integrated luminosity) as scaling factor, it is possible to compare the integrated luminosity needed to reach a stable calibration factor for both FGDOS and RADFETs. For instance, during 2016, the cumulated dose measured by the Beam Loss Monitor (BLM) in the LHC Arcs was on average ~300 mGy, for an integrated luminosity of the LHC of about 33 fb^{-1}. Considering the comparison presented in Table 7, the integrated luminosity needed to achieve a calibration factor would be: ~4 fb^{-1} by performing the measurement through FGDOS; 33 fb^{-1} by performing the measurement through RADFET biased to +5V; ~50 fb^{-1} by performing the measurement through unbiased RADFET.

TABLE VII
SUMMARY OF CALIBRATION FACTOR K_{DOSE} MEASUREMENT

TARGET	DOSIMETER	K_{DOSE} [GY/POT]	$POT_{\pm5\%}$ [POT]	$\Delta D_{\pm5\%}$ [GY]	$\Delta T_{\pm5\%}$ [H]
CU	FGDOS	$5.63 \cdot 10^{-14}$	$0.61 \cdot 10^{+14}$	3.5	1.5
	RADFET +5V	$5.73 \cdot 10^{-14}$	$5.15 \cdot 10^{+14}$	30	12
	RADFET 0V	$5.74 \cdot 10^{-14}$	$8.15 \cdot 10^{+14}$	47	20
AL	FGDOS	$3.20 \cdot 10^{-14}$	$0.66 \cdot 10^{+14}$	2.1	1.6
	RADFET +5V	$2.97 \cdot 10^{-14}$	$8.20 \cdot 10^{+14}$	25	20
	RADFET 0V	$2.85 \cdot 10^{-14}$	$31.1 \cdot 10^{+14}$	89	75
ALH	FGDOS	$1.86 \cdot 10^{-14}$	$1.20 \cdot 10^{+14}$	2.3	3
	RADFET +5V	$1.65 \cdot 10^{-14}$	$27.3 \cdot 10^{+14}$	45	65
	RADFET 0V	$1.84 \cdot 10^{-14}$	$37.1 \cdot 10^{+14}$	68	90

Table 7. k_{Dose} factor measurement performed by the FGDOS and RadFETs unbiased and biased to +5V. The $POT_{\pm5\%}$ indicates the POT to be cumulated to achieve k_{Dose} oscillations lower than ±5% of the final value. $\Delta D_{\pm5\%}$ and $\Delta T_{\pm5\%}$ indicates the dose time needed to achieve k_{Dose} oscillations lower than ±5% of the final value.

5.3 NMOS and RADFET

Since the sensitivity of the NMOS is similar to the one obtained by the RADFET biased to 5V, the comparison of the measurements of the dose calibration factor performed by means of the two sensors would not provide significant results in terms of $\Delta D_{\pm5\%}$. However, it is crucial to establish whether the radiation response of the two sensors is comparable. For this reason, the consistency of the dose measurements performed by the NMOS has been evaluated by comparing the results with the dose detected by the 100nm RADFETs, while the sensors were exposed to the CHARM's mixed field. Irradiation tests were performed to investigate both the passive and the active measurements. During the active measurement, the sensors were read online by the RadMon system, as described in Section 2.2. On the contrary, the passive measurement is performed by reading the voltage before and after the irradiation. The voltage shift is therefore converted into dose by means of the calibration curve of the sensor retrieved in Section2.4.

5.3.1 Active Measurements

At CHARM, ten RadMons are employed to provide the users with the radiation levels received by their setup in terms of High Energy Hadron fluence (HEH), Thermal Neutron fluence (ThN), 1MeV equivalent Neutron fluence (1-MeVeq) and Total Ionizing Dose. As described in Section 1.4, each RadMon can host on its deported module two TID sensors, which are read at the same time.

In normal conditions, the dose provided to the users is measured by means of the RADFET biased at +5V. Taking advantage of this setup configuration, it was possible to carry out several comparisons while measuring the dose levels for the users, by equipping the deported module with one RADFET and one NMOS.

Even though some measurements were performed multiple times in the same position, they cannot be compared to each other because the beam intensity and the effective irradiation time changes from run to run. Moreover, each deported module might be shielded in a different way depending on the user's setup. Therefore, the comparison must be done by evaluating the NMOS and the RadFET read by the same RadMon during the same irradiation run. In Figure 14, the dose measured during four different runs in four different positions is plotted as an example.

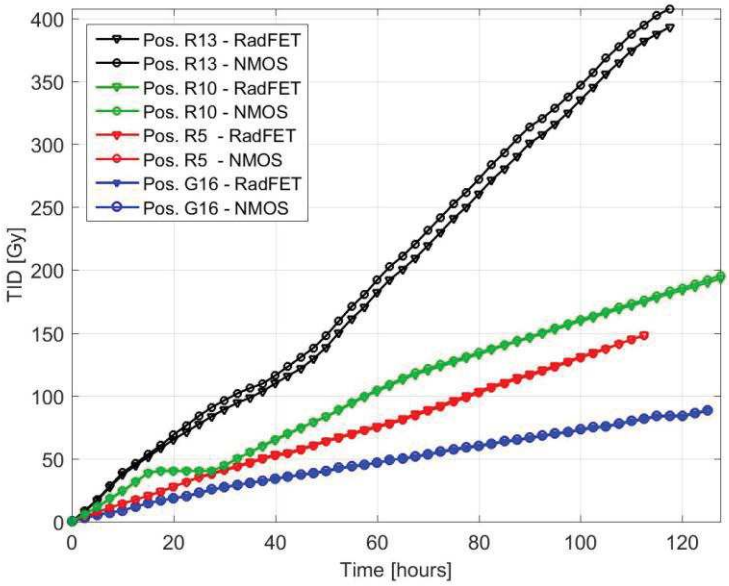

Figure 69. Response of the sensors is compared for three different positions (13, 10, 5 and 16). The measurements were performed during four different runs.

The comparison of all the irradiation runs from April 2018 to May 2018 is reported in Table 1, where the dose measured by each sensor pair is detailed. In the last column, the difference between the RADFET and the NMOS measurement is reported. This quantity has been calculated by the formula:

$$\Delta_{\%} = 100 \times \frac{Dose_{RadFET} - Dose_{NMOS}}{Dose_{RadFET}}$$

As can be observed, the maximum variation obtained is ~16%. However, only for three measurements over 18 the variation is larger than 10% and the mean of the error is -3.4%.

TABLE VIII
SUMMARY OF ACTIVE MEASUREMENTS

Position	RADFET [Gy]	NMOS [Gy]	$\Delta_{\%}$ [%]
R13	395.0	409.7	-3.72
	459.5	534.4	-16.29
	409.9	438.5	-6.97
	356.9	370.5	-3.83
R10	183.2	174.2	4.93
	193.8	196.3	-1.30
	183.5	192.3	-4.79
	183.1	201.3	-9.99
	156.2	147.2	5.79
	165.9	175.0	-5.48
	155.9	172.5	-10.59
	156.6	182.4	-16.53
	164.1	174.5	-6.32
	169.2	157.9	6.72
P5	150.3	150.1	0.14
G16	90.1	90.8	-0.72
G18	2.8	2.7	3.04
G17	1.6	1.6	4.82

Table 8. Comparison of the active measurement performed at CHARM during the irradiation runs.

5.3.2 Repeatability

The repeatability of the measurement performed by the NMOS has been investigated by irradiating seven different NMOS and one RADFET +5V in the same conditions. The sensors were placed in position 5 (see Figure 61) and read by four RadMons, simultaneously. InFigure 69, the resulting curves of the experiment are plotted. As can be seen, the sensors behaved similarly and the spread among the measured doses is relatively small. In Table 9, the summary of the irradiation results is reported.

TABLE IX
SUMMARY OF REPEATIBILITY MEASUREMENTS

Position	Sensor	# of samples	μ[Gy]	σ_{rel} [%]	Max err_{rel} [%]
R5	NMOS	7	150.0	2.5	-5.9
	RADFET	1	150.1	-	-

Table 9. Comparison between the measurements performed by the RADFET +5V and seven NMOS

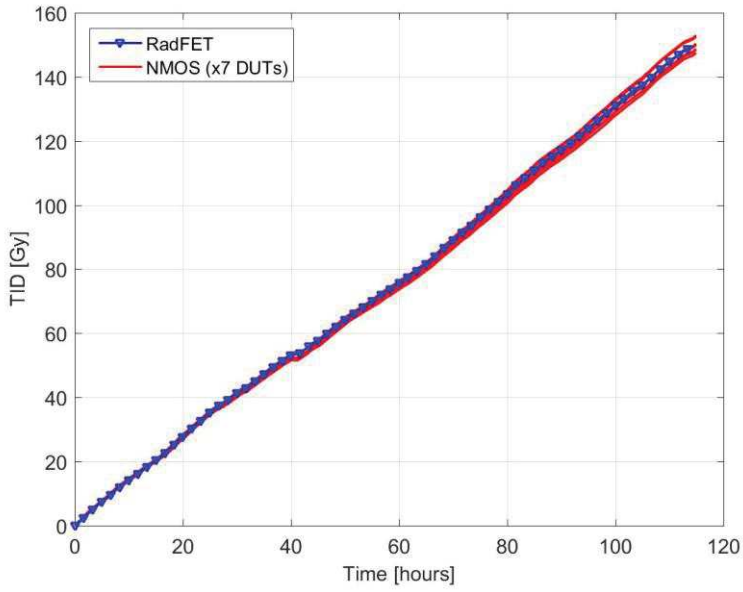

Figure 70. Irradiation test in position 5. The dose measured by the RADFET +5V is compared with the dose measured by seven different NMOS transistors.

5.3.3 Passive Measurements

The consistency of the measurements performed in passive mode has been investigate by irradiating two bunches of passive sensors, made of ten NMOS and one RADFET each, in two different positions (5 and 13). During the irradiation, all the pins of the sensors were shorted.

This experiment was performed at the same time of the repeatability test discussed in the previous section: in this way, it would have been possible to compare the passive measurements with the active sensors placed in position 5, i.e. seven NMOS and one RADFET +5V. Unfortunately, only one deported module equipped with two NMOS was placed in position 13, whereas no RADFETs were available.

In Table 10, the comparison of the measurements is reported. The quantities named as Δ_{MAX} and Δ_{MIN} indicate respectively the maximum and minimum variation with respect to the mean value μ. The difference between the passive measurements performed with the NMOS and RADFET has been evaluated as follows:

$$\Delta D1\ [\%] = \frac{\mu_{RadFET} - \mu_{NMOS}}{\mu_{RadFET}}$$

The mismatch between the passive and active measurement is labelled *ΔD2* and is calculated as the percentage difference between the two measurements with respect to the active one. In formula:

$$\Delta D2\ [\%] = \frac{\mu_{NMOS(Passive)} - \mu_{NMOS\ (Active)}}{\mu_{NMOS(Passive)}}$$

As can be observed, the variability of the passive NMOS is slightly larger than the one obtained with the active NMOS, although it is still acceptable for the application. This mismatch is confirmed by the comparison with the active measurements, reported in the last column.

On the other hand, the comparison between the passive measurements shows a significant difference between the NMOS and the RADFETs, which is confirmed in both the positions. This mismatch might be due to the calibration curve of the RADFET, which is different from the curve used to convert the voltage shift into dose during the active measurement. In fact, as mentioned above, the RADFET is biased to +5V during the active reading at CHARM. Of course, when the sensor is used in passive mode, no supply is applied to its gate (all the pins are shorted with each other). Consequently, the calibration curve used for the passive RADFETs was obtained by irradiating the sensor while connecting the gate to ground. Two causes can bring to this effect: i) the calibration curve of the RADFET at 0V introduces an error or ii) the calibration curves for the RADFET used in passive and active mode are different from each other. However, considering that the reading operation implemented by the RadMon (and described in Section 2.2) affects the bias of the sensor only for 100 ms over 2 s, i.e. for 5% of the time, the difference between the active and passive calibration curve should be negligible.

TABLE X
SUMMARY OF PASSIVE MEASUREMENTS

Position	Mode	Sensor	# of samples	μ[Gy]	Δ_{MAX} [%]	Δ_{MIN} [%]	ΔDose1[%]	ΔDose2[%]
R5	Passive	NMOS	10	146.7	2.5	-5.9	12.1	-1.4
		RadFET	1	167.0	-	-		
	Active	NMOS	7	148.9	2.4	-2.8	1.0	
		RadFET	1	150.3	-	-		
R13	Passive	NMOS	10	489.5	4.3	-6.5	13.4	7.1
		RadFET	1	565.5	-	-		
	Active	NMOS	2	455.1	3.6	-3.6	-	
		RadFET	-	-	-	-		

Table 10. Comparison of the passive measurements performed at CHARM.

The hypothesis that the source of the mismatch lies in the measurement of the passive RADFET is confirmed by the comparison between the active and passive RADFETs placed in position R5, whose difference is ~11%. The same consideration can be applied by comparing the active NMOS with the passive RADFET placed in position R13. In this case, the difference results ~2%.

5.4 Conlusions

In this chapter, the radiation response to mixed radiation field environment of the FGDOS and the NMOS has been investigated and compared with the RADFET's one.

The analysis of the FGDOS response has been focused on the measurement of the calibration factor and on the cumulated dose necessary to obtain a stable value. The results of the study highligth how the high sensitivity and resolution of the FGDOS leads to a substantial improvement in terms of TID measurement in mixed radiation fields with respect to the RADFET. This aspect has been verified at CHARM, where it was possible to evaluate both the calibration factor of the facility and the amount of POT to be cumulated in order to obtain a stable k_{Dose}. In Table 7, the k_{Dose} and the $POT_{\pm 5\%}$ are reported. The spread among calibration factors resulted within the 11% with respect to the one measured by the FGDOS. The $POT_{\pm 5\%}$ allows to estimate the time needed to obtain the k_{Dose} stabilization, assuming an average beam intensity of $1 \cdot 10^{+15}$ POT/day: to obtain the same accuracy, the RADFETs

are required to integrate the dose for periods of time from 8 to 50 times larger than the FGDOS. In the LHC context, the higher resolution would allow to measure the TID where the dose level is too low to be detected by RADFETs. Moreover, calibration factors could be retrieved with a much lower integrated number of collisions from the hadron collider.

As well as for the FGDOS, the behaviour of the DMN601 NMOS transistor in the accelerator-like mixed radiation environment has been investigated by performing accelerated radiation tests at the CHARM facility. During the irradiation runs of the facility performed from April to May 2018, the exposure of 18 pairs (NMOS, RADFET +5V) read in active mode have been analysed (see Table 8). The maximum variation observed on the measured dose was ~-16%, whereas the average error was ~-3.4%. Considering that the uncertainty of the RADFET in the mixed field assessed in [77] is ±25%, the results of the comparison of the active measurements are consistent with this variability.

The repeatability of the measurement has been investigated by irradiating seven NMOS and one RADFET biased to +5V, which were read by using four different RadMons during the same run. The spread among the NMOS radiation responses is within the 6%, whereas the average curve of the doses the NMOS sensors overlaps the RADFET one.

The consistency of the measurements performed in passive mode has been verified by comparing the results of the passive NMOS with active and passive RADFETs. The experiments show that the NMOS measurements performed in passive mode are consistent with the dose measured both by the active NMOS and the active RADFETs. On the other hand, the passive measurements performed by the RADFETs resulted ~12% higher than the NMOS measurements. The source of this mismatch shall be investigated by verifying that the calibration curve of the RADFET biased to 0V is suitable for the measurements in passive mode.

Chapter 6 Conclusions

Aiming to improve the monitoring of the Total Ionizing Dose along the CERN's accelerator complex, two silicon dosimeters have been investigated to demonstrate their suitability as TID detector for accelerator-like environments. The sensors have been selected following two criteria: (i) cost containment and (ii) improvement of the TID measurement in terms of resolution and flexibility of the monitoring system.

The commercial component selected to accomplish the first criteria is the NMOS transistor DMN601k, whose radiation response has been fully characterized by exposing the device to gamma radiation at the CC60 facility at CERN. The sensitivity as a function of the dose has been discussed, as well as the error introduced by the sample-to-sample and batch-to-batch variation. The dose resolution results comparable to the one obtained by the RADFET, although its measurable dose range is limited to 550 Gy (which is still acceptable for most of the measurement requirements of CERN radiation environment). The dose range is not limited by the intrinsic characteristic of the device, but rather by the dynamic range of the reading circuit employed. Indeed, to further contain costs and avoid the development of dedicated radiation tolerant monitoring systems, minor modifications of the reading circuit embedded on the RadMon system were necessary to adapt the circuit, conceived to measure the V_{th} shift of the RADFET, for the NMOS transistor.

The suitability of the NMOS as TID detector in mixed radiation fields has been demonstrated by performing several radiation tests at the CHARM facility, and by operating the sensor both in active and passive mode. The consistency of the measurements performed in active mode has been verified by comparing the output of the measurements performed by the NMOS and the RADFET biased at +5V: the maximum error observed (~-16%) was significantly lower than the error that must be considered by using the RADFET in mixed radiation fields (±25%). Finally, the use of the NMOS operating in passive mode has been investigated: the experiments showed that the NMOS passive measurements are consistent with the dose measured both by the active NMOS and the active RADFETs. The dose measured by the RADFETs operating in passive mode was found to be ~12% higher than the NMOS measurements. The cause of this discrepancy will be investigated by verifying the suitability of the calibration curve of the RADFET biased to 0V for passive measurements. The qualification of the NMOS in

passive mode is extremely important as it would allow the deployment of a large number of dosimeters in order to obtain a detailed dose map for large distributed facilities, such as the LHC.

Furthermore, the temperature sensitivity of the sensor has been characterized in order to remove the effect of the temperature on the NMOS output, which might lead to significant errors in the measurements, especially for low doses.

The research for improving the quality of the TID monitoring performed along the accelerator chain led us to consider the FGDOS as a suitable candidate. As extensively discussed, the radiation sensitive circuit, based on a standalone floating gate structure, makes the device extremely sensitive to TID, leading to a resolution of 160 μGy: two orders of magnitude lower than the one obtained by the 100nm RADFET biased to +5V, which is 60 mGy.

The behaviour of the sensor has been fully characterized. The variability of the radiation response considering samples belonging to the same batch and samples belonging to different batches has been estimated. The spread due to sample-to-sample variability is extremely low (2.9%), whereas, for sensors belonging to different batches, the spread is 10%.

Being the FGDOS a System-On-Chip whose degree of autonomy changes depending on the configuration and operational mode used, a detailed characterization of all the possible configurations has been carried out. In particular, two operational modes (called Passive and Autonomous Mode) have been developed and characterized. For the Passive Mode, two different methods to measure the dose have been discussed: (i) by exploiting the full characteristic of the sensor and (ii) by approximating the response curve with a straight line. The error made by using the calibration curve was found to be very low both for the HS and LS configuration. The measurements made by the linear approximation were in good agreement with the absorbed dose when the sensor works in HS configuration. On the contrary, the LS configuration showed a significant discrepancy between the measurements, due to the non-optimal choice of the linear range. In this concern, the linear range should be shifted where the sensitivity does not change so dramatically. However, to correctly implement this change, the biasing of the radiation sensitive circuit and the temperature sensitive circuit must be modified in the next release of the sensor. This study has also a direct impact on the Autonomous Mode as the choice of the linear range would affect the recharge rate and, as a consequence, the dose error.

The functioning of the Autonomous Mode has been successfully demonstrated and characterized by performing several radiation tests. The sensor can autonomously control the recharge process and provide the data whenever it is interrogated. The accuracy of the measurement by using Equation

3.10 requires that (i) the recharge time is negligible with respect to the discharge time, and (ii) the sensitivity does not change with the dose. The error introduced by the finite recharge time can be drastically reduced by applying the high voltage externally. However, the use of the internal recharge circuitry requires the re-design of the charge pump chain to minimize the error. The re-design is currently in progress. Concerning the sensitivity, the irradiation test presented in Section 3.6.2 highlights that its degradation plays a crucial role in the measurement of the dose, introducing a significant error that might invalidate the dose measurement. As a consequence, it became important to understand the mechanisms behind the degradation of the sensitivity. In this concern, a test chip embedding the radiation sensitive circuit structures was provided by IC-Malaga. Several experiments have been carried out by exposing the test chips to gamma radiation with the aim to investigate the degradation of the floating gate capacitor and the reading transistor composing the radiation sensitive circuit. This study allowed the separation of two main mechanisms impacting the sensitivity of the FGDOS. On the one hand, the shift of the characteristic of the reading transistor due to a leakage current appears to affect both the transconductance of the transistor and the sensitivity of the capacitor. This phenomenon can be easily avoided by designing a radiation hardened transistor with an enclosed layout, to avoid any possible leakage path and the change in the working point of the sensor. The enclosed transistor tested in Chapter 4 has been already implemented in the design of the next release of the sensor. On the other hand, the analysis on the capacitor sensitivity showed that its degradation depends essentially on the electric field across the capacitor and on the quality of the field oxide. The former directly affects the degradation rate and can be reduced by using the sensor in the Lower Working Point region. The latter is strictly related with the fabrication process, which cannot be improved for economic reasons. To overcome this drawback, possible compensation methods are currently under study. The sensitivity degradation can be compensated for by shifting the characteristic of the reading transistor to push its working point towards higher *gm*, which would compensate for the lowering of the capacitor sensitivity. The parallel current can be easily generated integrating an NMOS transistor in parallel to the one used to read the floating gate capacitor. The voltage gate of the parallel transistor should be properly tuned to control the sensitivity compensation. This solution will be implemented in the next release of the sensor. An alternative compensation method can be implemented by using the injector and the floating gate capacitor as a capacitive voltage divider. In principle, the decrease of the electric field can be compensated for by applying a specific voltage on the injector, which will be divided between the injector and the capacitor. Of course, this voltage has to be calculated according to the degradation of the sensor and the transistor working point. In addition, it must be lower than the injection threshold.

Finally, the radiation response of the FGDOS in the mixed radiation field environment of the CHARM facility has been investigated and compared with the RADFET's one. In particular, the measurement of the calibration factor and the cumulated dose necessary to obtain a stable value have been evaluated for the two sensors. The results of the investigation point out how the high sensitivity of the FGDOS leads to a substantial improvement in terms of TID measurements in mixed radiation fields with respect to the RADFET. The spread among calibration factors fell within the 11% with respect to the one measured by the FGDOS. The amount of POT to be cumulated to obtain a stable k_{Dose} ($POT_{\pm 5\%}$), assuming an average beam intensity of $1 \cdot 10^{+15}$ POT/day, was found to be much higher for the RADFET: to obtain the same accuracy, the RADFETs need to integrate the dose for periods of time from 8 to 50 times larger than the FGDOS. In the LHC context, the higher sensitivity of the FGDOS would allow to measure the TID where the dose level is too low to be detected by RADFETs. Furthermore, calibration factors could be retrieved with a much lower integrated number of collisions from the hadron collider.

Acknowledgments

This work would not have been possible without the help of many persons that I would like to thank. Firstly, I am thankful to my CERN's supervisor Salvatore Danzeca for guiding me in this exciting and tortuous path. It has been an honour to be his first PhD student.

My truthful gratitude goes to my university supervisor Professor Laurent Dusseau, whose precious advices helped me to understand the mechanisms ruling radiation effects in electronics.

I am also grateful to Professor Lodovico Ratti and Professor Sylvain Girard, who deeply reviewed this manuscript.

I would like to Alessandro Masi for giving me the opportunity to work in this stimulating environment.

I wish to thank all my colleagues from the EN-SMM-RME section, for their support and the stimulating discussions we had. They gave me the opportunity to grow up as a researcher and a person. Special thanks go to Georgios, Rudy, Thomas, Chiara, Giulia and Stefano for having made these years memorable.

I deeply thank Martina, who knows how to read my few words and always pushes me to give my best, no matter if they are sunny or rainy days.

Lastly, I wish to thank my family, who made me feel their love across the Alps.

Matteo

References

[1] M. Lamont, “LHC Report: intensity ramp-up – familiar demons.”

[2] “FUNDAMENTAL QUANTITIES AND UNITS FOR IONIZING RADIATION,” *J. Int. Comm. Radiat. Units Meas.*, vol. 11, no. 1, p. NP-NP, Apr. 2011.

[3] N. H. Medina *et al.*, “Experimental Setups for Single Event Effect Studies,” *J. Nucl. Phys. Mater. Sci. Radiat. Appl.*, vol. 4, no. 1, pp. 13–23, Aug. 2016.

[4] C. Leroy and P.-G. Rancoita, *Principles of Radiation Interaction in Matter and Detection*, 2nd ed. WORLD SCIENTIFIC, 2009.

[5] S. Wood *et al.*, “Simulation of Radiation Damage in Solids,” *IEEE Trans. Nucl. Sci.*, vol. 28, no. 6, pp. 4107–4112, 1981.

[6] J. R. Srour and J. W. Palko, “Displacement Damage Effects in Irradiated Semiconductor Devices,” *IEEE Trans. Nucl. Sci.*, vol. 60, no. 3, pp. 1740–1766, Jun. 2013.

[7] R. Ferraro, “CHARM RadTest - 180613 - TLP383, TLP385, TLP785, PS2502 & 4N49U Optocouplers | Document 2002403 (v.1).”

[8] C. Poivey and G. Hopkinson, “Displacement Damage, Mechanism and Effects.”

[9] H. W. Schmitt, R. C. Block, and R. L. Bailey, “Total neutron cross section of B10 in the thermal neutron energy range,” *Nucl. Phys.*, vol. 17, pp. 109–115, Jun. 1960.

[10] C.-W. Liu, B.-T. Dai, and C.-F. Yeh, “Chemical mechanical polishing of PSG and BPSG dielectric films: the effect of phosphorus and boron concentration,” *Thin Solid Films*, vol. 270, no. 1, pp. 607–611, Dec. 1995.

[11] A. Vázquez-Luque *et al.*, “Neutron Induced Single Event Upset Dependence on Bias Voltage for CMOS SRAM With BPSG,” *IEEE Trans. Nucl. Sci.*, vol. 60, no. 6, pp. 4692–4696, Dec. 2013.

[12] A. Holmes-Siedle and L. Adams, “RADFET: A review of the use of metal-oxide-silicon devices as integrating dosimeters,” *Int. J. Radiat. Appl. Instrum. Part C Radiat. Phys. Chem.*, vol. 28, no. 2, pp. 235–244, Jan. 1986.

[13] G. Spiezia *et al.*, “The LHC Radiation Monitoring System - RadMon,” *J. Proc. Sci*, p. 12.

[14] I. Mateu, M. Glaser, G. Gorine, M. Moll, G. Pezzullo, and F. Ravotti, “ReadMON: a portable readout system for the CERN PH-RADMON sensors,” *IEEE Trans. Nucl. Sci.*, pp. 1–1, 2018.

[15] R. Secondo *et al.*, “System Level Radiation Characterization of a 1U CubeSat Based on CERN Radiation Monitoring Technology,” *IEEE Trans. Nucl. Sci.*, pp. 1–1, 2018.

[16] Y. Kimoto and A. Jaksic, “RADFET utilization for spacecraft dosimetry,” in *2004 24th International Conference on Microelectronics (IEEE Cat. No.04TH8716)*, 2004, vol. 2, pp. 657–659 vol.2.

[17] R. Ferraro, T. Borel, and S. Danzeca, “CC60 Radiation Report for N-MOSFET Transistor,” Radiation Report 1609725.

[18] D. M. Fleetwood *et al.*, “Effects of oxide traps, interface traps, and ‘“border traps”’ on metal-oxide-semiconductor devices,” *J. Appl. Phys.*, vol. 73, no. 10, pp. 5058–5074, May 1993.

[19] T. R. Oldham, *Ionizing radiation effects in MOS oxides*. Singapore: World Scientific, 2000.

[20] G. A. Ausman and F. B. McLean, “Electron−hole pair creation energy in SiO_2,” *Appl. Phys. Lett.*, vol. 26, no. 4, pp. 173–175, Feb. 1975.

[21] H. H. Sander and B. L. Gregory, “Unified Model of Damage Annealing in CMOS, from Freeze-In to Transient Annealing,” *IEEE Trans. Nucl. Sci.*, vol. 22, no. 6, pp. 2157–2162, Dec. 1975.

[22] J. M. Benedetto and H. E. Boesch, “The Relationship between 60Co and 10-keV X-Ray Damage in MOS Devices,” *IEEE Trans. Nucl. Sci.*, vol. 33, no. 6, pp. 1317–1323, Dec. 1986.

[23] R. C. Hughes, “Hole mobility and transport in thin SiO_2 films,” *Appl. Phys. Lett.*, vol. 26, no. 8, pp. 436–438, Apr. 1975.

[24] G. S. Ristic, “Influence of ionizing radiation and hot carrier injection on metal-oxide-semiconductor transistors,” *J. Phys. Appl. Phys.*, vol. 41, no. 2, p. 023001, 2008.

[25] T. P. Ma and P. V. Dressendorfer, Eds., *Ionizing radiation effects in MOS devices and circuits*. New York: Wiley, 1989.

[26] F. J. Grunthaner and J. Maserjian, “CHEMICAL STRUCTURE OF THE TRANSITIONAL REGION OF THE SiO2/Si INTERFACE**This paper presents the results of one phase of research performed at the Jet Propulsion Laboratory, California Institute of Technology, sponsored by the National Aeronautics & Space Administration under Contract No. 7-100, and by the Defense Advanced Research Projects Agency through the National Bureau of Standards, Order No. 611377.,” in *The Physics of SiO2 and its Interfaces*, S. T. Pantelides, Ed. Pergamon, 1978, pp. 389–395.

[27] F. J. Grunthaner, P. J. Grunthaner, and J. Maserjian, “Radiation-Induced Defects in SiO2 as Determined with XPS,” *IEEE Trans. Nucl. Sci.*, vol. 29, no. 6, pp. 1462–1466, Dec. 1982.

[28] T. Sakurai and T. Sugano, “Theory of continuously distributed trap states at Si-SiO2 interfaces,” *J. Appl. Phys.*, vol. 52, no. 4, pp. 2889–2896, Apr. 1981.

[29] P. M. Lenahan and P. V. Dressendorfer, “Hole traps and trivalent silicon centers in metal/oxide/silicon devices,” *J. Appl. Phys.*, vol. 55, no. 10, pp. 3495–3499, May 1984.

[30] P. J. McWhorter and P. S. Winokur, “Simple technique for separating the effects of interface traps and trapped-oxide charge in metal-oxide-semiconductor transistors,” *Appl. Phys. Lett.*, vol. 48, no. 2, pp. 133–135, Jan. 1986.

[31] A.-M. El-Sayed, M. B. Watkins, T. Grasser, V. V. Afanas’ev, and A. L. Shluger, “Hydrogen-Induced Rupture of Strained Si–O Bonds in Amorphous Silicon Dioxide,” *Phys. Rev. Lett.*, vol. 114, no. 11, p. 115503, Mar. 2015.

[32] C. M. Dozier, D. B. Brown, J. L. Throckmorton, and D. I. Ma, “Defect Production in SiO2 by X-Ray and Co-60 Radiations,” *IEEE Trans. Nucl. Sci.*, vol. 32, no. 6, pp. 4363–4368, Dec. 1985.

[33] F. B. McLean, “A Framework for Understanding Radiation-Induced Interface States in SiO2 MOS Structures,” *IEEE Trans. Nucl. Sci.*, vol. 27, no. 6, pp. 1651–1657, Dec. 1980.

[34] F. W. Sexton and J. R. Schwank, “Correlation of Radiation Effects in Transistors and Integrated Circuits,” *IEEE Trans. Nucl. Sci.*, vol. 32, no. 6, pp. 3975–3981, Dec. 1985.

[35] A. E. Islam, V. D. Maheta, H. Das, S. Mahapatra, and M. A. Alam, “Mobility degradation due to interface traps in plasma oxynitride PMOS devices,” in *2008 IEEE International Reliability Physics Symposium*, 2008, pp. 87–96.

[36] G. Spiezia *et al.*, “A New RadMon Version for the LHC and its Injection Lines,” *IEEE Trans. Nucl. Sci.*, vol. 61, no. 6, pp. 3424–3431, Dec. 2014.

[37] J. R. Schwank *et al.*, “Radiation Effects in MOS Oxides,” *IEEE Trans. Nucl. Sci.*, vol. 55, no. 4, pp. 1833–1853, Aug. 2008.

[38] J. Kassabov, N. Nedev, and N. Smirnov, “Radiation dosimeter based on floating gate MOS transistor,” *Radiat. Eff. Defects Solids*, vol. 116, no. 1–2, pp. 155–158, Mar. 1991.

[39] B. L. Gregory, “Process Controls for Radiation-Hardened Aluminum Gate Bulk Silicon CMOS,” *IEEE Trans. Nucl. Sci.*, vol. 22, no. 6, pp. 2295–2302, Dec. 1975.

[40] P. J. McNulty *et al.*, “Improvements in resolution and dynamic range for FGMOS dosimetry,” *IEEE Trans. Nucl. Sci.*, vol. 52, no. 6, pp. 2597–2601, Dec. 2005.

[41] L. Z. Scheick, P. J. McNulty, and D. R. Roth, “Dosimetry based on the erasure of floating gates in the natural radiation environments in space,” *IEEE Trans. Nucl. Sci.*, vol. 45, no. 6, pp. 2681–2688, Dec. 1998.

[42] P. J. McNulty *et al.*, “Effects of previous ionizing radiation exposure on programming EPROMS,” 2002, pp. 332–337.

[43] P. J. McNulty and K. F. Poole, “Increasing the Sensitivity of FGMOS Dosimeters by Reading at Higher Temperature,” p. 5.

[44] S. Gerardin *et al.*, "Radiation Effects in Flash Memories," *IEEE Trans. Nucl. Sci.*, vol. 60, no. 3, pp. 1953–1969, Jun. 2013.

[45] N. G. Tarr, G. F. Mackay, K. Shortt, and I. Thomson, "A floating gate MOSFET dosimeter requiring no external bias supply," *IEEE Trans. Nucl. Sci.*, vol. 45, no. 3, pp. 1470–1474, Jun. 1998.

[46] N. G. Tarr, K. Shortt, Y. Wang, and I. Thomson, "A sensitive, temperature-compensated, zero-bias floating gate MOSFET dosimeter," *IEEE Trans. Nucl. Sci.*, vol. 51, no. 3, pp. 1277–1282, Jun. 2004.

[47] M. N. Martin, D. R. Roth, A. Garrison-Darrin, P. J. McNulty, and A. G. Andreou, "FGMOS dosimetry: design and implementation," *IEEE Trans. Nucl. Sci.*, vol. 48, no. 6, pp. 2050–2055, Dec. 2001.

[48] M. Alvarez, C. Hernando, J. Cesari, A. Pineda, and E. Garcia-Moreno, "Total Ionizing Dose Characterization of a Prototype Floating Gate MOSFET Dosimeter for Space Applications," *IEEE Trans. Nucl. Sci.*, vol. 60, no. 6, pp. 4281–4288, Dec. 2013.

[49] S. Danzeca *et al.*, "Characterization and Modeling of a Floating Gate Dosimeter with Gamma and Protons at Various Energies," *IEEE Trans. Nucl. Sci.*, vol. 61, no. 6, pp. 3451–3457, Dec. 2014.

[50] M. Brucoli *et al.*, "A complete qualification of floating gate dosimeter for CERN applications," in *2016 16th European Conference on Radiation and Its Effects on Components and Systems (RADECS)*, 2016, pp. 1–4.

[51] E. Pikhay, Y. Roizin, and Y. Nemirovsky, "Ultra-Low Power Consuming Direct Radiation Sensors Based on Floating Gate Structures," *J. Low Power Electron. Appl.*, vol. 7, no. 3, p. 20, Jul. 2017.

[52] J. Mekki, M. Brugger, R. G. Alia, A. Thornton, N. C. D. S. Mota, and S. Danzeca, "CHARM: A Mixed Field Facility at CERN for Radiation Tests in Ground, Atmospheric, Space and Accelerator Representative Environments," *IEEE Trans. Nucl. Sci.*, vol. 63, no. 4, pp. 2106–2114, Aug. 2016.

[53] J. R. Schwank *et al.*, "Radiation Effects in MOS Oxides," *IEEE Trans. Nucl. Sci.*, vol. 55, no. 4, pp. 1833–1853, Aug. 2008.

[54] R. J. Krantz, L. W. Aukerman, and T. C. Zietlow, "Applied Field and Total Dose Dependence of Trapped Charge Buildup in MOS Devices," *IEEE Trans. Nucl. Sci.*, vol. 34, no. 6, pp. 1196–1201, Dec. 1987.

[55] M. R. Shaneyfelt, D. M. Fleetwood, J. R. Schwank, and K. L. Hughes, "Charge yield for cobalt-60 and 10-keV X-ray irradiations of MOS devices," *IEEE Trans. Nucl. Sci.*, vol. 38, no. 6, pp. 1187–1194, Dec. 1991.

[56] T. R. Oldham and F. B. McLean, "Total ionizing dose effects in MOS oxides and devices," *IEEE Trans. Nucl. Sci.*, vol. 50, no. 3, pp. 483–499, Jun. 2003.

[57] A. Haran, M. Murat, and J. Barak, "Charge Yield and Track Structure Effects on Total Ionizing Dose Measurements," *IEEE Trans. Nucl. Sci.*, vol. 55, no. 4, pp. 2098–2105, Aug. 2008.

[58] T. R. Oldham and J. M. McGarrity, "Comparison of 60Co Response and 10 KeV X-Ray Response in MOS Capacitors," *IEEE Trans. Nucl. Sci.*, vol. 30, no. 6, pp. 4377–4381, Dec. 1983.

[59] M. Lenzlinger and E. H. Snow, "Fowler-Nordheim Tunneling into Thermally Grown SiO2," *J. Appl. Phys.*, vol. 40, no. 1, pp. 278–283, Jan. 1969.

[60] J. Madrenas, A. Ivorra, E. Alarcon, and J. M. Moteno, "Injector design for optimized tunneling in standard CMOS floating-gate analog memories," in *1998 Midwest Symposium on Circuits and Systems (Cat. No. 98CB36268)*, 1998, pp. 426–429.

[61] R. Ferraro, S. Danzeca, M. Brucoli, A. Masi, M. Brugger, and L. Dilillo, "Design of a radiation tolerant system for total ionizing dose monitoring using floating gate and RadFET dosimeters," *J. Instrum.*, vol. 12, no. 04, p. C04007, 2017.

[62] E. Garcia-Moreno *et al.*, "Floating Gate CMOS Dosimeter With Frequency Output," *IEEE Trans. Nucl. Sci.*, vol. 59, no. 2, pp. 373–378, Apr. 2012.

[63] F. P. Heiman and H. S. Miiller, “Temperature dependence of n-type MOS transistors,” *IEEE Trans. Electron Devices*, vol. 12, no. 3, pp. 142–148, Mar. 1965.

[64] E. Garcia-Moreno *et al.*, “Temperature Compensated Floating Gate MOS Radiation Sensor With Current Output,” *IEEE Trans. Nucl. Sci.*, vol. 60, no. 5, pp. 4026–4030, Oct. 2013.

[65] M. Brugger, “Radiation Effects, Calculation Methods and Radiation Test Challenges in Accelerator Mixed Beam Environments,” presented at the NSREC, Paris, 2014, p. 381.

[66] M. Brucoli *et al.*, “Floating Gate Dosimeter Suitability for Accelerator-Like Environments,” *IEEE Trans. Nucl. Sci.*, vol. 64, no. 8, pp. 2054–2060, Aug. 2017.

[67] P. Jarron *et al.*, “Deep submicron CMOS technologies for the LHC experiments,” *Nucl. Phys. B - Proc. Suppl.*, vol. 78, no. 1, pp. 625–634, Aug. 1999.

[68] A. Giraldo, A. Paccagnella, and A. Minzoni, “Aspect ratio calculation in n-channel MOSFETs with a gate-enclosed layout,” *Solid-State Electron.*, vol. 44, no. 6, pp. 981–989, Jun. 2000.

[69] F. Faccio and G. Cervelli, “Radiation-induced edge effects in deep submicron CMOS transistors,” *IEEE Trans. Nucl. Sci.*, vol. 52, no. 6, pp. 2413–2420, Dec. 2005.

[70] J. Boch, F. Saigne, L. Dusseau, and R. D. Schrimpf, “Temperature effect on geminate recombination,” *Appl. Phys. Lett.*, vol. 89, no. 4, p. 042108, Jul. 2006.

[71] S. M. Sze and M. K. Lee, *Semiconductor devices : physics and technology*, 3rd ed. New York, NY : Wiley, 2012.

[72] K. Roeed, M. Brugger, and G. Spiezia, “An overview of the radiation environment at the LHC in light of R2E irradiation test activities,” Sep. 2011.

[73] D. Kramer *et al.*, “LHC RadMon SRAM Detectors Used at Different Voltages to Determine the Thermal Neutron to High Energy Hadron Fluence Ratio,” *IEEE Trans. Nucl. Sci.*, vol. 58, no. 3, pp. 1117–1122, Jun. 2011.

[74] A. Thornton, “CHARM Facility Test Area Radiation Field Description,” CERN, CERN-ACC-NOTE-2016-0041.

[75] B. Schmidt, “The High-Luminosity upgrade of the LHC: Physics and Technology Challenges for the Accelerator and the Experiments,” *J. Phys. Conf. Ser.*, vol. 706, no. 2, p. 022002, 2016.

[76] R. G. Alía *et al.*, “LHC and HL-LHC: Present and Future Radiation Environment in the High-Luminosity Collision Points and RHA Implications,” *IEEE Trans. Nucl. Sci.*, vol. 65, no. 1, pp. 448–456, Jan. 2018.

[77] J. Mekki, M. Brugger, S. Danzeca, L. Dusseau, K. Røed, and G. Spiezia, “Mixed Particle Field Influence on RadFET Responses Using Co-60 Calibration,” *IEEE Trans. Nucl. Sci.*, vol. 60, no. 4, pp. 2435–2443, Aug. 2013.